Imaging Lipid Phase Separation in Droplet Interface Bilayers

A dissertation

by

JOHN SHOKRI HANNA DANIAL

submitted in partial satisfaction
of the requirements for the degree

of

Doctor of Philosophy

in

Physical and Theoretical Chemistry

in the

Mathematics, Physical and Life Sciences Division

of the

University of Oxford

St. Anne's College
Trinity 2015

Imaging Lipid Phase Separation in Droplet Interface Bilayers
JOHN SHKORI HANNA DANIAL
University of Oxford
Trinity 2015

Abstract

The spatiotemporal organization of membrane proteins is implicated in cellular trafficking, signalling and reception. It was proposed that biological membranes partition into lipid rafts that can promote and control the organization of membrane proteins to localize the mentioned processes. Lipid rafts are thought to be transient (microseconds) and small (nanometers), rendering their detection a challenging task. To circumvent this problem, multi-component artificial membrane systems are deployed to study the segregation of lipids at longer time and length scales. In this thesis, multi-component Droplet Interface Bilayers (DIBs) were imaged using fluorescence and interferometric scattering microscopy. DIBs were used to examine and manipulate microscopic lipid domains and to observe, for the first time, transient nanoscopic lipid domains. The techniques and results described here will have important implications on future research in this field.

Statement of Originality

The work described in this thesis was carried out between October 2012 and August 2015, in the laboratory of Dr. Mark I Wallace at the Chemistry Research Laboratory of the University of Oxford. All the work described within this thesis is my own. Experimental work was done in collaboration with G. de Wit, J. Rojko and J. Sengel. This work has not been submitted previously for any other degree at the University of Oxford or any other university. Manuscripts prepared from this work are detailed in Appendix A.

John S. H. Danial
Oxford, 12 August 2015

Acknowledgements

The work between your hands, dear reader, is an accumulation of the efforts of numerous people. It is unfair that my name appears on the front cover of this dissertation and I would, therefore, like to take this opportunity to thank those who have shared in shaping this dissertation and most importantly, my persona, over the course of the past three years.

It has been a source of genuine joy to work under the supervision of Dr. Mark I. Wallace. Those three years, beyond this written dissertation, were very enlightening thanks to his critical supervision.

I Would like to thank my funding body, the Louis Dreyfus-Weidenfeld Scholarships and Leadership Programme, for the generous financial support throughout the past 3 years. Dame Elizabeth Roberts and Dr. John Adamson, from the Weidenfeld-Hoffmann trust have been extremely helpful throughout and I would like to extend specials thanks to them.

I would also like to thank all the current and former members of the Wallace group: Dr. Matthew Cheetham, Dr. Daniel Kattnig, Dr. Carina Monico, Dr. Hajra Basit, Dr. Ravinash Kumar, Dr. Matthew Baker, Dr. Oliver Castell, Michael Senior, Marc Szabo, Jason Sengel, Eve Weatherill, Helena Coker and Vivek Ramakrishna. Those 3 years have been extremely joyful because of your presence. I hope that each one of you will remember me.

I would like to thank Dr. Philipp Kukura and Gabrielle de Wit for the very fruitful, engaging and highly intellectual collaboration.

I would like to thank my friends outside academia: Dr. Antony Aziz, Dr. George Kamel, Fr. Morkos Fakhry, Girgis Youssef, Harvey Nagy and Youhanna Youssef for their companionship, love, care and, most importantly, prayers. I will never forget you.

I would like to thank the one who shared the pains and joys of those three years with humbleness: Christine Hanna. I look forward to our wedding and sharing our joys and tragedies thereafter.

I would like to thank my sister Gena Danial. I will never forget the beautiful days we have spent, and will spend, together.

I would like to thank Nihad Nadam for generously providing me with the arabic calligraphy artwork on the next page that translates to: “to mum and dad”.

Having said so, an artwork alone shall never repay my mum and dad the 26 years they have spent caring for me. I am eternally grateful to God for providing me with such indescribably beautiful parents. I can do nothing to repay their love except to offer this dissertation as a humble gift to them.

Beyond, and above, all, is my heavenly father to whom no words or sacrifice can express my gratitude for his support, for his love, for his care and for his beauty. The beauty of his creation is a projection of his beauty. I will remain grateful to him for giving me the opportunity to see him in living matter.

إِلى أَبي وَأُمّيْ

Contents

List of Figures

Acronyms

AFM	Atomic Force Microscopy
AOD	Acousto-Optic Deflector
BLM	Black Lipid Membrane
bSM	brain Sphingomyelin
CAD	Computer Aided Design
Chol	Cholesterol
CMOS	Complementary Metal-Oxide Semiconductor
CNC	Computer Numerical Control
DIB	Droplet Interface Bilayer
DiI	1,1-dioctadecyl-3,3,3,3-tetramethylindocarbocyanine
DLPC	1,2-dilauroyl-sn-glycero-3-phosphocholine
DMPE	1,2-Dimyristoyl-sn-glycero-3-phosphoethanolamine
DOPC	1,2-Dioleoyl-sn-glycero-3-phosphocholine
DPhPC	1,2-diphytanoyl-sn-glycero-3-phosphocholine
DPPC	1,2-dihexadecanoyl-sn-glycero-3-phosphocholine
DPPE	1,2-dihexadecanoyl-sn-glycero-3-phosphoethanolamine
DSPC	1,2-Distearoyl-sn-glycero-3-phosphocholine
EM-CCD	Electron Multiplying Charge Coupled Detector
EqII	Equinatoxin II
eSM	egg Sphingomyelin
FCS	Fluorescence Correlation Spectroscopy
FRAP	Fluorescence Recovery After Photobleaching
FRET	Forster Resonance Energy Transfer
FWHM	Full Width at Half Maximum
GPI	Glycophosphatidylinositol
GPMV	Giant Plasma Membrane Vesicle
GUV	Giant Unilamellar Vesicle
HeLA	HEnrietta LAcks
HEPES	4-(2-hydroxyethyl)-1-piperazineethanesulfonic acid
HWHM	Half Width at Half Maximum
iSCAT	Interferometric Scattering
LoG	Laplacian of Gaussian
MSD	Mean Squared Displacement
NMR	Nuclear Magnetic Resonance

PBS	Polarizing Beam Splitter
PID	Proportional-Integral-Derivative
PMMA	poly-methyl methacrylate
POPC	1-palmitoyl-2-oleoyl-sn-glycero-3-phosphocholine
PSF	Point Spread Function
Ptk	Potorous tridactylus kidney
QD	Quantum Dot
RICM	Reflection Interference Contrast Microscopy
SANS	Small Angle Neutron Scattering
SLB	Supported Lipid Bilayer
STED	Stimulated Emission by Depletion
SUV	Small Unilamellar Vesicle
TIRF	Total Internal Reflection Fluorescence
TRITC-DHPE	N-Tetramethylrhodamine-6-thiocarbamoyl-1,2-dihexadecanoyl-sn-glycero-3-phosphoethanolamine, triethylammonium salt
VLP	Virus Like Particle

1

Lipid membranes

The complex organization of the cell membrane, arising from its heterogeneous population of lipids and proteins, plays an important role in facilitating many biological processes, including: signalling, trafficking, recognition and adhesion [159, 60, 189, 126, 4]. This chapter summarizes the role of lipids in controlling membrane organization.

1.1 Lipids

Lipids are biological amphiphiles that form a variety of structures, including: micelles, liposomes and bilayer sheets (figure 1.1). More than 100 different lipid types are present in biological membranes [27, 71, 15], however, only a few are present in abundance, and which contribute to its gross organization.

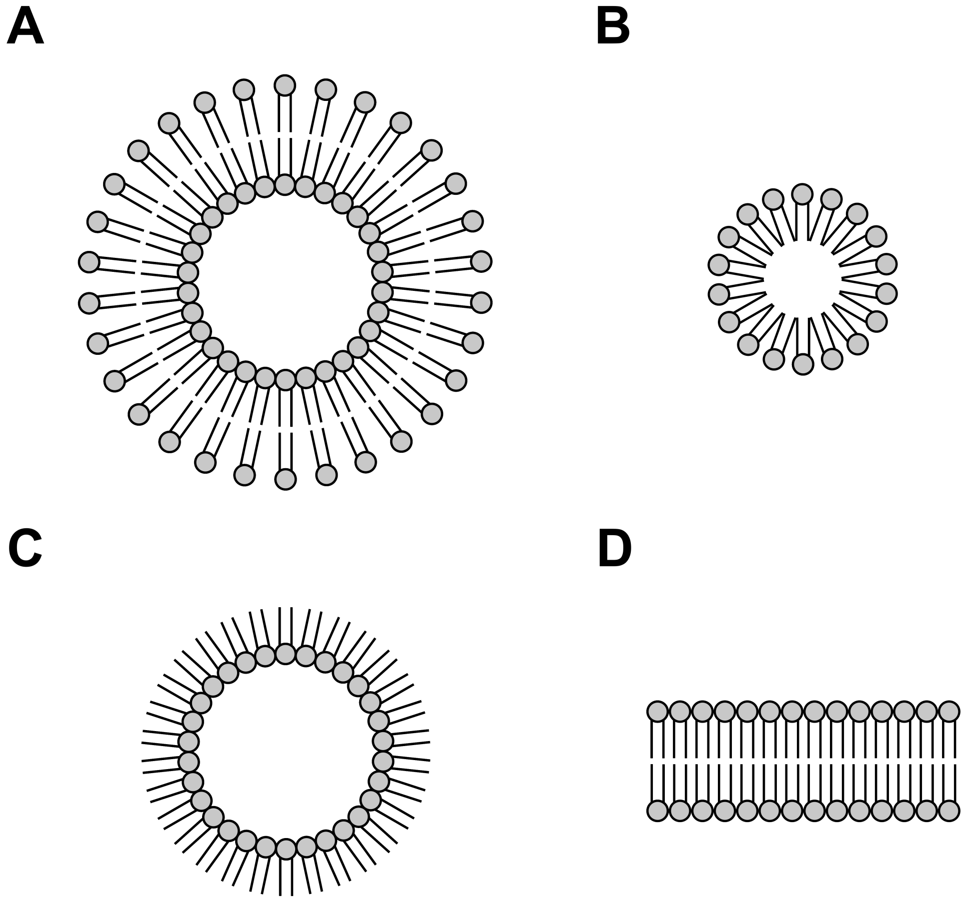

Figure 1.1: Lipids can form a variety of structures including (A) Liposomes, (B) Micelles, (C) Inverse micelles and (D) Two-dimensional lipid bilayers.

A. **Phospholipids** are the major component of biological membranes [192]. They posses a hydrophilic negatively-charged phosphate group (head) and a hydrophobic hydrocarbon tail. Phosphatidylcholine (PC) is a major sub-component of phospholipids found in abundance in cellular membranes. In eukaryotes, as well as prokaryotes, PC is found mainly on the outer leaflet of the cell membrane [129]. Phosphatidylethanolamine (PE) is the second most abundant lipid found in cellular membranes [190].

B. **Sphingolipids** account for 15 - 40% of the total molar lipid composition of the plasma membrane [191]. The saturated carbon tail of sphingolipids promotes the formation of ordered phases in multi-component bilayers.

Sphingolipids are composed of a sphingosine base linked via an ester linkage to a charged head group (figure 1.2). Similar to phospholipids, the head group in sphingolipids can be an ethanolamine, a serine, or a choline group. Sphingolipids have a prominent role in signal transduction [44, 98, 119].

C. **Glycolipids** are implicated in cellular recognition. Glycolipids are mainly found in the outer layer of cellular membranes [200].

D. **Sterols** are amphipathic molecules thought to affect the organization of biological membranes [163, 166, 113, 164]. Sterols are composed of multiple hydrocarbon rings that form a flat face serving to order the tails of unsaturated lipids upon interaction [86, 191, 117].

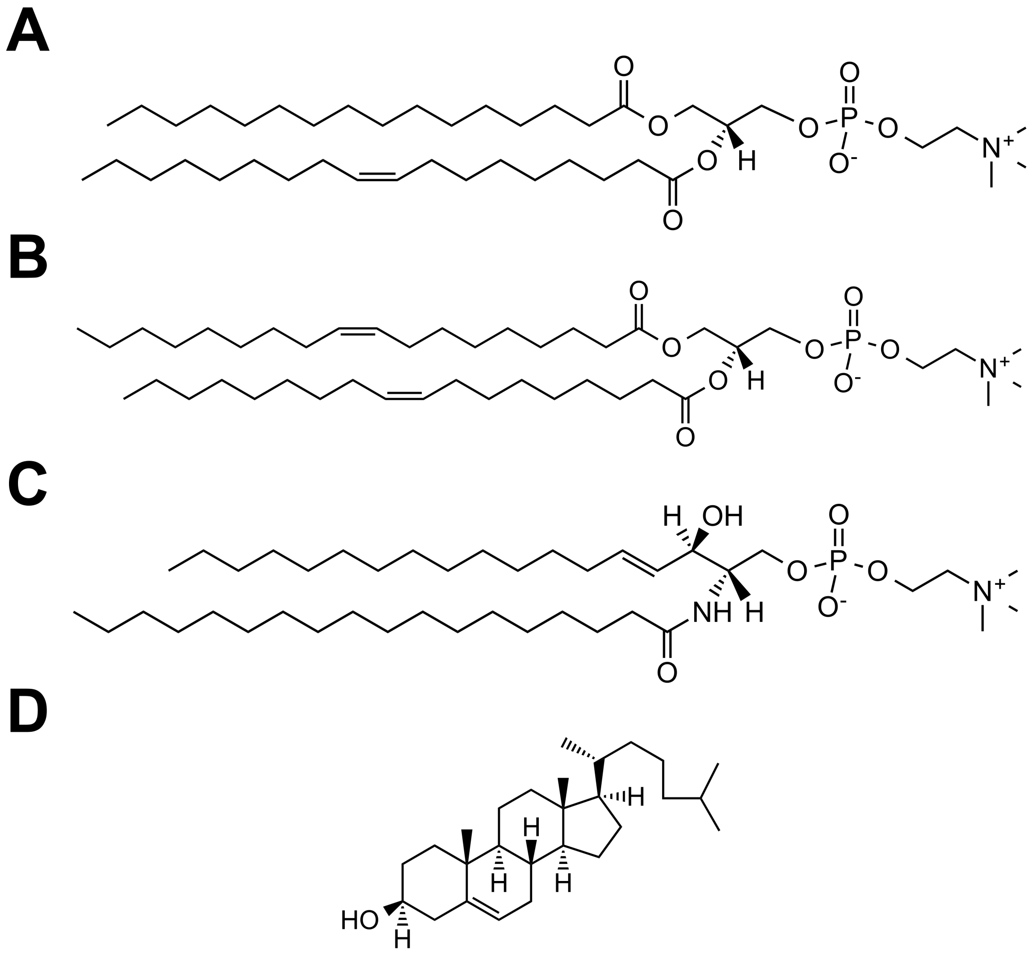

Figure 1.2: Chemical structure of lipids and cholesterol used in this thesis. (A) DOPC, (B) POPC, (C) egg Sphingomyelin and (D) Cholesterol.

Nuclear Magnetic Resonance (NMR) measurements, along with fluorescence microscopy observations, established the presence of three major phases in multi-component lipid bilayers [196, 195]:

A. a liquid disordered (L_d) phase enriched in phospholipids and characterized by lack of conformational and translational order across the lipid chains,

B. a liquid ordered (L_o) phase enriched in cholesterol which imposes a long range organizational pattern by ordering phospholipids' chains, and,

C. a solid ordered (S_o) phase enriched in saturated lipids which cooperatively exist in a packed structure to induce long-range translational and conformational order across the bilayer.

The three phases can individually exist, or mutually coexist, in multi-component bilayers depending on their composition (section 1.5).

The presence of cholesterol at relatively high molar quantities in the membrane of living cells, and its profound role in inducing translational and conformational order in otherwise disordered multi-component lipid membranes, has led to the examination of its interaction with phospholipids at a molecular level. In 1999, Huang and Feigenson proposed the first model for the interaction of cholesterol with phospholipids [86]. Their model proposed an ”umbrella”-like interaction whereby the polar head groups of lipids shield the non-polar cholesterol to thus prevent its energetically unfavourable exposure to water. Increasing cholesterol concentration lead to the close packing of both lipid chains and cholesterol molecules. The flat ring-like structure of sterols in general, and cholesterol more specifically, allows the ordering of the lipid's chains whilst retaining translational freedom across the lipid head groups. In 2003, McConnell and coworkers published a series of studies suggesting that cholesterol can form distinct complexes with phospholipids [117]. The proposed complexes, which could vary in size between 12 and 60 molecules, were claimed to lead to the ”condensation effect” whereby the area occupied by a phospholipid is decreased upon interaction with cholesterol. It was further suggested that the condensed complex would be stable below a certain transition temperature and would dissociate at higher temperatures. These conclusions were derived from experiments performed on lipid monolayers with the assumption that the findings could be extrapolated to lipid bilayers.

In an attempt to describe the mentioned differences, Almeida published a theoretical framework explaining lipid interactions from a thermodynamic perspective and their role in the formation co-existing phases [3]. Although all these models do not provide useful insights on the structural role of cholesterol in facilitating conformational order across different lipid genres, the dynamic aspects of domain formation, registration and coalescence have been studied in different groups and are detailed below.

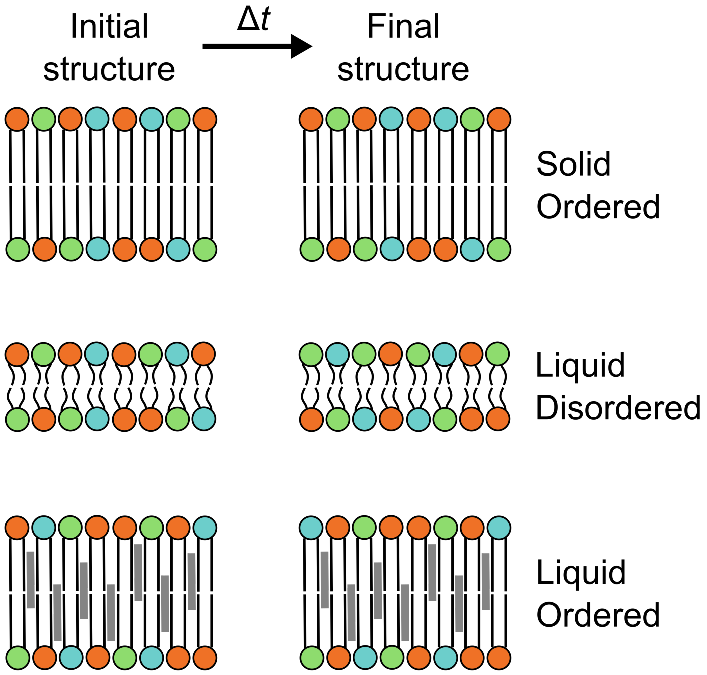

Figure 1.3: Three distinct lipid phases exist in multi-components lipid membranes: solid ordered (S_o), liquid ordered (L_o) and liquid disordered (L_d); each describing the state of lipids in a bilayer. In the S_o phase, high transition temperature (T_m) phospholipids show conformational and translational order across the chains. In the L_o phase, low T_m phospholipids are free to translate across the bilayer but their chains are ordered due to interactions with the cholesterol. In the L_d phase, low T_m phospholipids show conformational and translational disorder across the chains.

1.2 Organization of the cell membrane

This section discusses three non-exclusive models for the organization of the cell membrane: the fluid-mosaic, lipid rafts and picket-fences.

1.2.1 Fluid mosaic

In 1972, Singer and Nicholson proposed a model for the structural organization of the cell membrane [167]. Previously, the cell membrane was thought to be arranged in alternating layers of proteins and lipids [40]. In their model, Singer and Nicholson described the cell membrane as a two dimensional fluid lipid bilayer in which peripheral and integral proteins are randomly dispersed and freely diffuse to form a “fluid mosaic”. Previous experiments by Frye and Edidin had uncovered the dependence of membrane proteins’ diffusion on temperature [57]. It was also already established that phospholipids undergo reorganization, from gel-like to liquid-like phases, when subjected to changes in temperature [172, 118, 50, 186]. This allowed Singer and Nicholson to suggest that membrane proteins are embedded in a lipid bilayer and that, furthermore, the lipid bilayer is fluid [167]. In 1975, Saffmann and Delbruck developed a theoretical model describing the unrestricted lateral diffusion of solid inclusions a two-dimensional membranes [150]. The details of this model are given in section 1.4.

1.2.2 Lipid rafts

Experiments carried out between 1974 and 1982 pointing towards the partitioning of cellular membranes into specialized domains went beyond the simple model envisaged by Singer and Nicholson. The physical properties and biological role of these domains remain a subject of intense debate. In the 1970s, a number of scientists postulated the ordering of cellular membranes into crystalline micro-sized domains [172, 186, 173, 51]. Further biophysical investigations during during 1970s and 1980s served to refine the structural description of domains from crystalline to quasi-crystalline [201, 184, 38, 26]. In 1982, Karnovsky and coworkers published a first review presenting the structural and biological evidence supporting the organization of cellular membranes into lipid domains [96]. Although the size and constituents of the proposed lipid domains was not known, their results allowed them to infer that compositional heterogeneity in biological membranes could be a driving force behind the formation of membrane domains. During the 1990s, detergent insoluble lipid extracts were extensively reported [56, 41, 156, 168, 32, 72]. The insoluble extracts were reported to be rich in sphingolipids, glycolipids and cholesterol. Simons and Ikonen interpreted these results in favour of the presence of domains in cellular membranes and, in 1997, proposed the concept of lipid rafts as a membrane organizing principle [163]. Between 1997 and 2007, macroscopic lipid domains were visualized and characterized in model membranes formed of a reduced number of components [100, 155, 42, 17, 197, 196, 34] and in biological membranes under non-physiological conditions [110, 16, 70, 112, 194]. Stable proteolipid rafts were not observed in cellular membranes as it would be expected from detergent extraction experiments. Later, Heerklotz showed evidence that previously used detergents promoted domain formation in lipid raft mixtures [77]. These conflicting results led to lipid rafts being redefined during a 2006 keystone symposium as: “small (10 - 200 nm), heterogeneous, highly dynamic, sterol and sphingolipid enriched domains that compartmentalize cellular processes” [135]. This definition placed the time and lengths scales of lipid rafts far beyond the realm of non-invasive microscopy techniques. In 2009, Eggeling and coworkers reported their use of Stimulated Emission by Depletion (STED) microscopy and fluorescence correlation spectroscopy (FCS) to reveal the transient and dynamic confinement (10 - 20 ms) of a lipid probe in cholesterol-mediated 20 nm complexes [48]. Although the probe confinement was shown to correlate with the presence of sphingomyelin and cholesterol, it remains unclear if the confinement was a result of the presence of transient nanoscopic lipid domains or the transient binding of the probe to other supra-molecular structure. Although long-lived protein nanoclusters have been observed in biological membranes [60, 90, 66, 142], the existence of transient lipid rafts remains a contentious topic [127, 105, 136, 89].

1.2.3 Picket fences

The compositional richness of biological membranes and the lack of evidence for the existence of observable lipid domains has inspired the proposition that membrane organization is governed by supra molecular structures. In 1996, Kusumi and Sako proposed a third model for the organization of the cell membrane; the membrane-cytoskeleton model [152, 153, 104]. Kusumi pioneered the argument that the anomalous (non-directed) diffusion in cellular membranes is induced by the interaction of the cytoskeleton with the lipid bilayer. Single particle tracking showed hop-diffusion of a number of receptors on the surface of cellular membranes [58]. Schmidt, Kucik, Edidin and coworkers also optically-trapped receptor-gold nanoparticle complexes and their trajectories corresponded to transient confinement of membrane proteins in, possibly, cytoskeleton-confined domains [159, 101, 47]. In 2005, it was reported that phospholipids undergo anomalous diffusion in the outer leaflet of cellular membranes. These reports were surprising as it was expected that the diffusion of phospholipids in the outer leaflet would not be affected by the cytoskeleton, which resides on the cytoplasmic region of the cell membrane. In the same year, Kusumi and coworkers refined their membrane-cytoskeleton model to take into account the effect of cytoskeleton membrane-anchored proteins [103] on the diffusion of lipids. In their model, they proposed a “picket-fence” structure whereby the local viscosity induced by cytoskeleton (fence) - bound proteins (pickets) can effectively act against the free diffusion of lipids in both the outer and inner leaflets of the cell membrane.

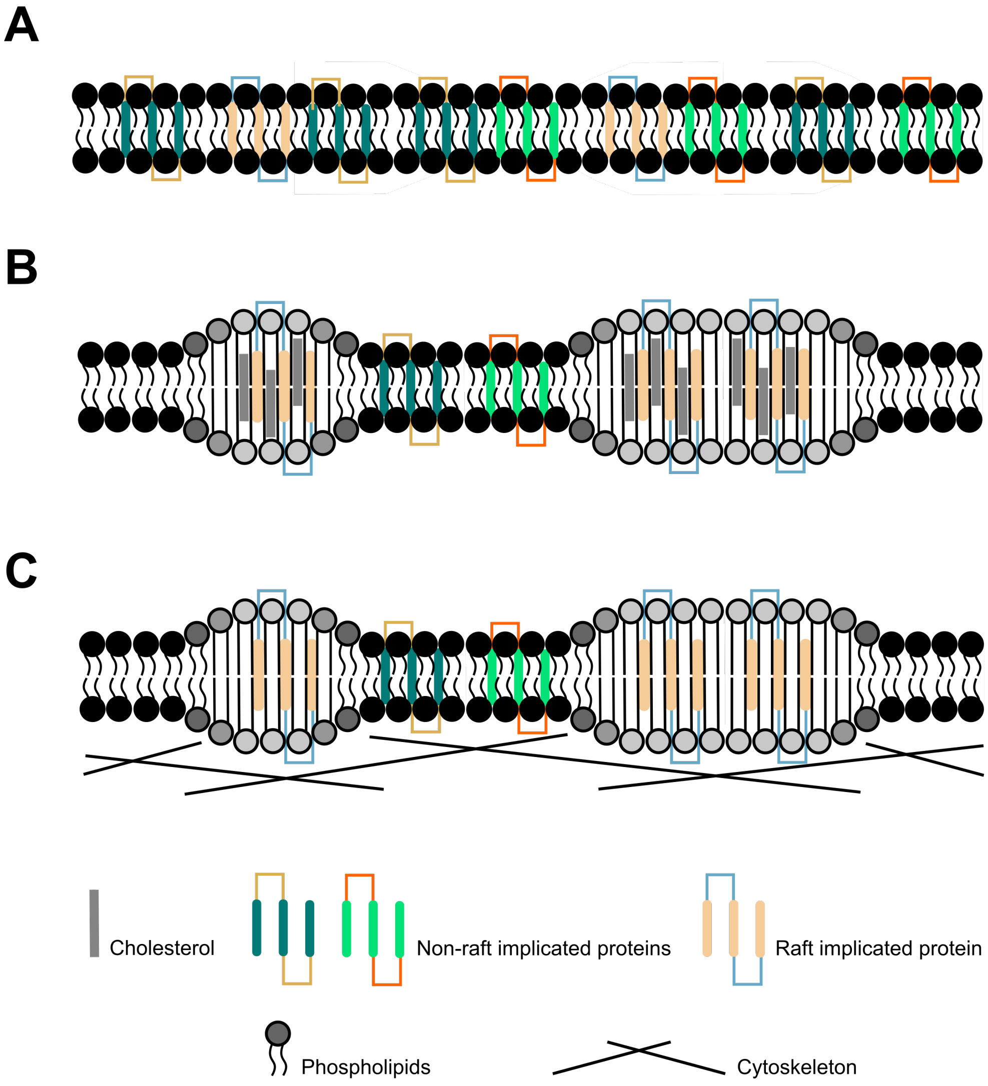

Figure 1.4: Different models proposed for the organization of proteins and lipids in biological membranes. (A) Fluid mosaic model: describes the random dispersion of proteins in a fluid membrane. (B) Lipid rafts model: describes the ordering of lipid chains by cholesterol to form specialized lipid “rafts” which are nanoscopic and transient in nature, and capable of modulating protein function. (C) Picket fence model: describes the segregation of biological membranes into compartments through the binding of the cytoskeleton to transmembrane proteins.

1.3 *In vitro* mimics of the cell membrane

The previous section highlighted the putative complex role imposed by lipids and proteins in organizing cellular membranes. In order to isolate the mechanism of action of lipids on the formation of rafts, lipid phase separation has been studied in lipid bilayers. The architecture, construction, shortcomings and advantages of such mimics are surveyed below.

1.3.1 Black lipid membranes

In 1964, Mueller and coworkers developed Black Lipid Membranes (BLMs), also known as planar lipid bilayers [125]. Traditionally, BLMs have been formed by immersing a Teflon annulus ($\approx$ 10 s micrometers) through an air/water interface covered in a lipid monolayer. Although readily form-able and can posses superior resistance seals (≥ 1 GΩ), BLMs are short lived. BLMs have been used for several decades for recording the electrical activity of reconstituted proteins [124] and more recently to image macroscopic lipid phase separation [162].

1.3.2 Supported lipid bilayers

Unlike BLMs, where the bilayer is surrounded with an aqueous phase, Supported Lipid Bilayers (SLBs) are formed directly on a substrate, typically glass, with, thus, the upper leaflet exposed to free solution and the other suspended above the substrate by a thin ($\approx$ 1 nm) water layer. This architecture renders SLBs accessible via a wide range of characterization tools including: Surface Plasmon Resonance [154], interferometric scattering microscopy [8] and Atomic Force Microscopy (AFM) [45, 121]. Traditionally, SLBs were formed by Langmuir-Blodgett deposition [106, 25]. Although this technique is still used to create SLBs, it requires careful control of surface pressure induced by the packing of the self-assembled lipid mono-layer at the air/water interface. More recently, the rupture of small lipid vesicles onto a substrate has been used to construct SLBs [179]. Being accessible to high resolution scanning probe techniques, SLBs has been used to observe nanoscopic lipid domains [36]. However, slow probe scanning speeds and substrate-induced hindered diffusion of lipid domains remain significant problems for these methods. Even when SLBs are supported on a polymer cushion, diffusion is several orders of magnitude slower than that reported in Giant Unilamellar Vesicles (GUVs) [64].

1.3.3 Giant unilamellar vesicles

Giant Unilamellar Vesicles (GUVs) are, by far, the most widely used artificial membrane system for studying lipid phase separation. The architecture of GUVs resembles the architecture of an empty cell; an aqueous phase surrounded by a lipid bilayer immersed into an aqueous solution. This exclusive architecture allows the study of many cellular process in an environment which spatially resembles the environment of a living cell. GUVs were first described by Reeves and Dowben in 1969 [144] and were later developed as a fluid lipid membrane system employed for different applications. The application of an electric field through a deposited lipid film (also called electroformation) has been extensively used to form GUVs [9]. Despite its popularity, this method yields GUVs of heterogeneous composition and size. A primary cause behind the observed heterogeneity is lipid mixing in the dry film state. To circumvent that problem, Baykal-Cagler and coworkers demonstrated the successful electroformation of GUVs from damp lipid films [19]. The modified protocol was proven to ameliorate this problem but at the expense of long ($\approx$ 24 hours) preparation times. Thus far, there has been no easy and efficient solution to forming GUVs of homogeneous composition and size using electroformation. Recently, microfluidic techniques were successfully employed to produce GUVs of controlled size [147, 95, 170, 116], however, the applicability of this method to study lipid phase separation has not been demonstrated. Arriaga and coworkers used water-in-oil-in-water double emulsion drops as templates for phase-separated GUVs [10]. The published protocol was tested using a ternary mixture of DOPC, DPPC, and Cholesterol. Measurement of the area fraction occupied by the L_o phase over a small number of GUVs revealed a small standard deviation ($\approx$ 0.05%). Homogeneous GUVs can be formed by the spontaneous budding of a lipid film at an agarose(or hydrogel)/buffer interface [85]. However, lack of control over the size of the formed GUVs remains a problem. Although a single method for readily creating homogeneous and equally sized GUVs does not yet exist, GUVs are routinely used as model system for visualising lipid membrane organization [199]. Multi-component GUVs have been employed for studying lipid phase separation *in vitro*; in particular, to map out phase diagrams of ternary [195, 24] and quaternary lipid mixtures [99] and investigating the dynamics of lipid domains [34] (section 1.4) .

1.3.4 Droplet interface bilayers

Since 2007, the Wallace and Bayley labs at the University of Oxford have been developing a novel model system which is fluid, substrate-supported, accessible via a wide array of characterization techniques and long-lived [21]. Since its conception, Droplet Interface Bilayers (DIBs) have been used for the detection of membrane channels [80], measuring ionic currents and fluorescence from single protein pores [79], controlling 2D membrane protein concentration [68] and imaging the assembly of multi subunit protein complexes [182]. DIBs are formed by the contact of two lipid monolayers surrounding two aqueous droplets. DIBs can also be formed between a hydrogel film and an aqueous droplet, both immersed in a lipid-in-oil solution [109]. Unlike GUVs, where changes in lipid mixing can occur as a dry lipid film rehydrates, lipids in DIBs are free to mix both before and after bilayer formation and remain in equilibrium with the lipids solubilized in the surrounding oil bath (chapter 3). The fluidity and supported architecture of DIBs renders them suitable for imaging lipid phase separation using a wide range of optical techniques.

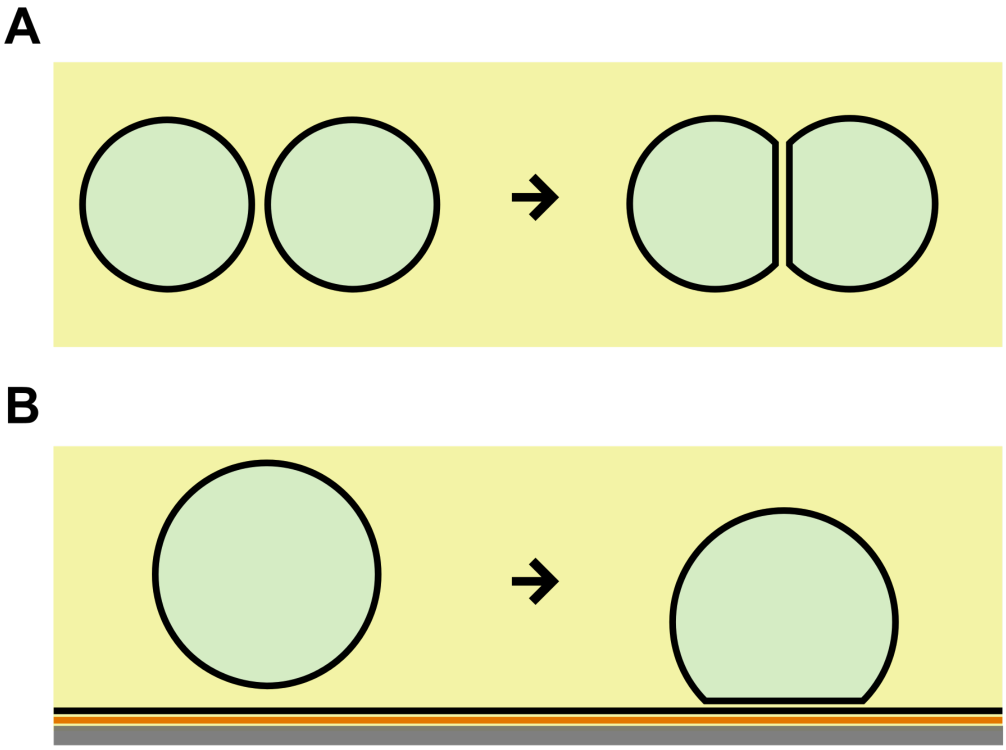

Figure 1.5: Formation of DIBs. (A) DIBs can be formed by the contact of two aqueous droplets immersed in a solution of lipids in oil, or, (B) by the contact of an aqueous droplet with a substrate supported thin hydrogel film both immersed in a solution of lipids in oil. Solid black lines represent lipid monolayers. Orange represents hydrogel.

1.4 Diffusion in lipid membranes

Diffusion in lipid membranes is crucial for understanding membrane dynamics. Models approximating diffusion in two-dimensional membranes are surveyed in this section.

1.4.1 Brownian motion

The distance x_N covered by a randomly moving particle from an origin after N steps is given by the following equation

$$\langle x_N^2 \rangle = 2Dt \tag{1.1}$$

$\langle x_N^2 \rangle$ is the Mean Squared Displacement (MSD), D is the diffusion coefficient and t is the time-lag. The constant 2 is indicative of space dimensionality. Therefore, $\langle x_N^2 \rangle = 4Dt$ in two dimensions and $\langle x_N^2 \rangle = 6Dt$ in three dimensions. The relationship between D and the temperature of the system T can be derived by considering thermal forces [12]. The translational and rotational diffusion of a particle in any medium can be written in terms of the translational and rotational mobilities,μ_T and μ_R, as follows:

$$\frac{D_T}{\mu_T} = k_B T \tag{1.2}$$

$$\frac{D_R}{\mu_R} = k_B T \tag{1.3}$$

Equations 1.2 and 1.3 are known as Einstein - Stokes relations. In 1851, Stokes derived an expression for μ_T and μ_R (the rotational mobility) which depends on the surrounding liquid's drag coefficient ξ and which in turn can be expressed in terms of the particle's radius a, and the liquid's viscosity η, through the following relationship:

$$\begin{aligned} \mu_T &= \frac{1}{\xi} = \frac{1}{6\pi\eta a} \\ \mu_R &= \frac{1}{8\pi\eta a^3} \end{aligned} \tag{1.4}$$

This set of equations are known as Stokes formulas and are only applicable to the translational and rotational diffusion of a particle in 3 dimensions.

1.4.2 Stokes paradox

The Stokes formula is suitable for studying the flow of fluids with low flow velocities, large viscosities or small flow length-scales in three dimensions. A non-trivial, steady-state solution for diffusion in two-dimensional systems does not exist (Stokes paradox) due to creeping flow. This paradox complicates the modelling of translational diffusion of cylindrical-shaped objects in two-dimensional membranes.

1.4.3 Saffman and Delbrück model

In 1975, Saffman and Delbrück published a hydrodynamic model approximating the diffusion of a cylindrical inclusion in a continuous, infinite, viscous membrane separating a less viscous liquid. Although lipid phase separation was not observed at that time, the model was presented to describe the, experimentally observed, diffusion of membrane proteins [150].

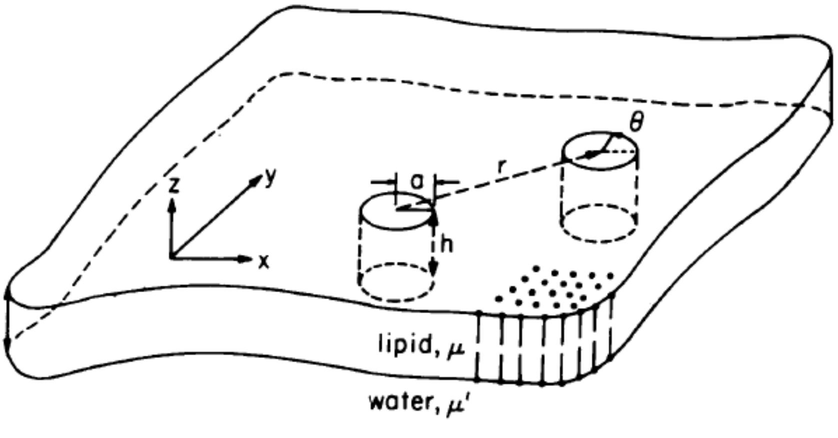

Figure 1.6: Diagram depicting the translational and rotational diffusion of a solid cylindrical inclusion of a two-dimensional lipid bilayer of viscosity separating a less viscous water phase. Reproduced from [150].

Referring back to equations 1.4, it can be noted that the ratio of μ_T to μ_R is independent of the surrounding viscosity η

$$\mu_T/\mu_R = \frac{4}{3}a^2 \tag{1.5}$$

In 2 dimensions, the rotational diffusion is indifferent to the architecture of the surrounding and therefore is represented as:

$$\mu_R = \frac{1}{4\pi\mu a^2 h} \tag{1.6}$$

Saffman and Delbrück considered the translation of an infinite cylinder of radius a in a continuous membrane of height h and viscosity η_m, surrounded by a less viscous liquid of viscosity η_w of finite depth H. Assuming that the depth of the surrounding liquid phase is much larger than the radius of the cylinder

$(H/a \rightarrow \infty)$ and that $\eta a/\eta_m h << 1$, the translational mobility μ_T of the cylinder can be deduced

$$\mu_T = \frac{1}{4\pi\eta_m h}\left(\ln\frac{2\eta_m h}{\eta a} - \gamma\right) \tag{1.7}$$

where $\gamma \approx 0.577$ is the Euler —Mascheroni constant. Equation 1.7 describes the motion of a cylinder in an infinite membrane bounded by a liquid phase of finite viscosity. Saffman and Delbrück expanded this approximation for diffusion in a circular sheet of radius R. The translational mobility in that case is given by:

$$\mu_T = \frac{1}{4\pi\eta h}\left(\ln\frac{R}{a} - \frac{1}{2}\right) \tag{1.8}$$

μ_R is inversely proportional to a^2 while μ_T is inversely proportional to a. These results indicate low energy dissipation in the bounding phase resulting in an increase of the translational mobility, while the rotational mobility is entirely dependant on the viscosity of the membrane and it, therefore, scales according to the space dimensions. Saffmann and Delbrück justified their assumptions by calculating the translational diffusion coefficient for Rhodopsin which matched experimentally reported values [150].

1.4.4 Hughes, Pailthorpe and White model

Discrepancy between membrane viscosity values obtained from fitting the Saffmann Delbrück model to diffusion data and values obtained by other means has caused considerable confusion. In 1981, Hughes, Pailthorpe and White proposed a more accurate numerical solution [87]. In their report, the translational and rotational mobilities, μ_T and μ_R, respectively, were calculated and represented in terms of matrices of bessel functions dependent on the reduced inclusion size ϵ and the membrane's and surrounding viscosities. The equations derived by Hughes, Philthorpe and White represents an infinite set of equations which cannot be analytically solved.

In 2008, Petrov and Schwille developed a simple and accurate numerical approximation of the Hughes, Philthorpe and White model[134]. In their report, equation **??** was numerically evaluated and truncated to 30 equations. The resulting reduced mobility factor $\Delta(\epsilon)$ was expressed as follows:

$$\Delta_T(\epsilon) = \frac{\ln(2/\epsilon) - \gamma + 4\epsilon/\pi - (\epsilon^2/2)\ln(2/\epsilon)}{1 - (\epsilon^3/\pi)\ln(2/\epsilon) + c_{T1}\epsilon^{b_{T1}}/(1 + c_{T2}\epsilon^{b_{T2}})} \tag{1.9}$$

where $b_{T1} = 2.74819$, $b_{T2} = 0.61465$, $c_{T1} = 0.73761$ and $c_{T2} = 0.52119$. The coefficient of translational diffusion can be expressed in terms of the reduced mobility factor as follow:

$$D_T(\epsilon) = D_0\Delta_T(\epsilon) \tag{1.10}$$

where $D_0 = k_BT/4\pi\eta_m$. The resulting numerical approximation was tested on data by Cicuta and coworkers [34] and were found to conform. As a consequence of the lack of data on the rotational diffusion of micron-sized domains, the applicability of the numerical approximation in describing the rotational diffusion of bilayer embedded inclusions was not elucidated in their report. However, later, in 2012, an approximation for the rotational diffusion was derived and validated on freely diffusing diamond-shaped micron-sized domains in multi-component phase separated GUVs (see 1.5.3) [133]. For rotational diffusion, the base term $D_0 = k_BT(\eta)^2/(\pi\eta_m^3)$ and $\Delta(\epsilon)$ is expressed as:

$$\Delta_R(\epsilon) = \frac{1}{\epsilon^2 + 4\epsilon^3/(3\pi) + c_{R1}\epsilon^{b_{R1}}/(1 + c_{R2}\epsilon^{b_{R2}})} \tag{1.11}$$

where $b_{R1} = 2.91587$, $b_{R2} = 0.68319$, $c_{R1} = 0.31943$ and $c_{R2} = 0.60737$. Viscosity values extracted by fitting the rotational and translational diffusion coefficients were found to agree with previously reported values, thus suggesting the applicability of the approximation.

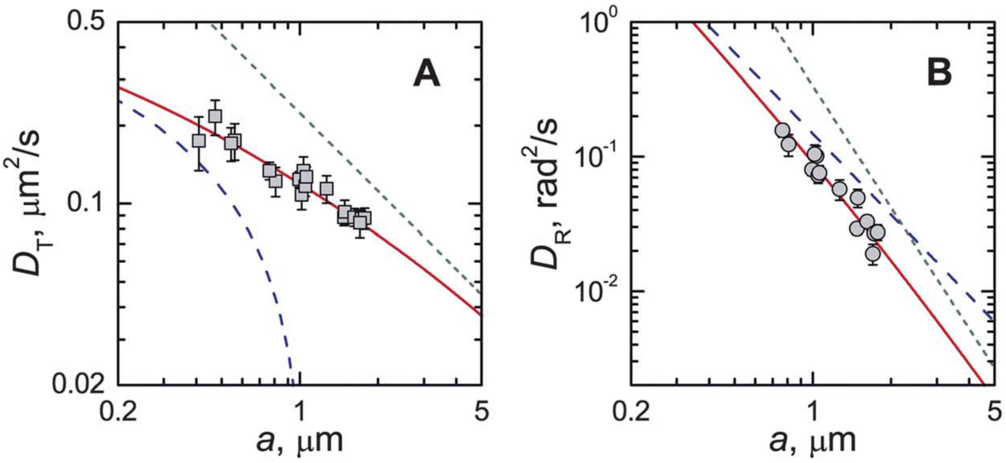

Figure 1.7: Translational (A) and rotational (B) diffusion of diamond-shaped S_o domains in osmotically-tensed GUVs. Data is well-described by the Petrov et al. approximation of the Hughes, Philtorpe and White model (red solid line) for the diffusion of cylindrical inclusions in two-dimensional membranes. Simultaneous curve fitting to the translational and rotational diffusion data resulted in an average membrane viscosity value of 2.2×10^{-9}. Scale bar = 5 μm. Reproduced from [133].

1.4.5 Evans and Sackmann model

In 1988, Evans and Sackmann published a first model describing the translational and rotational diffusion of cylindrical inclusions in a lipid bilayer supported on a solid substrate, to account for the anomalies observed in the diffusion of molecular probes in supported and unsupported (free) lipid bilayer systems [53]. Contrary to other models, where the transport of momentum into the axial dimension is dominated by the presence of a liquid bulk phase with viscosity η_s, Evans and Sackmann examined the case where momentum coupling is dominated by the presence of a substrate of height h mathematically described by the single frictional parameter b_s. Diffusion coefficients were derived by assuming an intrinsic frictional drag characterizing bilayer-substrate interaction that is linearly dependant on the velocity of the inclusion.

$$D_T = \frac{k_B T}{4\pi\eta_m h\left(\frac{\epsilon^2}{2} + \frac{\epsilon k_1(\epsilon)}{k_0(\epsilon)}\right)}$$

where

$$\epsilon = \sqrt{\frac{b_s}{\eta_m h}} \tag{1.12}$$

and k_0 and k_1 are bessel functions of the second type. Since its development, the Evans and Sackmann model was used, and further developed, to study frictional coupling between lipid bilayers [94], modelling the diffusion of lipid domains in polymer-supported bilayers [180], and understanding the role of curvature on membrane hydrodynamics [43].

1.4.6 Guigas and Weiss model

Although the Petrov and Schwille approximation has fulfilled the need for a simple numerical solution that can be used for modelling the diffusion of micron-sized domains in unsupported (free) model membranes, there is concern over the validity of this approximation in faithfully describing the motion of nanoscopic liquid ordered domains where line tension, lipid interactions and length scale effects could affect the predicted diffusion of membrane inclusions [204]. A mathematical model taking into account, some or all of, the mentioned hydrodynamic effects has, thus far, not been developed.

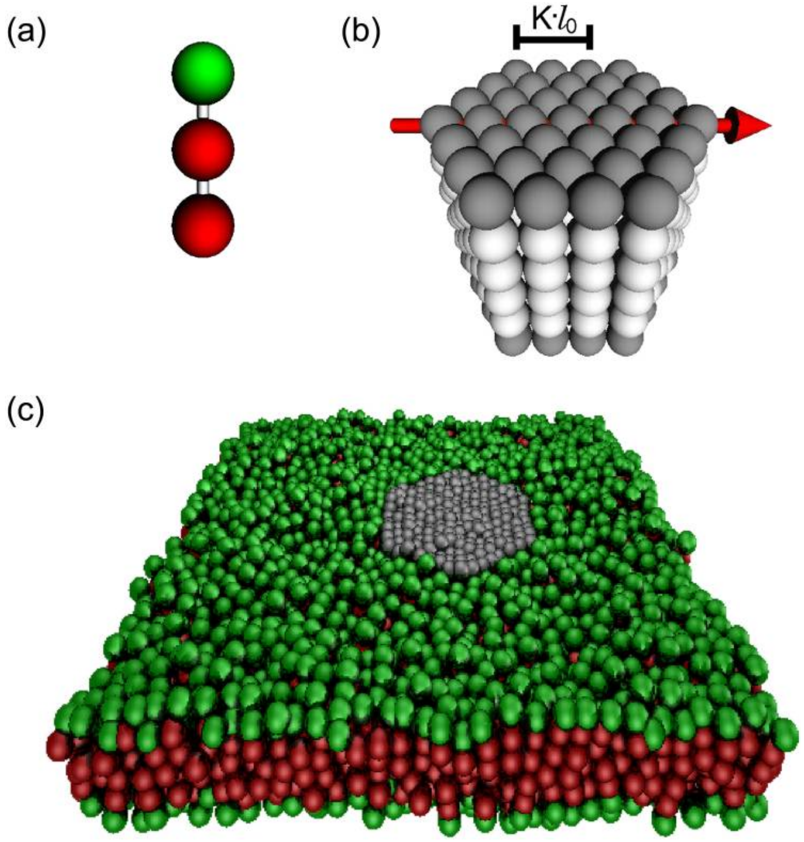

Figure 1.8: Molecular dynamics simulation of a phase-separated lipid bilayer. (a) Unsaturated lipid molecule simulated as three beads interconnected using Hookean springs. (b) Hexagonal S_o lipid domains with edge length $(K+1)l_0$ composed of saturated lipid molecules. (c) Snapshot of a disordered membrane with an embedded S_o domain. Reproduced from [69].

In 2006, Guigas and Weiss published the results of a course-grained molecular dynamics simulation of a diffusing S_o domain in a L_d phase [69]. Unlike other models, their model takes into account the finite compressibility of both the membrane and the surrounding fluid and the internal degrees of freedom which would hamper the diffusion of the embedded domains. Solid hexagonal membrane inclusions with edge length Kl_0 [1] were embedded inside a self-assembling lipid bilayer. The diffusion coefficient and domain radii were recorded simultaneously. The Saffmann-Delbrück model was shown to best describe the diffusion of domains smaller than a critical radius $R_c \approx h\eta_m/(2\eta) \approx 7.4$ nm.

---

[1] K is the average number of lipid head groups at the edge of the hexagonal domain

Beyond the given critical radius, diffusion coefficients were found to strongly deviate from the values predicted by Saffmann and Delbrück as follows:

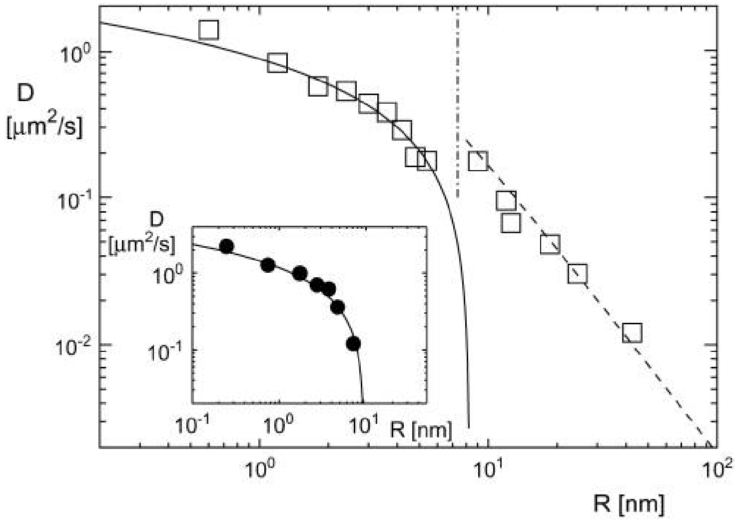

Figure 1.9: Plot of the translational diffusion coefficient versus radius for nanoscopic lipid domains. Suitability of the Saffmann-Delbruck model in describing the diffusion of domains smaller than a critical radius $R_c \approx h\eta_m/(2\eta) \approx 7.4$ nm (solid line). The diffusion of domains larger than the critical radius are best described by $D_T = (k_B T \arctan(c/R))/(8\pi\eta R)$. Reproduced from [69].

Diffusion for domains larger than the critical radius is dominated by the fluid viscosity and is given by the following formula:

$$D_T = \frac{k_B T \arctan(c/R)}{8\pi\eta R} \tag{1.13}$$

where c is an interaction constant and is proportional to the membrane viscosity η_m. Unsurprisingly, the rotational diffusion revealed a dependence on $1/R^2$ as previously eluded to in the Stokes formula. The applicability of this model in the sub 100 nm regime has not been experimentally demonstrated so far due to the lack of a system were appropriately sizable inclusions can be imaged and tracked.

1.5 Segregation of lipid membranes

The partitioning of biological membranes into transient rafts remains elusive [127, 105, 136, 89]. Artificial membrane systems composed of fewer lipid mixtures portray rich phase behaviour. Biological membranes can exhibit such behaviour under non-physiological conditions [110, 16, 70, 112, 194]. However, it remains unknown how lipid phase behaviour in simple mimics could explain the complex organization of biological membranes [46, 166, 73, 55, 89, 63, 113, 164, 28]. This section provides an account of the experiments performed on multi-component artificial bilayers and describes the physical principles of lipid phase separation.

1.5.1 Visualisation of lipid membranes

Lipid phase behaviour has been extensively studied in multi-component artificial bilayers [100, 42, 155, 196, 197, 35, 198, 62, 199, 82, 36]. A hallmark in this field is the 2003 report by Veatch and Keller describing the role of ternary mixtures of phospholipids and cholesterol in inducing macroscopic lipid phase separation [196] and:

A. Demonstrating that a high $\mathrm{T_m}$ lipid (saturated), a low $\mathrm{T_m}$ lipid (unsaturated) and a sterol can produce macroscopic, optically discernable, coexisting phases, and,

B. Quantitatively representing this phenomenon in terms of multi-component phase diagrams.

Dye labelled lipids have been extensively used to visualize lipid phase separation *in vitro* [100, 197, 18]. Fluorescent probes can preferentially partition into the $\mathrm{L_o}$ phase or the $\mathrm{L_d}$ phase. The partitioning behaviour depends on the chemical structure of the lipid and the fluorescent dye attached. In 2007, Baumgart and coworkers documented the preferential partitioning of a wide range of fluorescent lipids in multi-component phase-separated GUVs [18]. More recently, the inefficient partitioning of fluorescent lipids, due to the steric pressure exerted between the large organic dyes has been hypothesized [196, 197, 195, 82, 123].

1.5.2 Lipid phase diagrams

Lipid phase diagrams map out regions of phase coexistence in two dimensional space in respect to the molar fraction of lipids present within individual multi-component lipid bilayers. Multiple phase diagrams must eventually be used to examine how lipid phase behaviour changes with temperature and pressure. Lipid phase diagrams have been typically constructed for binary and ternary lipid mixtures but have also been recently constructed for quaternary lipid mixtures (subsection 1.5.4).

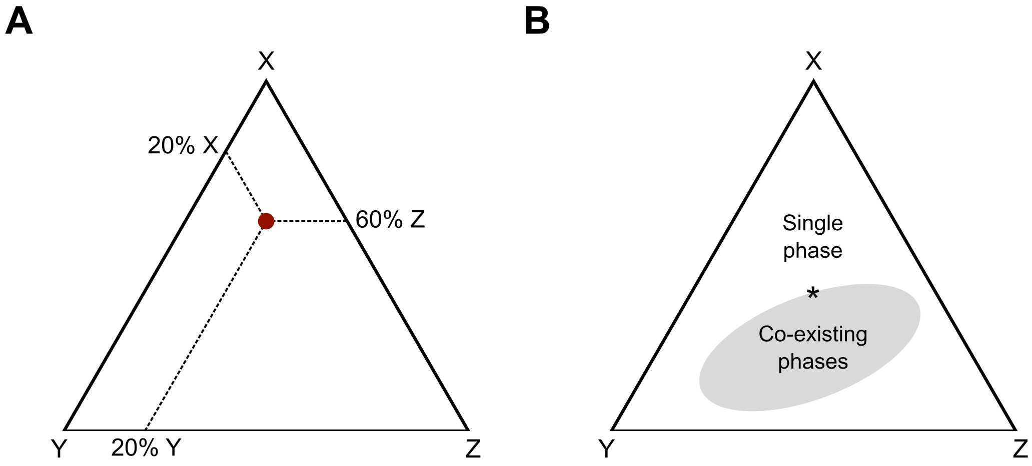

Figure 1.10: Lipid phase diagrams can be used to visually represent the organizational state of a multi-component lipid membrane at any composition. (A) The number of phases in a lipid membrane composed of a ternary lipid mixture (X,Y and Z) can be deduced by extending lines from points of corresponding relative molar composition at 120°. The point of intersection of these lines can lie in a space that represents the presence of a single phase or multiple co-existing phases as shown in (B). Critical point is represented as an asterisk at the phase boundary.

Construction of lipid phase diagrams is mathematically governed by the Gibbs phase rule which dictates that the number of components C in a system equals the sum of the number of independent intrinsic variables or the degrees of freedom F and the number of phases in thermodynamic equilibrium P. Mathematically, this can be expressed as follows:

$$F = C - P + 2 \tag{1.14}$$

where the constant 2 is introduced to account for the variability of temperature and pressure. The Gibbs phase rule has numerous implications, most importantly, that the number of phases exhibited in cellular membranes is large due to the large number of different lipid components in living cells. Consider a bilayer with two lipid components, A and B, where A is a high-transition temperature lipid and B is a low-transition temperature lipid. At temperatures higher than the transition temperatures of both A and B, a single uniform liquid phase dominates the bilayer. At temperatures lower than the transition temperature of either, A or B, the bilayer segregates into two distinct, co-existing, phases. Regions of phase coexistence, at defined temperatures, are identified on phase diagrams and distinguished from regions of single phase existence (figure 1.10). Regions where the coexisting phases have close to identical compositions are critical points and can also be marked on phase diagrams. The subtle, and often indistinguishable, chemical properties of coexisting phases, at critical points, drive the system into a state of dynamic equilibrium. Numerous processes of biological relevance are thought to occur at these points.

1.5.3 Dynamics of lipid domains

Lipid phase separation is a time-dependant process. This aspect is not conveyed in a phase diagram. Since molecules in the cell membrane are in constant motion, it is important to understand and model the diffusion and coarsening of lipid domains and their effects on the dynamics, and function, of membrane components.

Diffusion of lipid domains

In 1993, Klingler and McConnell reported the diffusion of micron-sized S_o domains in fluid lipid monolayers formed at an air/water interface [97]. Abrupt pressure differentials were applied to regions of phase coexistence in phase separated monolayers composed of DPPC and DMPE to force the isolation of appropriately-sized domains, which were tracked. DPPC domains in a

DMPE phase showed different diffusion from DMPE domains in a DPPC phase, thereby confirming the dependence of the diffusion of domains on the bilayer's viscosity. It was not until 2006 that macroscopic lipid domains in GUVs composed of ternary lipid mixtures were tracked [34] and the diffusion was compared to those predicted by diffusion models (section 1.4). L_d domains were tracked in a DPPC-rich L_o phase over a range of molar compositions and temperatures. The reported diffusion coefficients agreed with values calculated using the mathematical model developed by Saffmann and Delbrük at the small domain size limit, and with an approximation of the HPW model for large-sized domains. Increasing the molar composition of DPPC reduced the mobility of the L_d domains whilst reducing the concentration of cholesterol did not affect the system's performance. Notably, Cicuta and coworkers were the first to report a value for the membrane viscosity $\approx 10^{-8} - 10^{-7}$ Ns/m for the DPPC-rich bilayer membrane. Later, Petrov and coworkers tracked diamond-shaped S_o domains on the upper pole of osmotically tensed GUVs electroformed from a binary mixture of DPhPC and DPPC [133]. The asymmetric nature of the observed domains facilitated the tracking of their orientations.

Translational and rotational diffusion coefficients were consistent with the numerical approximation of the HPW model developed by Petrov and Schwille [134] with a membrane viscosity value of $\approx 10^{-9}$ Ns/m for the fluid DPhPC-rich L_d phase - an order of magnitude lower than that previously reported value for a DPPC-rich phase.

Coarsening of lipid domains

Coalescence and dynamic changes in the size of lipid rafts could be responsible for the dynamic organization of proteins in biological membranes [164]. Quantifying the coarsening dynamics, and the associated line tensions, of macroscopic lipid domains correlates with understanding the putative role of lipid rafts. In 1992, Benvegnu and McConnell published their first attempts in measuring the line tension of L_o lipid domains by hydrodynamic distortion [23]. By applying a flow shear across the fluid sub-phase and removing the shear following the distortion, the line tension of circular lipid domains was calculated from the velocity of restoration. Later in 2003, Baumgart and coworkers imaged, and modeled, tension-induced curvature and shape-transitions in model membranes [17]. Abrupt reduction in the line tension between coexisting phases is expected at critical points [198, 62] and, therefore, a quantitative description of the abrupt decrease in line tension at critical points is important for understanding the out of equilibrium dynamics occurring in biological membranes. In 2008, Honerkamp-Smith and coworkers quantitatively evaluated fluctuations at the L_o / L_d phase boundaries near critical compositions and temperatures [194] and highlighted that line tension would drop down to zero as the temperature of the system approaches the critical temperature. Although these, and other, results [188] strongly suggest their existence, transient nanoscopic lipid domains have not yet been observed.

1.5.4 Quaternary lipid mixtures

It has, thus far, been possible to accurately measure, and model, diffusion coefficients and line tensions in multi-component phases-separated model membranes, but, the imprecise sampling of critical compositions has not permitted the extrapolation of these measurements to transient nanoscopic lipid domains. The range of critical compositions of ternary lipid mixtures is challenging to sample due to its strong temperature dependance. A solution to this problem was recently suggested, in that quaternary lipid mixtures possess critical contours which can be effectively sampled in a range of model systems [99, 65, 1].

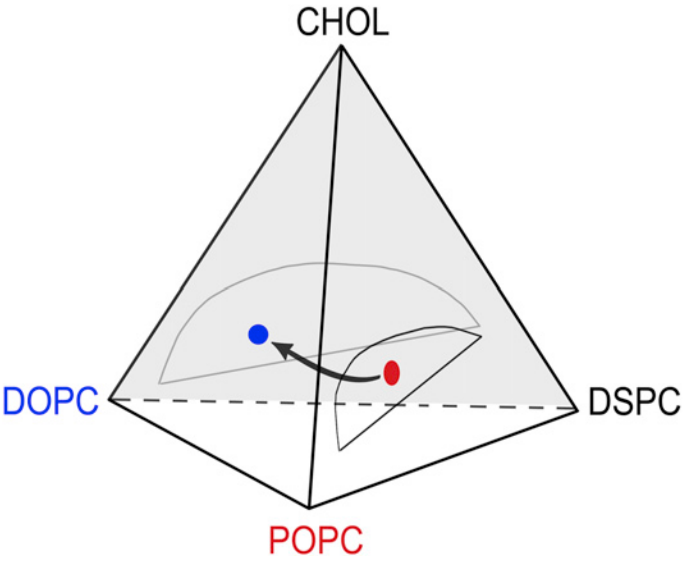

Figure 1.11: Lipid phase diagram for the quaternary lipid mixture DSPC, DOPC, POPC and Chol showing different regions of phase coexistence. Reproduced from [65].

Sub 100 nm Small Unilamellar Vesicles (SUVs) composed of the quaternary lipid mixture DSPC, DOPC, POPC and Chol were examined using Förster Resonance Energy Transfer (FRET), Small-Angle Neutron Scattering (SANS) and Electron Spin Resonance (ESR) [76]. Similar to ternary mixtures, where the modulation of the height mismatch between different coexisting phases can modulate the size of micron-sized domains [62], it was shown that modulation of the height mismatch between coexisting phases, induced by varying the ratio of the unsaturated lipid DOPC to the saturated lipid DSPC, can modulate the size of nanoscopic lipid domains. The molar fraction, ρ, is a characteristic parameter of the mentioned measurements and is defined as follows:

$$\rho \equiv \frac{[\mathrm{DOPC}]}{[\mathrm{DOPC}] + [\mathrm{DSPC}]} \tag{1.15}$$

Although the modulation in the size of nanodomains was not directly observed, Monte Carlo fits to obtained SANS data revealed a linear dependence of the average radii of the nanodomains on ρ. Domain radius varied between 0 nm ($\rho = 0$) to 15 nm ($\rho = 0.35$).

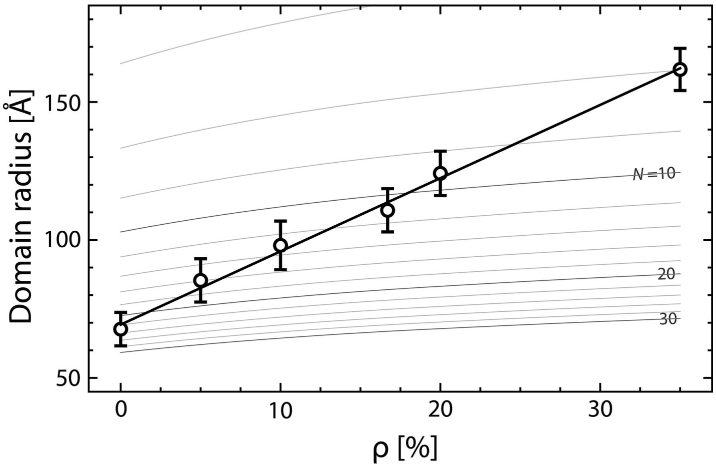

Figure 1.12: Modulation of the size of nanoscopic lipid domains in quaternary lipid mixtures by varying the relative molar ratio ρ of the saturated lipid (DOPC) to the unsaturated lipid (POPC). Domain sizes have been deduced from fitting Monto Carlo to SANS data. The fit reveals a linear increase of the size of domains with increase in ρ. Reproduced from [76].

1.5.5 Effect of protein binding on lipid phase behaviour

There is substantial evidence suggesting a link between the segregation of lipids with signal transduction [165, 163, 108, 193, 176, 4], trafficking [126, 139, 78, 189, 74] and viral recognition [128, 157, 167, 143, 33, 203, 31, 29, 178]. It remains unclear whether these effects are driven by lipid phase separation or another membrane organizing principle (chapter 4). To reduce the complexity of the problem, the interplay between proteins and lipid phase separation has been studied *in vitro* as shown below.

Integral proteins

In 2013, Scheve and coworkers provided evidence suggesting that steric hindrance between integral proteins opposes the formation of macroscopic lipid phases [158]. Ubiquitin, transferrin, GFP and transferrin receptors were found to contribute to the dissolution of domains beyond a certain concentration threshold that is proportional to the mass of the different proteins.

Peripheral proteins

In as much as integral proteins seem to contribute to the destruction of macroscopic lipid phases, numerous peripheral proteins were reported to employ the boundaries of coexisting phases as binding sites, for example:

A. The HIV-1 glycoprotein (gp41) was reported to bind at the edges of cholesterol-enriched lipid domains and promote viral membrane fusion [202].

B. The multi-function Rac1 protein was recently found to get translocated at the boundary of coexisting phases [122].

C. Here, monomers of the pore forming toxin, Equinatoxin (Eq) II, are also shown to bind to the boundaries of the L_o/L_d coexisting phases before diffusing into the L_d phase [148] to form pores.

Filamentous proteins

The interplay between the binding of filamentous proteins (eg. actin and FtsZ) and lipid phase separation was recently investigated in GUVs and SLBs [84, 11, 115, 114]. The binding of filamentous proteins to multi-component lipid membranes was found to mediate temperature-resistant macroscopic lipid phase separation (figure 1.13). These results were benchmark against single-component membranes where the binding of filamentous proteins was found not to induce any discernable lipid phase separation. These findings explain the presence of macroscopic islands in biological membranes where protein diffusion is hindered and, importantly, reconciles two membrane organization models, the lipid rafts and picket fence, which were once thought to be distinct.

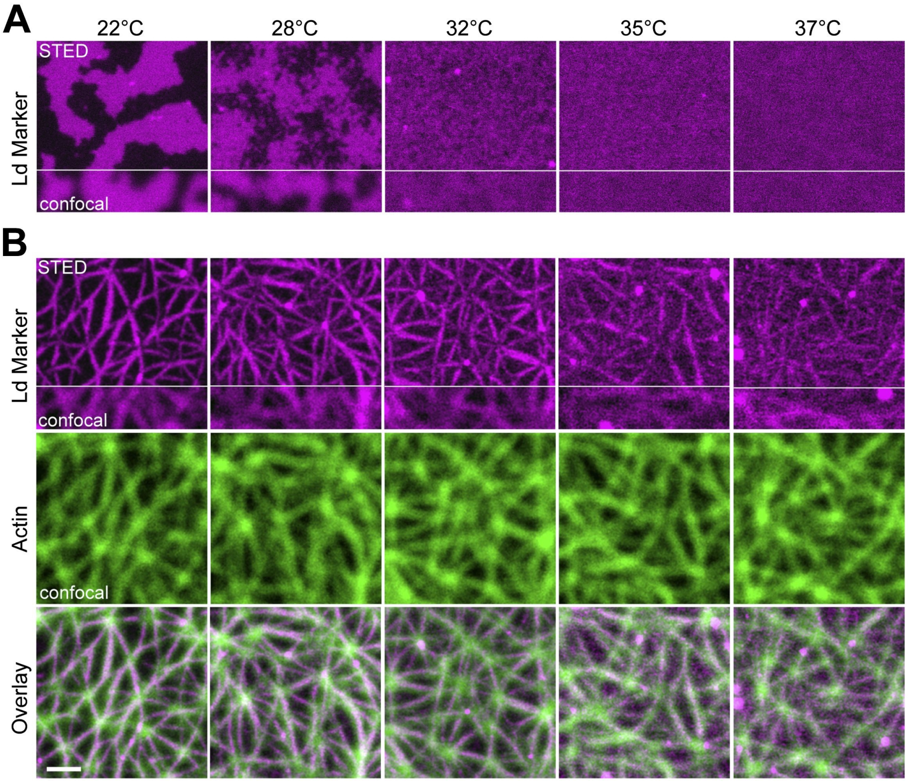

Figure 1.13: Actin induced temperature-resistant lipid phase separation in SLBs composed of a ternary mixture of DPhPC, DPPC and Chol labelled with trace amounts of DPPE-KK114 as a marker for the L_d phase. (A) Without Actin. (B) With Actin bound; lipid phase separation persists as temperature of the bilayer is elevated above the transition temperature of DPPC (≈ 41°C). Scale bar = 1 µm. Reproduced from [84].

2

Technique development

The development of protocols and methods for the formation and imaging of phase-separated DIBs forms a substantial part of this dissertation. This chapter provides detailed materials and methods for:

A. The formation of DIBs.

B. Imaging phase-separated DIBs.

C. Data processing and analysis.

2.1 Materials

2.1.1 Lipids

All lipids were obtained from (Avanti Polar Lipids, Alabama, US) unless otherwise indicated. All lipids were stored at -20°C until used. The following are all the lipids used in the experiments described in this dissertation: DPhPC (1,2-diphytanoyl-sn-glycero-3-phosphocholine), DPPC (1,2-dihexadecanoyl-sn-glycero-3-phosphocholine), DOPC (1,2-Dioleoyl-sn-glycero-3-phosphocholine), POPC (1-palmitoyl-2-oleoyl-sn-glycero-3-phosphocholine), eSM (egg Sphingomyelin) (Sigma Aldrich, Dorset, UK), bSM (brain Sphingomyelin), TRITC-DHPE (N-Tetramethylrhodamine-6-thiocarbamoyl-1,2-dihexadecanoyl-sn-glycero-3-phosphoethanolamine, triethylammonium salt), DiI-C18 (1,1-dioctadecyl-3,3,3,3-tetramethylindocarbocyanine), ATTO-488 DPPE (ATTO-TEC, Siegen, Germany) and Chol (Affymetrix, High Wycombe, UK). Lipid stocks were prepared as follows: lyophilized lipids in their powder form were dissolved in excess (700 µL) of chloroform (Sigma Aldrich) and transferred to pre-weighed Teflon-capped vials. Gentle nitrogen flow was used to evaporate all chloroform. Vials were kept under vacuum for at least 1 hour and reweighed. Stocks of lipid(s) in chloroform at 50 mgmL^{-1} were prepared by dissolving the weighed mass of lipids in the appropriate volume of chloroform and stored at -20°C until required. Lipid stocks were replaced every 6 months.

For each experiment, the desired amounts of required lipid in chloroform stocks were mixed in a Teflon-lidded vial, dried under a gentle stream of nitrogen and vacuum applied for at least 30 minutes. The dried lipid content of the vial was dissolved in the volume of hexadecane needed to reach the required lipid concentration (8.7 mgmL^{-1}) and transferred to a dry bath, pre-heated above the transition temperature of all lipid components, for 5 minutes. This allowed for the homogeneous mixing of lipids prior to DIB preparation. One half of the solution was transferred to another Teflon-lidded vial where 10% of Silicone oil AR-20 (Sigma Aldrich), was added. Both lipid containing vials were allowed to cool for up to 1 hour until DIB preparation.

2.1.2 Agarose

Buffers were prepared as follows: 90 mM buffer solution of HEPES (H3375, Sigma Aldrich) was made with 18.6 MΩ ultra pure deionized water (Milli-Q, Merck Milli, Watford, UK) and the pH was adjusted to 7.0 with NaOH. A stock of 20 mL was stored in a sterilised 50 mL Falkon tube (Fischer Scientific, Loughborough, UK) at 4°C for up to 3 months until required. In 1.5 mL Eppendorf tubes, a 2.8 mgmL^{-1} solution of low melt agarose (A9414, Sigma Aldrich) in deionised water and a 0.75 mgmL^{-1} solution of ultra low melt agarose (A5030, Sigma Aldrich) in buffer were melted in a temperature-controlled mixer (Eppendorf, Hamburg, Germany), set at 90°C, for 20 minutes. The solutions were incubated at that temperature for up to 1 hour until required.

2.2 Device fabrication

Droplets were incubated and DIBs formed in PMMA devices, which were developed and manufactured in-house [109] (figure 2.1). Each well of the “incubation chamber” accommodates 8 droplets (200 nL each), and each of the 16 wells of the “device” accommodates an individual bilayer. Following fabrication, the incubation chamber and device were washed and stored in 30% ethanol. Immediately prior to use, they were washed with deionised water, then ethanol and finally dried under nitrogen.

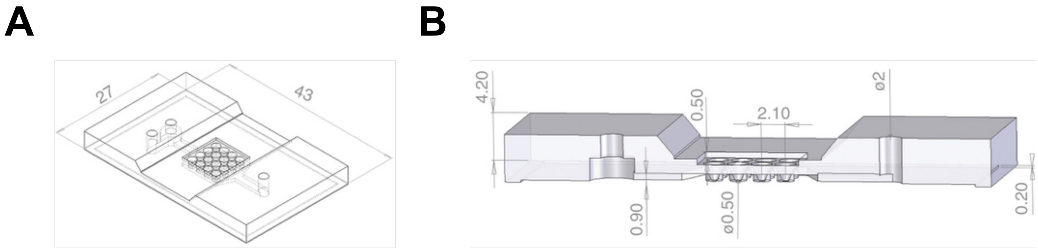

Figure 2.1: Schematic diagram of a device. (A) Isometric projection and (B) cross-section. Dimensions in mm.

2.3 DIB preparation

Phase-separated DIBs are constructed using the following protocol adapted from [109]:

A [00:00 - 00:03 h] 20 µL of lipids in hexadecane and silicone oil is used to fill each well of the incubation device. 8 droplets (50.2 nL each) are injected in each well using a piezo-driven injector (World Precision Instruments, Florida, US) as shown in figure 2.3A.

B [00:03 - 00:10 h] A 24 mm x 40 mm, n.1 thickness, glass cover slip (Gerhard Menzel, Braunschweig, Germany), are plasma cleaned in a Femto plasma cleaner (Diener Electronic, Ebhausen, Germany), for 7 minutes at 0.2 bar of oxygen as shown in figure 2.3B.

C [00:13 - 00:15 h] The plasma-cleaned cover slip was coated with 140 µL of ultra low melt agarose solution spun at 4000 rpm for 30 minutes using a spin coater (WS-650MZ-23NPP/LITE, Laurell, Pennsylvania, US) as shown in figure 2.3C.

D [00:15 - 00:16 h] The agarose-coated cover slip is then placed underneath a device and secured at the edges with adhesive tape to reduce evaporation and prevent liquid leakage (figure 2.3D).

E [00:16 - 00:18 h] The spaces surrounding the wells are filled with 180 µL molten low melt agarose solution. Once the agarose solution sets, the device is secured with adhesive tape on top (figure 2.3E).

F [00:18 - 00:23 h] The wells are, subsequently, filled with 50 µL of the lipids in hexadecane solution previously described (figure 2.3F).

G [00:43 - 00:45 h] Individual droplets are transferred from the incubation chamber to the wells of the device using a pipette (figure 2.3G).

H The device is then placed inside a preheated drying cabinet set at 45 °C for 25 minutes (figure 2.3H). Alternatively, the device could also be heated on top of a hotplate set at 45 °C for 6 - 7 minutes. However, the drying cabinet heats the device isotropically and was used for experiments described here.

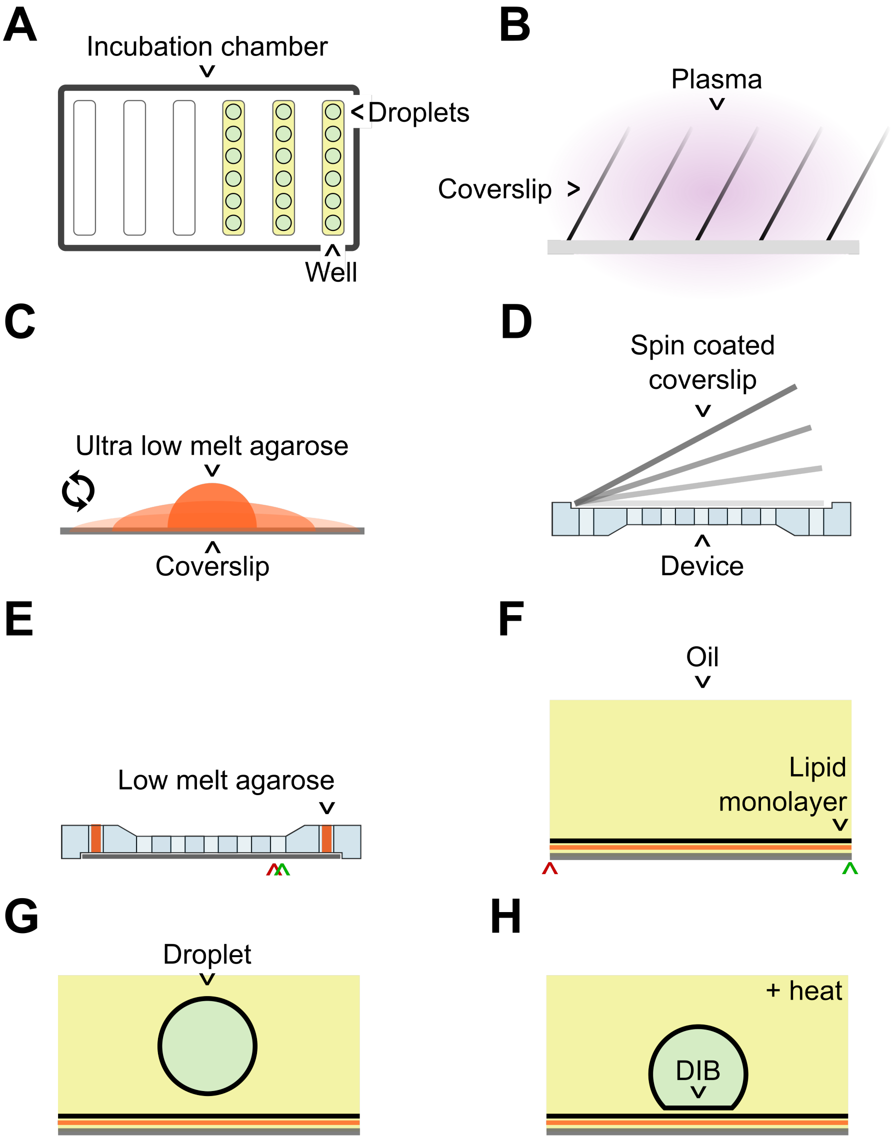

Figure 2.2: Steps involved in the formation of DIBs. (A) Aqueous droplets incubated in a lipid in oil solution. (B) Coverslips are cleaned in a plasma cleaner. (C) Plasma cleaned coverslip is spin coated with a solution of ultra low melt agarose solution. (D) Agarose coated coverslip is inserted in a grove at the bottom of the device (shown upside down) and sealed. (E) Low melt agarose fills the gaps between the wells. (F) Solution of lipids in oil is injected into the wells and a lipid monolayer forms over the hydrogel film. (G) Incubated droplets are transferred from the incubation tank and inserted into the wells of the device. (H) Device is heated and bilayer forms. Figure not to scale.

2.4 DIB visualisation

Optical microscopy is one of the primary experimental techniques used for the study of membrane organization and dynamics. This section briefly covers the principle of operation of Total Internal Reflection Microscopy (TIRF) and interferometric Scattering microscopy (iSCAT); the two techniques used in this dissertation to image lipid phase separation in DIBs.

2.4.1 Total internal reflection fluorescence microscopy

Total Internal Reflection (TIR) is a well established optical phenomena whereby light incident at an angle θ above a critical angle θ_c, dictated by Snell's law, is reflected at the interface between two media with different refractive indices n_1 and n_2. To account for the continuity of Maxwell's equations at the interface, a small portion of the reflected wave is transmitted perpendicular to the plane of reflection. On component of the transmitted wave is evanescent and decays exponentially along the axis perpendicular to the surface [13]. In Cartesian coordinates, the intensity of the evanescent field is expressed as follows:

$$I(z) = I_0 e^{-z/d} \tag{2.1}$$

Where z is the direction of propagation of the evanescent wave and d is is depth of penetration expressed as follows:

$$d = \frac{\lambda_0}{4\pi\sqrt{n_1^2 \sin^2\theta - n_2^2}} \tag{2.2}$$

λ_0 is the wavelength of the incident light and θ is the angle of incidence. From equation (2.34) It is evident that d is proportional to λ_0 and inversely proportional to θ. Therefore, the depth of the evanescent field does not exceed 100 nm for visible light. By limiting the fluorescence emission to a narrow region thus providing a high signal to noise ratio. TIRF microscopy is routinely used to image single-molecule and ensemble fluorescence in DIBs [67, 182, 75, 79, 148] as the agarose substrate is thin enough to allow the evanescent field to illuminate the bilayer.

2.4.2 Interferometric scattering microscopy

Reflection is the scattering of light from a flat surface where the electric field components constructively interfere. Two major forms of scattering exist: elastic scattering, where no energy transfer is involved, and inelastic scattering, where energy is transferred between electromagnetic radiation and matter. Although inelastic scattering techniques can be used for imaging lipid phase separation [6], this work is concerned with the detection of elastically scattered photons. Scattering modes can be differentiated by the size parameter α expressed as follows:

$$\alpha = \pi d / \lambda \tag{2.3}$$

where d is the diameter of a particle and λ is the excitation wavelength. For $\alpha << 1$, Rayleigh scattering dominates, for $\alpha \approx 1$ Mie scattering dominates and for $\alpha >> 1$ geometric scattering, or reflection, dominates. For most biological applications, however, where the dimensions of the imaged entity is approximately ten times smaller than the wavelength of the excitation source, the Rayleigh approximation suffices to predict and characterise the emerging scattering field. According to the Rayleigh approximation, the scattering amplitude s by a sphere of diameter d is given by:

$$s = \eta n_m^2 \pi \frac{d^3}{2} \left(\frac{n_p^2 - n_m^2}{n_p^2 + 2n_m^2} \right) \tag{2.4}$$

The total intensity I_{det} received at the detector following excitation is composed of a static background term (reflection) "b", a scattering term "s" and an interference term "$bs \sin\theta$". I_{det} is expressed as:

$$I_{det} = I_b + I_s = (E_b + E_s)^2 = E_i^2 (b^2 + s^2 - 2bs \sin\theta) \tag{2.5}$$

Assuming that the contribution of the scattering signal s^2 is negligible for a nano-sized object, equation 2.5 is reduced to:

$$I_{det} = I_b + I_s = (E_b + E_s)^2 = E_i^2 (b^2 - 2bs \sin\theta) \tag{2.6}$$

One successful approach for label-free imaging can be deduced from equation 2.6. The interference term ($bs\sin\theta$) scales linearly with s and, consequently, with d^3. To facilitate comparison between intensity values, the contrast C is defined as:

$$C \equiv \frac{I_{det}}{I_b} = 1 - \frac{2s\sin\theta}{b} \tag{2.7}$$

Interference Reflection Microscopy (IRM), which operates on the detection of the interference between reflections from different interfaces at different heights, was first adapted by Curtis in 1964 [39] to visualize cell adhesion and later used for imaging phase separation in lipid monolayers [92]. In 2004, the lab of Vahid Sandoghar developed Interferometric Scattering (iSCAT) microscopy [111] to track the position and orientation of single virus particles (VLPs) [102]. The difference between iSCAT and IRM is that the background signal "b" is removed during post processing by averaging all frames in a video. By employing faster and more sensitive Complementary Metal Oxide Semiconductor (CMOS) cameras, iSCAT is now capable of imaging in the microsecond regime, at the single molecule level and with nanometer localization precision.

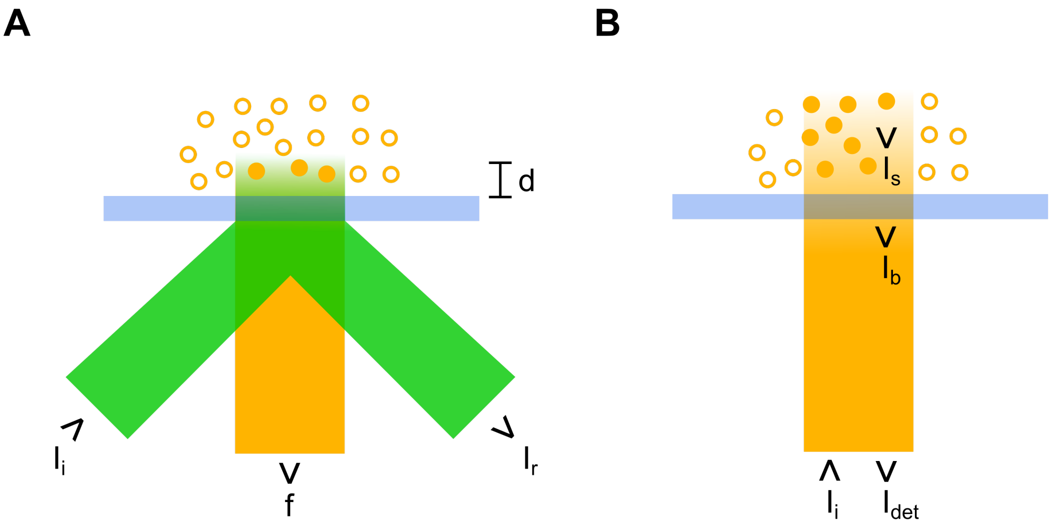

Figure 2.3: Schematic diagram showing the principle of operation of (A) TIRF and (B) iSCAT. In TIRF, an evanescent wave propagates perpendicular to the plane of an interface for a distance ($d \approx 100$ nm) exciting all molecules at the vicinity of the interface and the fluorescence emission (f) is collected. In iSCAT, the superposition of the wave scattered by nano-sized objects (I_s) and the wave reflected by macroscopic objects (I_b) is detected (I_{det}) and the background signal is removed in the post processing.

In 2009, Kukura and coworkers demonstrated the label-free tracking of the position and orientation of Simian 40 Virus Like Particles VLPs [102]. VLPs were labelled using Quantum Dots (QDs) and tracked on SLBs using fluorescence and iSCAT to reveal exclusive diffusion traits. In another report by Piliarik and Sandoghar, label-free optical detection of single proteins was demonstrated on four different proteins ranging from 65 kDa to 340 kDa [137]. The reported contrast scaled linearly with their molecular weights, compliant with the assumption that the density and refractive index of the four proteins is naively similar, and, therefore, the contrast signal is proportional to the volume of the proteins. These, and other reports [130, 7], demonstrate the ability to image and track nano-sized biological objects which could have not been imaged using fluorescence microscopy alone.

2.5 Experimental setup

2.5.1 Fluorescence microscope setup

All optical components were obtained from (Thorlabs, New Jersey, US) unless otherwise stated. A 532 nm ND:YAG diode-pumped solid state laser (SLIM-532, Oxxius, Lannion, France) was collimated and launched into a 450-600 nm single mode (460 hp) optical fiber a 2 mm molded glass aspheric lens (352150-C). Light out of the fiber was coupled to an optical fiber port of a TIRF Eclipse Ti microscope (Nikon, Tokyo, Japan) passing through a 545/650 nm bandpass dichroic filter (FF545/650-Di-01, Semrock, New York, US) and finally into a 60x, 1.45 Numerical aperture and oil immersion TIRF illuminated microscope objective (Nikon). fluorescence emission was imaged by an EM-CCD chip (iXon 3, Andor, Belfast, UK) after passing through a 532nm long pass emission filter (BLP01-532R-25, Semrock). A schematic diagram for the described experimental setup is shown in figure 2.4.

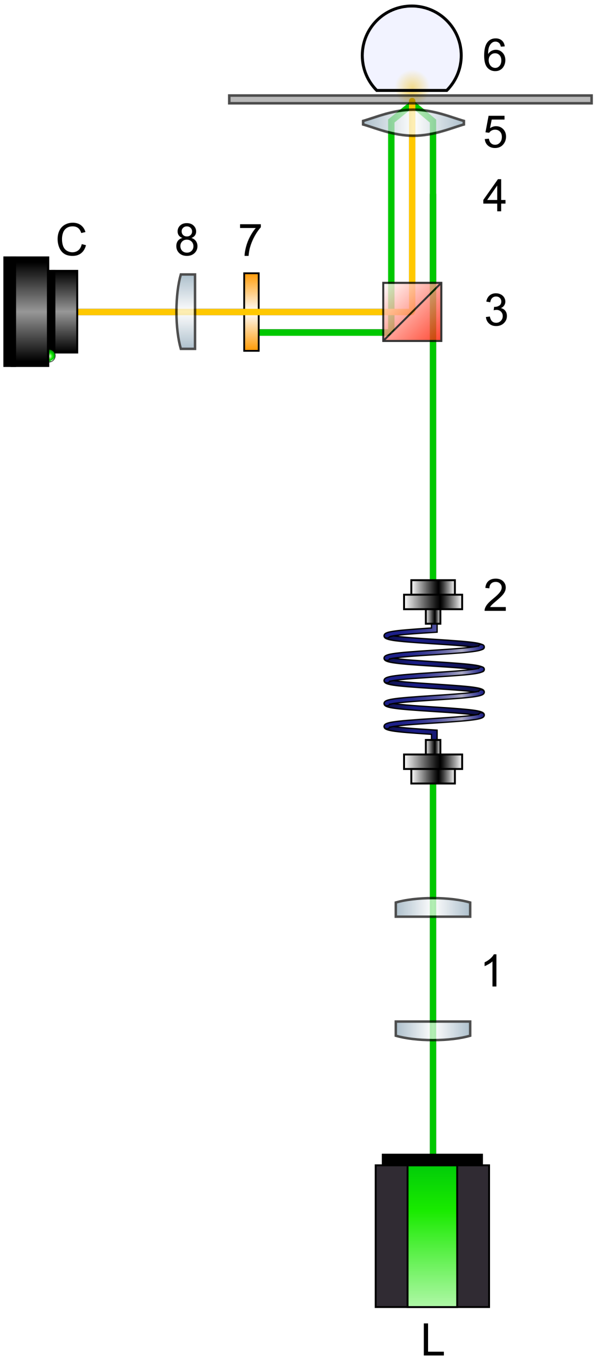

Figure 2.4: Schematic diagram of the TIRF microscopy setup. L: Laser, 1: collimation lenses, 2: single mode fiber, 3: dichroic mirror, 4: objective lens, 5: glass coverslip, 6: droplet, 7: emission filter, 8: tube lens, C: camera.

2.5.2 iSCAT and TIRF microscope setup

For iSCAT, the output of a 662 nm diode laser (Obis, Coherent, California, US) was collimated to 2 mm beam diameter before passing through two acousto-optic Deflectors (AODs) (Gooch and Housego, Ilminster, UK). The two AOD channels were scanned in a saw tooth by separate phase-locked function generators (DG 1022, Rigol, Reading, UK) at 79 and 80 kHz, respectively. The beam deflected by the AODs was imaged with telecentric lenses onto the back focal plane of 60x, 1.45 Numerical aperture and oil immersion TIRF illuminated microscope objective (Plapon, Olympus, Tokyo, Japan) after passing through a polarizing beam splitter. The scanned beam under fills the back aperture of the objective to generate a focal spot of $\approx 1\mu$m. A quarter wave plate placed before the objective causes the p-polarised incident light to be converted into a s polarized light after reflection from the sample. The light reflected by the polarizing beam splitter was detected by a CMOS camera (MV-D1024-160-CL-8, Photonfocus, Lachen, Switzerland) at 250× magnification.

For combined TIRF and iSCAT, a 473 nm diode laser (Crystal Laser, Nevada, US) was focused at the back aperture of the objective to totally internally reflect off the sample. The beam generated a wide field illumination spot with FWHM = 15 µm. The beam is reflected off a 505 nm long pass dichroic mirror. A 605 nm long pass dichroic mirror transmits the 662 nm beam. Fluorescence in the 505 nm to 605 nm window is separated from both the reflected 662 nm beam and 473 nm beams by the two dichroic mirrors. After passing through a 550 nm long pass filter, the fluorescence emission is imaged on to an EM-CCD chip (iXon 860, Andor). A schematic diagram for the described iSCAT setup is shown in figure 2.5.

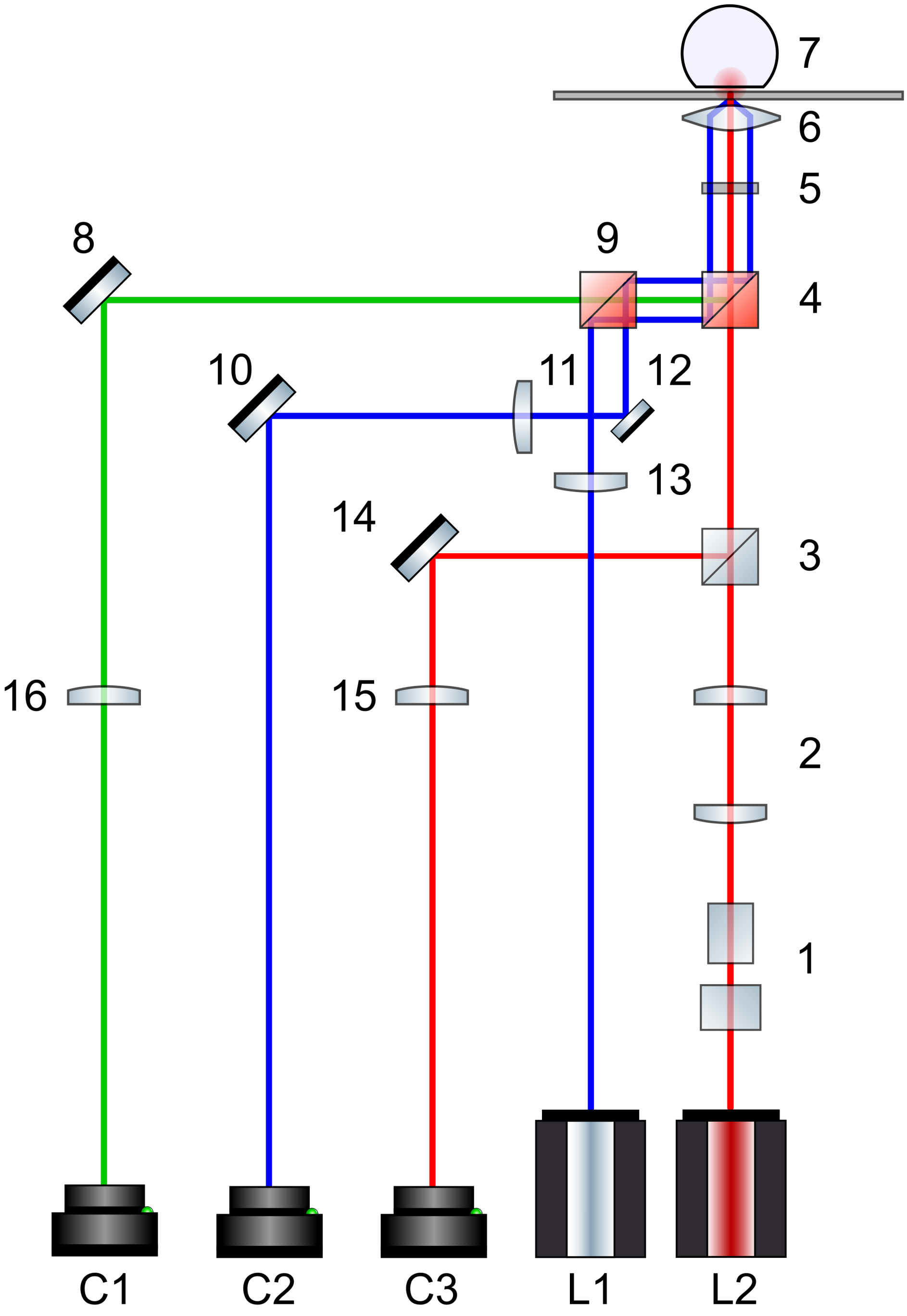

Figure 2.5: Schematic diagram of the iSCAT microscopy setup. L1: 473 nm Laser, L2: 660 nm laser, 1: AODs, 2: collimation lenses, 3: PBS, 4: long-pass dichroic mirror, 5: quarter wave plate, 6: objective lens, 7: sample, 8: mirror, 9: long pass dichroic mirror, 10: mirror, 11: tube lens, 12: mirror, 13: tube lens, 14: mirror, 15: tube lens, 16: tube lens, c1: EM-CCD, C2: CMOS camera and C3: CMOS camera.

2.6 Data processing

2.6.1 Image processing

The constant background in iSCAT images is removed by recording 1000 images while manually moving the sample stage. Each pixel is then replaced by the temporal median value of the frame sequence to generate an optimal flat field image that is independent of the sample.

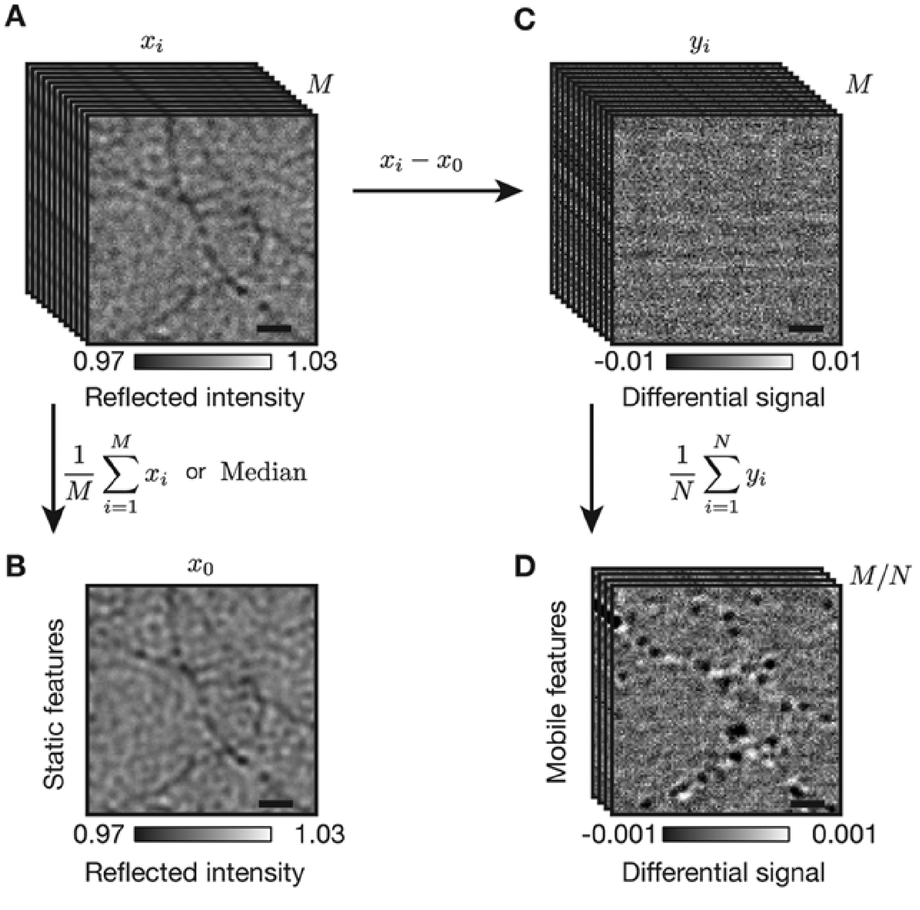

Figure 2.6: Processing of iSCAT images. A background image (B) of a stack (A) is obtained by summing the individual pixels across all the frames of the stack and dividing by the total number of frames of the stack. A differential stack (C) is obtained by dividing each frame of the stack (A) by the background image (B). To enhance the contract, consecutive sub stacks are averaged into single images and eventually concatenated to produce the final reduced stack (D). Reproduced from [130]

Following division by the flat field image, sample-specific images with shot noise limited sensitivity are obtained [130]. Focus was maintained by feedback control of the sample stage by detecting the reflected 473 nm beam on a CMOS chip. The feedback loop operates at 20 Hz, keeping the z position within 5 nm of the target.

2.6.2 Particle tracking

The centroid positions and contrast values were obtained by fitting objects in the image to Gaussian Point Spread Functions (PSF) of the general form:

$$f(x,y) = A\exp\Big[\frac{-1}{2(1-c^2)}\Big((\frac{x-x_0}{\sigma_x})^2 + (\frac{y-y_0}{\sigma_y})^2 - \frac{2c(x-x_0(y-y_0)}{\sigma_x\sigma_y}\Big)\Big] \tag{2.8}$$

Particle tracking was performed by the ImageJ Trackmate algorithm[1] [91] which employs a Laplacian of Gaussian (LoG) filter for detection. The Half-Width Half Maximum (HWHM), contrast and diffusion coefficient were calculated for each trajectory using a home-written MATLAB protocol (Appendix B.2).

2.6.3 Processing and tracking microdomains

Microdomain tracking was carried out by a home-written MATLAB protocol (Appendix B.2). Briefly, a Gaussian profile, corresponding to the illumination pattern, was divided from the raw stacks to create a flat background. Domains were identified by thresholding normalised images and rejecting all objects above or below a certain area range and which are not circular. The identified objects were, consequently, tracked by a closest-neighbour algorithm.

2.6.4 Mean squared displacement calculation

For each track, the MSD was calculated using a running-average function whereby, for a time difference Δt_n, x and y positions, the MSD is represented

---

[1] Downloaded from http://fiji.sc/TrackMate. Maintained by Jean-Yves Tinevez (jean-yves.tinevez@pasteur.fr).

as:

$$MSD(\Delta t_n) = \frac{1}{N-n+1}\sum_{j=0}^{N-n}([x(j\delta t+n\delta t)-x(j\delta t)]^2+[y(j\delta t+n\delta t)-y(j\delta t)]^2) \tag{2.9}$$

Where N is the total number of frames in a stack and n is size of the averaging window. Lateral diffusion coefficients, D, are calculated from the average value of the MSD which in turn is calculated by fitting a linear function to the obtained $MSD(\Delta t_n)$ and weighting the fit to the standard deviation of the errors in the mean squared displacement. The diffusion coefficients and measured radii of the identified objects were fit with different diffusion models (section 1.4).

3

Fluorescence imaging and characterisation of lipid phase separation in droplet interface bilayers

DIBs are configurable, substrate-supported, fluid membrane systems, which can be accessed using a wide range of optical microscopy techniques and have been employed in studying a number of biological processes (subsection 1.3.3). In this chapter, I examined multi-component phase-separated DIBs using fluorescence microscopy. The following experiments are described:

A. Sampling regions of lipid phase diagrams;

B. Measuring the diffusion of lipid domains in phase separated DIBs;

C. On-demand control of lipid composition in DIBs;

D. Imaging the lipid phase-dependent pore formation of Equinatoxin II;

E. Imaging electroporation in phase separated DIBs

3.1 Solubility of ternary lipid mixtures in hexadecane

Lipid phase separation has not been previously reported in DIBs. The solubility of different lipid mixtures in hexadecane was examined. Three mixtures were used: DOPC and bSM; DOPC, bSM and Chol; DOPC, POPC, bSM and Chol. The stocks in chloroform were transferred to separate Teflon-capped vials and subjected to nitrogen until a lipid film formed at the bottom of each vial. Hexadecane was titrated to each vial and the solubility was measured at different temperatures (figure 3.1).

3.1.1 Results

With the exception of the solubility of (DOPC and bSM) which increases with temperature, the solubility of (DOPC, bSM and Chol) and (DOPC, POPC, bSM and Chol) was not found to increase with temperature.

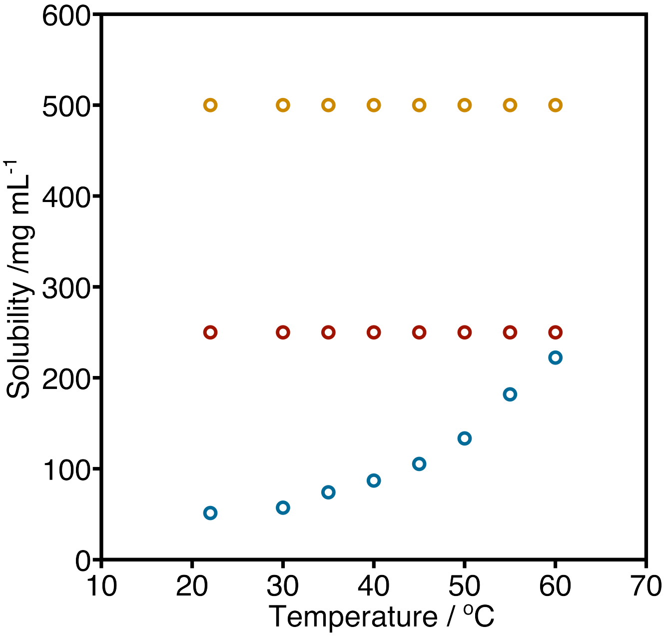

Figure 3.1: Solubility of DOPC:bSM 1:1 (blue), DOPC:bSM:Chol 1:1:1 (red) and DOPC:POPC:bSM:Chol 1:1:1:1 (orange) in hexadecane. The solubility of all lipid mixtures is larger than the concentration of lipid in oil used in this work (8.7 mg/mL). With the exception of the solubility of the binary mixture of DOPC:bSM, which increases with temperature, all other compositions do not show a pronounced variation in solubility with temperature.

3.1.2 Discussion

The solubility limit of these lipid mixtures in hexadecane is well above the concentration of lipid in oil used for experiments described in this dissertation

(8.7 mg/mL), and thus we conclude that the mass of lipids added to hexadecane accurately represents their concentration.

3.2 Sampling of ternary lipid mixtures in DIBs

Sampling of studied ternary lipid mixtures in DIBs was carried out. DIBs of ternary lipid mixtures were formed according to the protocol described in section 2.3 and imaged using the setup described in subsection 2.5.1. It is predicted that DIBs formed of lipid mixtures in hexadecane contain 9.2%v oil content [68]. Different phases were visualised by the addition of TRITC-DHPE and DiI-C_{18}; two fluorescent probes which are known to partition in the L_d phase [18]. The phase diagrams for the ternary lipid mixtures of (DPhPC, DPPC and Chol + 1 mol% of TRITC-DHPE) and (DPhPC, bSM and Chol + 1 mol% of DiI-C_{18}) as obtained by fluorescence imaging, are shown in figures 3.3 and 3.4, respectively. 16 different molar compositions of (DPhPC, DPPC and Chol) and (DPhPC, bSM and Chol) were sampled.

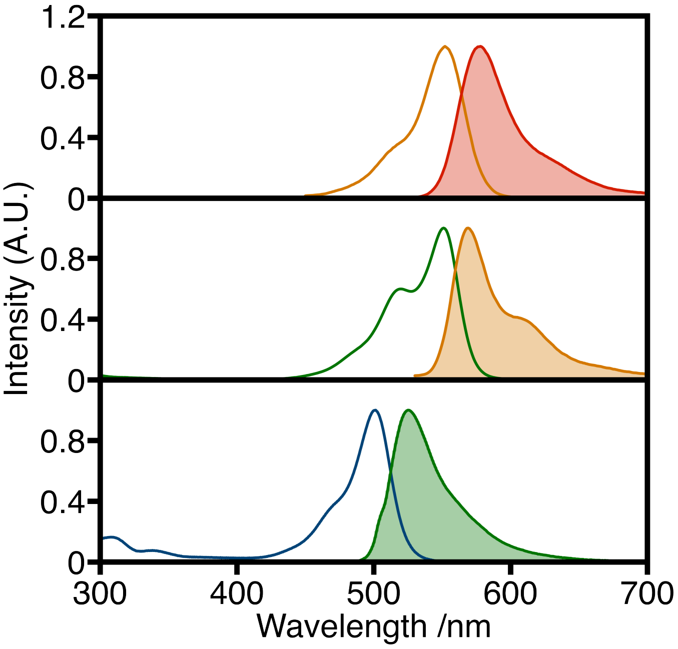

Figure 3.2: Absorption and emission spectrum of (upper panel) TRITC-DHPE, (middle panel) DiI-C18 and (lower panel) ATTO 488 DPPE.

3.2.1 Results

Continuous and bright regions were attributed to the $\mathrm{L_d}$ phase. Dark, micrometre-sized, circular regions with fluctuating boundaries that can coalesce were attributed to the $\mathrm{L_o}$ phase. Dark, micrometer sized, asymmetric regions with preserved boundaries that did not coalescence were attributed to the S_o phase.

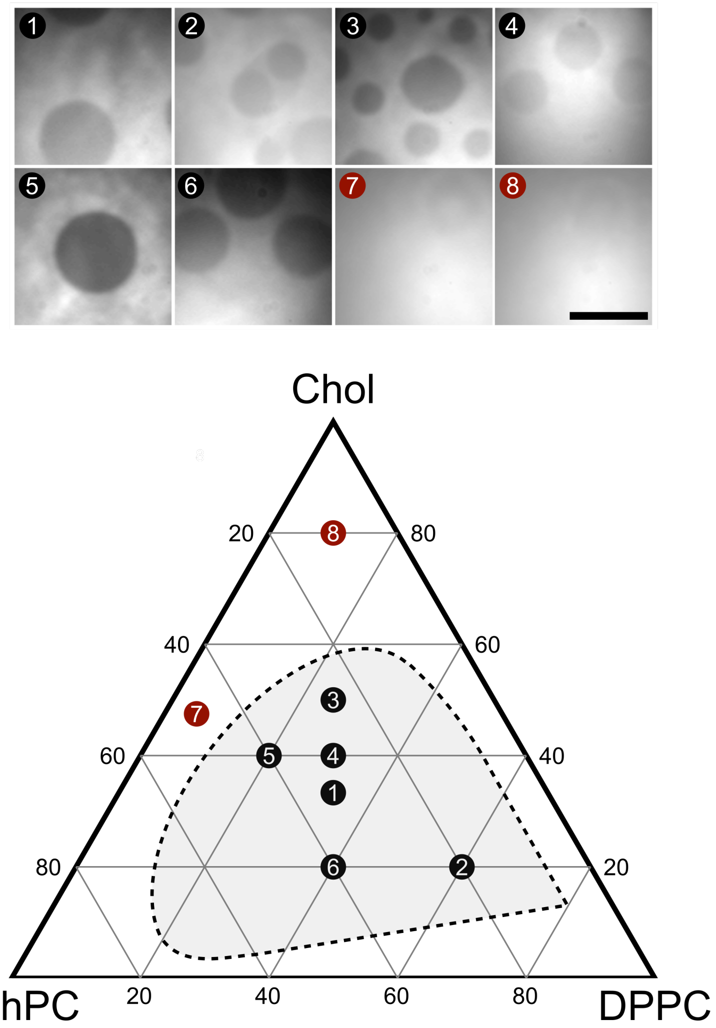

Figure 3.3: TIRF microscope images of DIBs composed of DPhPC, DPPC and Chol at different molar compositions: 1- (1:1:1), 2- (1:3:1), 3- (5:5:10), 4- (3:3:4), 5- (4:2:4), 6- (4:4:2), 7- (4.75:0.5:4.75) and 8- (1:1:8). (1), (3), (4), (5) and (6) lie in the two-phase region. (2) lies in the three-phase region. (7) and (8) lie in the single-phase region. Scale bar = 5 µm. Phase boundary is reproduced from [195].

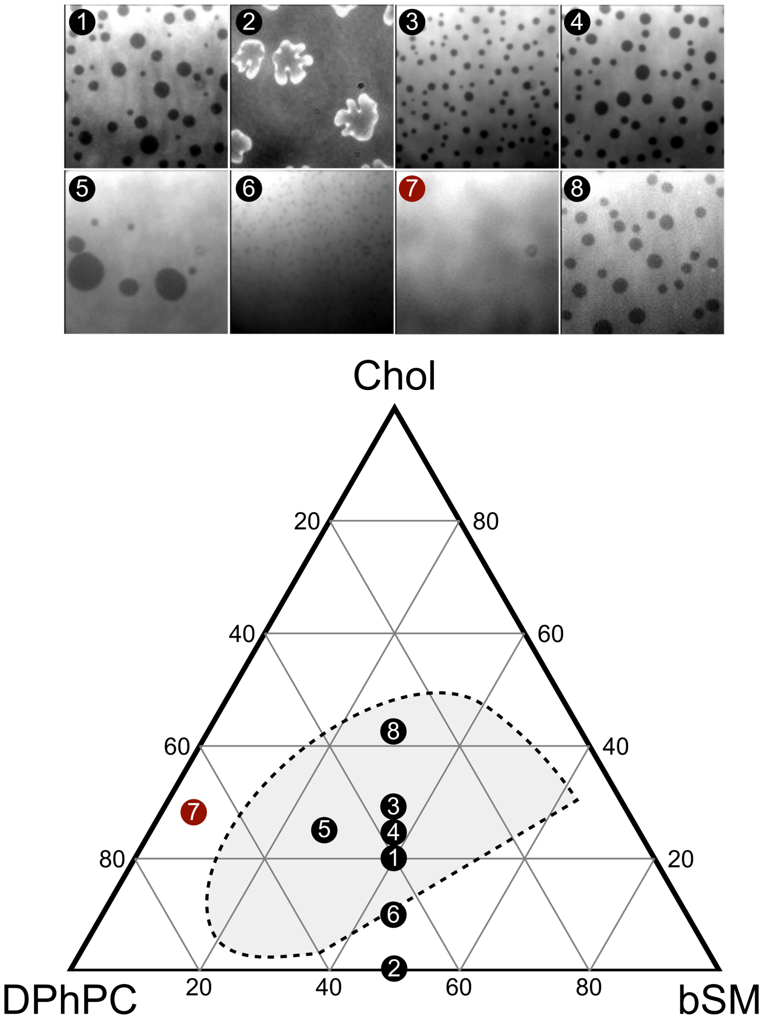

Figure 3.4: TIRF microscope images of DIBs composed of DPhPC, bSM and Chol at different molar compositions: 1- (4:4:2), 2- (5:5:0), 3- (3.33:3.33:3.33), 4- (3.75:3.75:2.5), 5- (5:2.5:2.5), 6- (4.5:4.5:1), 7- (6.25:0.65:3) and 8- (3:2.8:4.2). (1), (3), (4), (5), (6) and lie in the L_o/L_d phase coexistence region. (2) lies in the S_o/L_d phase coexistence region. (7) lies in the single-phase region. Phase boundary is reproduced from [24].

3.2.2 Discussion

The obtained phase diagrams agree with those obtained by NMR spectroscopy and confocal microscopy for multi-component GUVs [195, 24], however, the following uncommon traits were also observed:

A. Contrary to other reported findings in GUVs, mixtures containing phospholipids and cholesterol alone exhibited L_o domains with preserved boundaries which sometimes prevented their coalescence. This might be caused by the presumably high line tension imposed by the architecture of DIBs which affects the ordering of the saturated PC molecules preserving them in a highly ordered state and/or an increase in the membrane dipole potential caused by the presence of oil between the phospholipids as recently reported [146].

B. In addition, an intermediate fluorescence intensity was sometimes observed in ternary lipid mixtures exhibiting two co-existing phases. This could be attributed to either the presence of a third phase, which has been eluded to before but never observed [197, 195], or, the stimulated formation of another phase by effect of the presence of asymmetric bilayer leaflets. Recently published report argued against the latter case, providing strong evidence that bilayer asymmetry promotes the formation of binary phases by domain registration [140].

3.3 Measuring the diffusion of lipid domains in phase separated DIBs

The successful sampling of ternary lipid mixtures in DIBs has been demonstrated, however, the applicability of DIBs for studying the dynamics of lipid phase separation has never been demonstrated in the previous section. In this section, the diffusion of microscopic lipid domains examined. DIBs composed of (DPhPC, DPPC and Cholesterol + 1 mol % of TRITC-DHPE) were formed according to the protocol described in section 2.3 and imaged using the setup described in subsection 2.5.1. Obtained image sequences were analysed and diffusing microscopic domains were tracked as described in subsection 2.6.3. Obtained tracks were analyzed as described in subsection 2.6.4.

3.3.1 Results

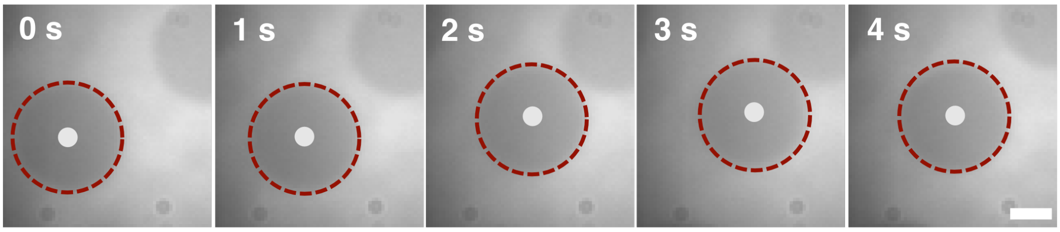

Figure 3.5: A time sequence of a diffusing microdomain in a DIB composed of DPhPC:DPPC:Chol (1:1:1) being tracked for 5 seconds. Scale bar = 1µm.

The diffusion of the tracked microdomains was fitted to four models (chapter 2): 1- Guigas-Weiss [69], 2- Evans-Sackmann [53], 3- Hughes, Philthorpe and White [87] and 4- Petrov-Schwille [134] (figure 3.6). For the Evans-Sackmann model, the second type modified bessel functions $K_0(\epsilon)$ and $K_1(\epsilon)$ in equation 1.12 were replaced with the following approximations:

$$\begin{aligned} K_0(\epsilon) &= \sqrt{\frac{\pi}{2\epsilon}}e^{-\epsilon}\Big[1-\frac{1}{8\epsilon}\Big(1-\frac{9}{16\epsilon}\Big(1-\frac{25}{24\epsilon}\Big)\Big)\Big] \\ K_1(\epsilon) &= \sqrt{\frac{\pi}{2\epsilon}}e^{-\epsilon}\Big[1+\frac{3}{8\epsilon}\Big(1-\frac{5}{16\epsilon}\Big(1-\frac{21}{24\epsilon}\Big)\Big)\Big] \end{aligned} \tag{3.1}$$

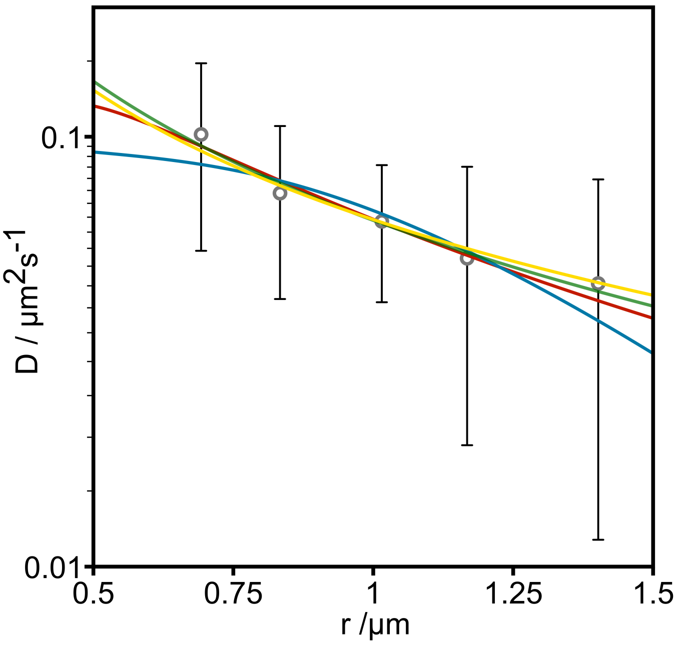

Figure 3.6: Tracking of large microdomains. Diffusion coefficients versus domain radius was fit to the large limit of the Saffman-Delbruck (yellow), Guigas-Weiss (green), Petrov-Schwille (blue) and Evans-Sackmann models (red). The Guigas-Weiss model best describes the data (GW: χ^2 = 1.329, η_c= 0.00363 Ns/m^2, c = 6.475E-6; ES: χ^2 = 1.990, η_m = 0.39288 Ns/m, b_s = 3779.6 Ns/m^3; PS: χ^2 = 6.928, η_c = 0.00357 Ns/m^2, η'' = 5.4E-9 Ns/m; SD: χ^2 = 1.705, η_c = 0.0040 Ns/m^2). Error bars report standard deviation (N = 36).

3.3.2 Discussion

Weighted by the standard deviation, the four diffusion models fit the data reasonably. The range of membrane viscosities ($\eta_m \approx$ 0.4 - 1.4 Ns/m) and solvent viscosities ($\eta_c \approx$ 0.004 Ns/m^2) obtained closely resembles those reported in the literature ($\eta_m \approx$ 0.6 Ns/m) [34] and ($\eta_c \approx$ 0.001 - 0.05 Ns/m) [133, 138]. However, comparing the reduced chi-squared values (χ^2) obtained from fitting the data to Guigas-Weiss model (χ^2 = 1.329), Petrov-Schwille approximation (χ^2 = 6.928), Evans-Sackmann model (χ^2 = 1.990) and Saffman-Delbruck model (χ^2 = 1.705), the Guigas-Weiss model was deemed to provide the best representation of the experimental data. The similarity between the membrane viscosity values previously reported and those we measured suggests that the presence of an underlying hydrogel film does not have any major effects on the diffusion of inclusions in DIBs. This was previously shown by Thompson and coworkers where the diffusion of labelled phospholipids was compared to the diffusion of lipids in SLBs and was found to be an order of magnitude higher; resembling diffusion coefficients obtained in GUVs [183].

3.4 On-demand control of lipid composition in individual bilayers

Biological membranes are thought to be capable of modulating their lipid composition *in situ* [35]. That capability might provide biological membranes with a means of modulating a range of processes including the formation and destruction of lipid phases. Replicating this process in a reduced environment would permit studying its effects on protein function. To pursue that goal, the cyclic oligosaccharide family of cyclodextrins has been widely used to modulate the lipid composition of GUVs by extracting specific components. For example, methyl-β-cyclodextrin (mβCD) is routinely employed for cholesterol extraction [205, 107, 93]. However, its mechanism of action is still poorly understood; in particular, it is unknown whether mβCD) extracts only cholesterol, or other lipids, and whether the extraction process affects both leaflets of the bilayer or only the outer leaflet. Thus far, methods employed to induce changes in the lipid composition of individual bilayers fail to yield systematic results. The architecture of DIBs suggests a simple way to control the lipid composition of an individual bilayers. In DIBs, lipids in the oil phase are expected to be in equilibrium with those in the bilayer, with continuous exchange of lipids that occur at the interface (figure 3.7). We speculated that the titration of appropriate amounts of lipids in the oil phase should result in a compositional change in the bilayer.

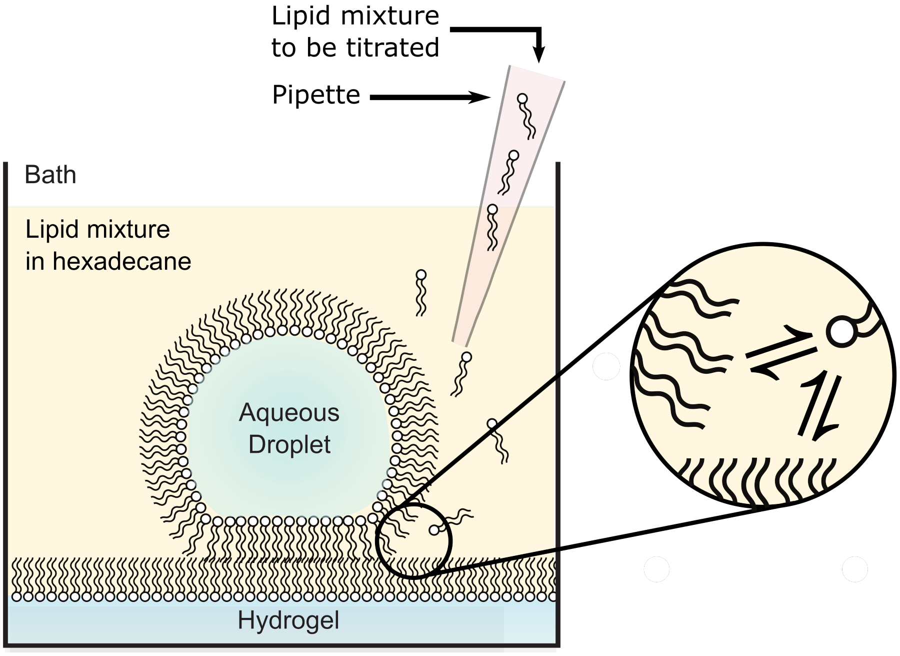

Figure 3.7: Schematic diagram showing the principle underlying the *in situ* modulation of lipid composition in individual bilayers. Since lipids in the oil phase are in equilibrium with those in the bilayer, on-demand control of the bilayer's lipid composition is possible by titrating set amounts of known lipids into the oil phase.

3.4.1 Results

DIBs composed of either

A. 1:1 of DPhPC and bSM (+1 mol% of DiI-C_{18}), or

B. 1:1:1.6 of DPhPC, bSM and Chol (+ 1 mol% of DiI-C_{18}),

were formed according to the protocol described in section 2.3. DIBs were visualized using the setup described in subsection 2.5.1. Two titration sequences were tested: reversible and irreversible titrations. Three stepwise titrations of cholesterol (irreversible) into a single DIB were performed from the initial composition "1" and three consecutive titrations of DPhPC and bSM (reversible) from the initial composition "2". These titrations were designed to cross the phase boundary and so provide visual confirmation of a compositional change in the bilayer. The titre was calculated so that the final concentration of the lipids in the oil phase was kept constant at 8.7 mg/mL. Furthermore, the volume of oil used in each titration was calculated so that the total titrated volume was less than the volume of the individual wells. Care was taken to ensure that the droplets were immersed in the oil solution. The droplets were heated for 20 minutes in a preheated oven set at 46°C to ensure optimal mixing of the bilayer components and faster equilibration between lipids in the monolayers and those in the oil phase. The results for the irreversible and reversible titrations are shown in figures 3.8 and 3.9 respectively.

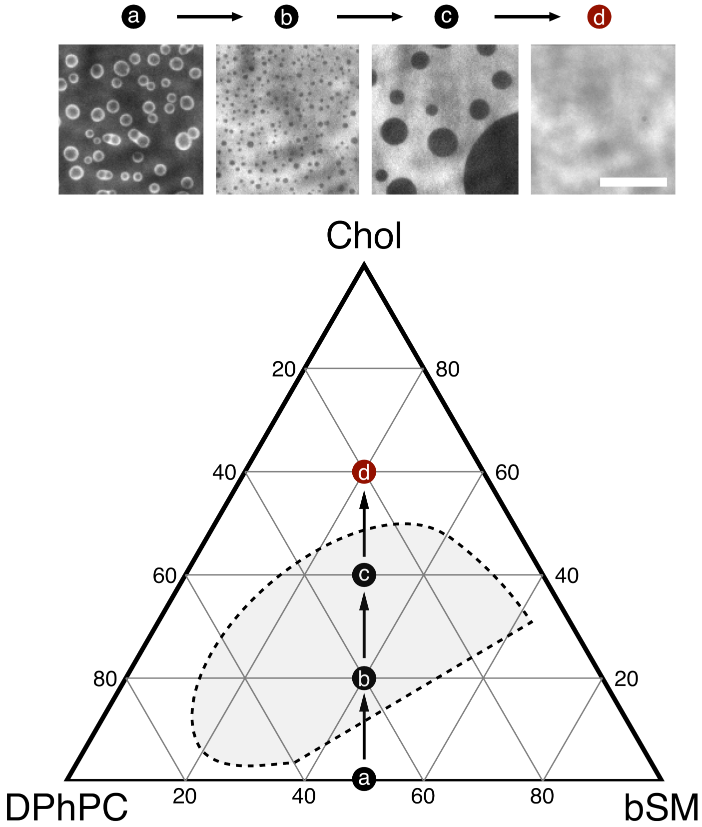

Figure 3.8: Consecutive titrations of cholesterol in a bilayer composed of a binary mixture of DPhPC and bSM from an initial composition (a) - (1:1 - DPhPC:bSM) to a final composition (d) - (1:1:8 - DPhPC:bSM:Chol). (a) lies in a region of $S_o/\mathrm{L_d}$ phase coexistence. (b) and (c) lie in a region of $\mathrm{L_o}/\mathrm{L_d}$ phase coexistence and (d) lies in a single $\mathrm{L_d}$ phase region. Scale bar = 17 µm. Phase boundary is reproduced from [24].

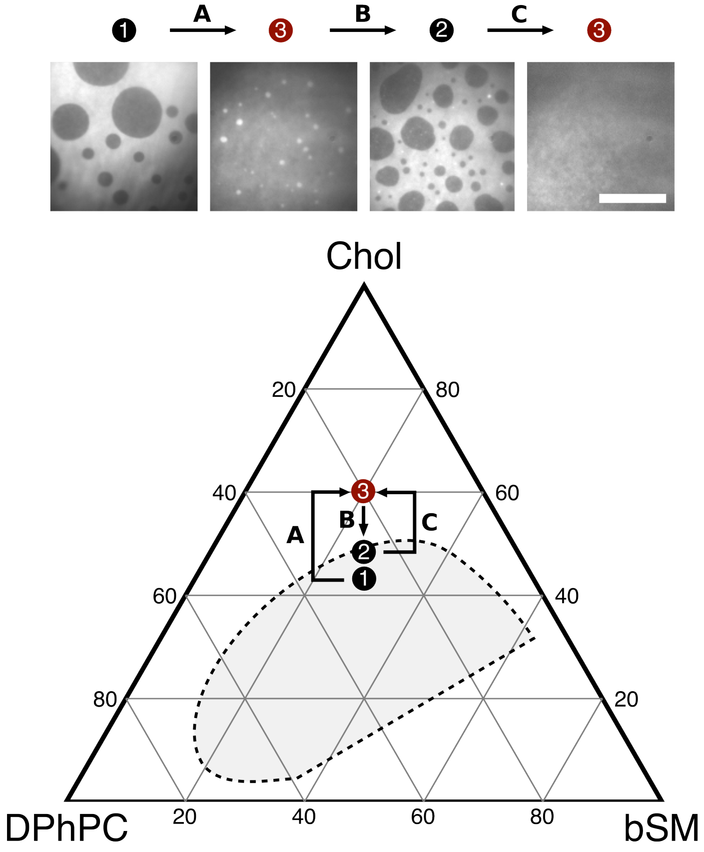

Figure 3.9: Consecutive titrations in lipids and cholesterol to a bilayer composed of a ternary mixture of DPhPC, bSM and Chol from an initial composition (1) - (1:1:1.6 - DPhPC:bSM:Chol) to a final composition (3) - (1:1:3 - DPhPC:bSM:Chol). (1) and (2) lie in a region of L_o/L_d phase coexistence and (3) lies in a single L_d phase region. Scale bar = 17 µm. Phase boundary is reproduced from [24].

3.4.2 Discussion

Cholesterol was irreversibly titrated in a composition containing 0% cholesterol until 60% cholesterol was reached following three consecutive titrations. The overall change in the fluorescence intensity of a bilayer not only marks the formation and destruction of multiple phases, but also, the successful modulation of a bilayer's content. The successive growth of domains between (a) and (c) in figure 3.8 is roughly proportional to the amount of cholesterol embedded in the bilayer and is consistent with predictions. Likewise, the reversible titration of lipids and cholesterol, depicted in figure 3.9, shows the reversible destruction and reformation of co-existing liquid phases that is also consistent with predictions.

According to my knowledge, this is the first systematic modulation of the lipid composition of an individual bilayer. The protocol followed in this dissertation includes heating of the droplets following each titration, this step can be eliminated at the expense of longer modulation times.

After developing these methods, we applied them to two biologically-relevant problems where lipid phase separation is important.

3.5 Lipid phase dependent pore formation of Equinatoxin II

Pore-forming proteins play a dominant role in cell apoptosis [81, 132, 88, 20, 149, 174]. Their strategy involves binding to the cell membrane [22], assembling [182] and inserting into the host membrane to eventually cause cell lysis [161]. The binding of some pore forming proteins is catalysed by the presence of specific bilayer components [14, 61] and/or the presence of coexisting phases [160]. The lack of a single artificial membrane technique which permits the imaging of lipid phase separation and pore formation simultaneously has hindered progress in elucidating the functional role of lipid phase separation in promoting protein binding and pore formation.

EqtII is a member of actinoporin protein family [59, 37, 5], isolated from the sea anemone *Actinia equina*. EqtII is believed to play a role in paralyzing prey and defending against predators [59]. EqtII is a 20 kDa protein with high affinity for sphingomyelin-containing lipid membranes [14]. Cy3-labeled pore forming protein Equintatoxin II (EqII) was examined in phase-separated DIBs. EqII was previously reported to preferentially bind to the boundaries of L_o/L_d phases [160], however, the lipid phase dependant pore formation of EqII has not been delivered. DIBs composed of DPhPC, eSM and Chol (+ 1 mol % DiI-C18) were formed according to the protocol described in section 2.3. The formed DIBs were visualised using the imaging setup described in subsection 2.5.1. Following DIB formation, EqII monomers were injected into the aqueous phase of a phase-separated DIB system using a piezo-driven glass micropipette.

3.5.1 Results

EqII monomers were found to preferentially bind to the boundaries of L_o/L_d phases, as previously reported, and then diffuse into the L_d phase (figure 3.10).

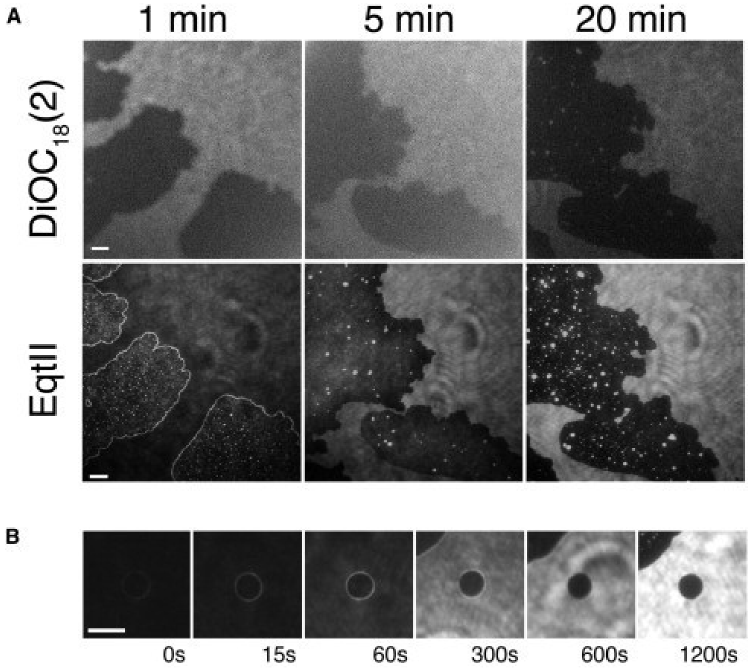

Figure 3.10: (A) Binding of cy3-labelled EqII monomers at domain boundaries. (B) Diffusion of the monomers into the disordered phase. DiO-C_{18} is a marker of the disordered phase. Scale bars = 10 µm.

To study the phase-dependant pore forming mechanism of EqII, calcium flux imaging was performed. $CaCl_2$ was added to the rehydration agarose and the calcium sensitive dye Fluo-8H was added to the buffer solution. Micro electrodes were inserted into the aqueous droplets and the rehydration agarose. A potential difference was applied between the electrodes to drive the calcium ions through the EqII pores. A localised fluorescence signal is produced near the pore as calcium ions bind Fluo-8H. Dual colour imaging of Cy3b and Fluo-8H showed pore formation in the L_d phase (figure 3.11).

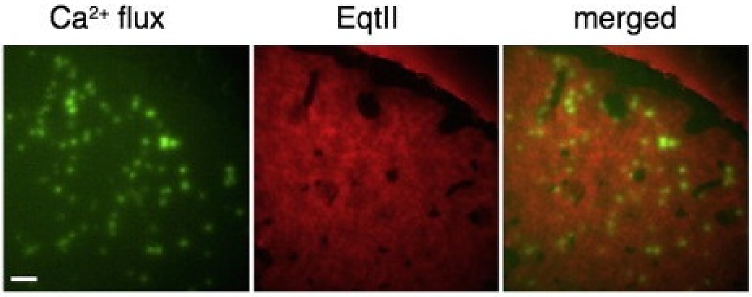

Figure 3.11: Dual color calcium flux and single molecule imaging of EqII pores and monomers revealing the phase-dependance of EqII pore formation.

3.5.2 Discussion

These results suggest two models for the mechanism of action of EqII:

A. Binding at the boundary of L_o/L_d, insertion, diffusion into the L_d phase then and pore formation; or

B. Binding and accumulating at domain boundaries leading to saturation of binding sites, followed by binding L_d, insertion and pore formation.

Although this experiment is the first to combine simultaneous membrane imaging and calcium flux imaging, it could not differentiate between both models. By combining calcium flux imaging with single-molecule Forster Resonance Energy Transfer (smFRET) it could be possible to elucidate the insertion dynamics of pore forming toxins in relation to lipid phase separation.

Contribution

Experimental work done in collaboration with J. Rojko. Danial prepared phase-separated DIBs and Rojko injected EqII.

3.6 Electroporation of phase separated DIBs

Electroporation, the transient permeabilization of biological membranes by the application of an electric field, is a commonly used non-invasive method for the delivery of biomolecules into cells [175, 49]. Electroporation is employed for gene transfection [2]. Electropores are electric field induced pores in lipid membranes that are thought to be toroidal in shape [185, 181], however, there is not experimental observation to support this claim. Recent molecular dynamics simulations of multi-component phase-separated lipid bilayers predicted that electropores preferentially form in the L_d phase [145], however, there is no experimental evidence to confirm these predictions.

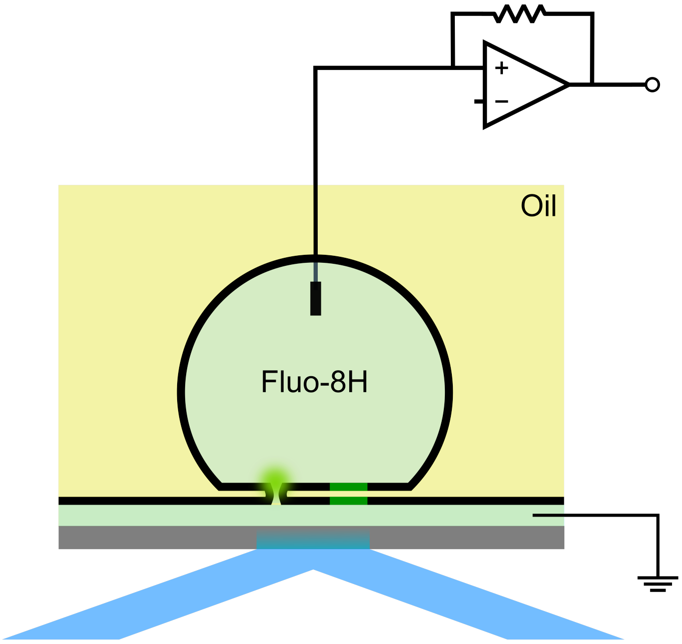

Figure 3.12: Schematic for Imaging setup used to study electroporation in phase-separated DIBs.

3.6.1 Results

DIBs composed of DPhPC,bSM and Chol (1:1:1 + 1 mol% DiI-C_{18}) and DPhPC, DPPG and Chol (+ 1 mol% DiI-C_{18}) were formed according to the protocol described in section 2.3. The formed DIBs were visualised using the imaging setup described in subsection 2.5.1. Calcium flux imaging was performed to observe electropores. $CaCl_2$ was added to the rehydration agarose and the calcium-sensitive dye Fluo-8H was added to the buffer solution. Micro electrodes were inserted into the aqueous droplets and the rehydration agarose. A potential difference (95 - 160 mV) was applied between the electrodes to drive the calcium ions through the electropores.

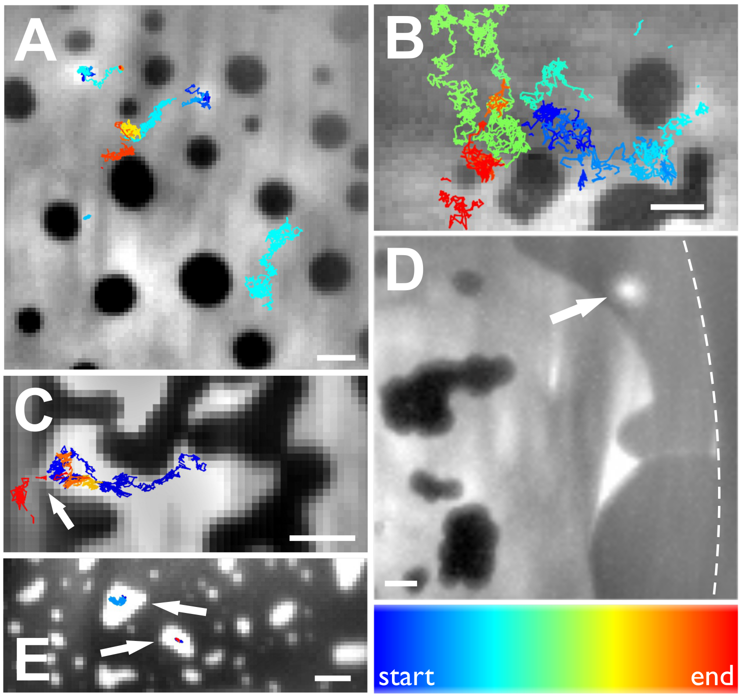

Figure 3.13: Electroporation in phase-separated DIBs. Images are median z-stacks; recordings were made between 95 and 160 mV. The colour of a trajectory indicates the time at which it began in the recording; see coloured bar beneath images. (C-E) DPhPC:DPPG:cholesterol, 1:1:1. Arrow in (E) indicates a gap between two solid ordered phases through which an electropore passes. (F) DPhPC:sphingomyelin:cholesterol, 1:1:1. Electropores form and are trapped within small pools of the L_d phase, marked by arrows. Scale bars are 5 µm.

3.6.2 Discussion

Application of an electrical potential across the membrane resulted in resolvable voltage-sustained fluorescence bursts indicative of the presence of electropores. The electropores were furthermore diffusive, thus, affirming claims related to the fluidity of the bilayer (figure 3.13A, B, C and E). Electropores formed and diffused inside the L_d phase and were not found in the L_o phase. This is the first time that the diffusion of electropores has been observed.

Contribution

Experimental work done in collaboration with J. Sengel

3.7 Summary

In this chapter, I have described work towards imaging and characterizing multi-component phase-separated DIBs. Although the architecture of DIBs makes it appealing to study various membrane processes simultaneously, it is the fluid-like property which makes it most distinctive from other substrate-supported systems. In chapter 4, I describe work towards imaging the dynamics of transient nanoscopic lipid domains in phase-separated DIBs.

4

Dynamic label-free imaging of lipid nanodomains

Phase separated DIBs have been constructed using the protocol detailed in chapter 3 and examined using iSCAT microscopy. In this chapter, the following related experiments are described:

A. Label-free imaging of phase-separated DIBs,

B. Label-free imaging of induced L_o nanodomains in DIBs composed of ternary lipid mixtures,

C. Label-free imaging and characterization of induced S_o nanodomains in DIBs composed of ternary lipid mixtures, and

D. Label-free imaging and characterization of transient L_o nanodomains in DIBs composed of quaternary lipid mixtures.

Contribution

Experimental work done in collaboration with G. de Wit. Danial conceived the idea, Danial prepared the DIBs, Danial and de Wit performed the imaging, Danial and de Wit analysed the S_o data, Danial analysed the L_o data and Danial prepared the figures.

4.1 Introduction

The construction and observation of multi-component phase-separated artificial membrane systems has served to explain lipid phase separation from a physical perspective [17, 196, 197, 195, 198]. Failure to observe transient nanoscopic lipid rafts *vivo* has led to increased uncertainty in the interpretation of biochemical experiments performed on biological membranes. Advances in fluorescence microscopy and labelling chemistry have recently permitted the tracking of fluorescently labelled sphingomyelin molecules in the membrane of HeLa cells [48]. Under physiological conditions, the transient entrapment of individual Sphingomyelin molecules in cholesterol-mediated nanoscopic complexes was detected using STED-FCS. These results were interpreted in favour of the existence of transient nanoscopic lipid rafts, however, the transient binding of Sphingomyelin to cholesterol-mediated supramolocular complexes was not excluded. More recently, improved fluorescently labelled lipid analogues with longer tail structures were developed [82, 169], incorporated and tracked using STED-FCS in biological membranes [83]. This study concluded that biological membranes are spatially homogenous and that spatial heterogeneities previously observed are attributed to the steric pressure between the large fluorescent probes. These results could be thought to have abolished any presumed evidence pointing towards the compositional heterogeneity of cellular membranes, and in particular, the existence of lipid rafts, however, the relatively low spatial and temporal resolution reported (60 - 80 nm) does not the exclude possibility of the existence of yet smaller, more dynamic, lipid rafts in biological membranes.

The orchestrated distribution of proteins in biological membranes remains a dilemma. Some recent reports propose that the mismatch between the length of the transmembrane domain of different membrane proteins is adequate to sort, even structurally homologous, proteins into distinct domains [120]. Others have shown that the anchoring of the cytoskeleton to biological membranes is responsible for the formation of multi-protein assemblies underlying its gross organization [151, 84] and induces temperature-resistant lipid phase separation in multi-component artificial membrane systems. Very recently, transmembrane coupling of some membrane proteins was discovered to drive their clustering at the nanoscale [142]. Hydrophobic mismatch, cytoskeleton binding and transmembrane coupling might all contribute to the segregation of membrane proteins, yet, the question remains, whether the formation and destruction of lipid rafts plays an organisational role. The observation of transient nanoscopic lipid rafts using fluorescence microscopy is not possible due to the inefficient partitioning of currently available lipid probes [82] and the anticipated effects these might have on lipid segregation at the nanoscale [52, 198]. Label-free microscopy techniques, such as Atomic Force Microscopy (AFM), were previously employed to observe nanoscopic lipid domains in SLBs [36]. However, the slow acquisition rates and the reduced fluidity in SLBs have not allowed the observation of transient nanoscopic lipid domains at relevant timescales. Reflection Interference Contrast Microscopy (RICM) was successfully used to image micron-sized domains in phase separated substrate-supported lipid monolayers [92] but this work was not carried further. RICM was also used to image phase separated lipid bilayers [54, 141]. The height and refractive index mismatch between different coexisting phases in multi-component phase-separated DIBs can, in principle, provide a detectable scattering signal in ISCAT microscopy [8, 7, 131, 102, 130, 137].

4.2 Label free imaging of phase separated DIBs

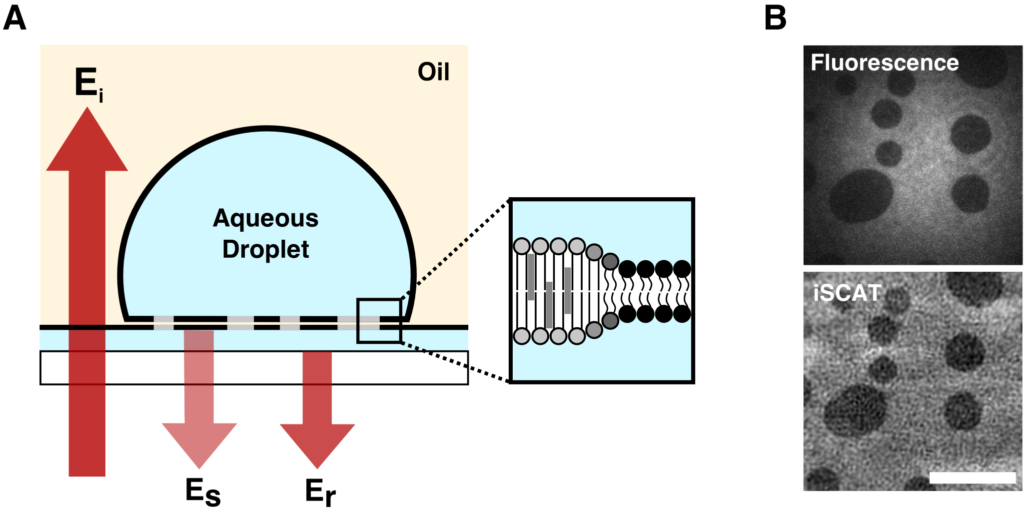

Figure 4.1: Label-free imaging of phase-separated DIBs using iSCAT. (A) Schematic of a DIB showing ordered (light grey) and disordered (black) phases. The interference between the scattered and reflected fields (E_s and E_r) is detected in the far-field using a CMOS camera. (B) 100 ms TIRF (top) and iSCAT (bottom) images of a DIB containing L_o domains within a bulk L_d phase. (1:1 DOPC:bSM + 1 mol % Atto 488 - DPPE). The static background due to scattering from the agarose substrate can been seen in this raw iSCAT image. This background is subtracted in subsequent images. Scale bars 5 µm.

DIBs composed of a 1:1 mixture of DPhPC and bSM (+ 1 mol % ATTO 488 - DPPE) were formed according to the protocol described in section 2.3. The formed DIBs were visualised using the imaging setup described in subsection 2.5.2. Freely diffusing S_o micron-sized domains were simultaneously observed using scattering and fluorescence (figure 4.1B). Images were processed as described in subsection 2.6.1. Figure 4.2 shows the difference between raw and processed images. S_o domains of the aforementioned mixture had a pixel Weber contrast of 4%[1]. The detection limit in iSCAT is 0.6% (set by shot noise) the observation of nanoscopic lipid domains was sought.

---

[1] Weber contrast is defined as the ratio of the time-dependent intensity (the signal) to the time-independent intensity (the background)

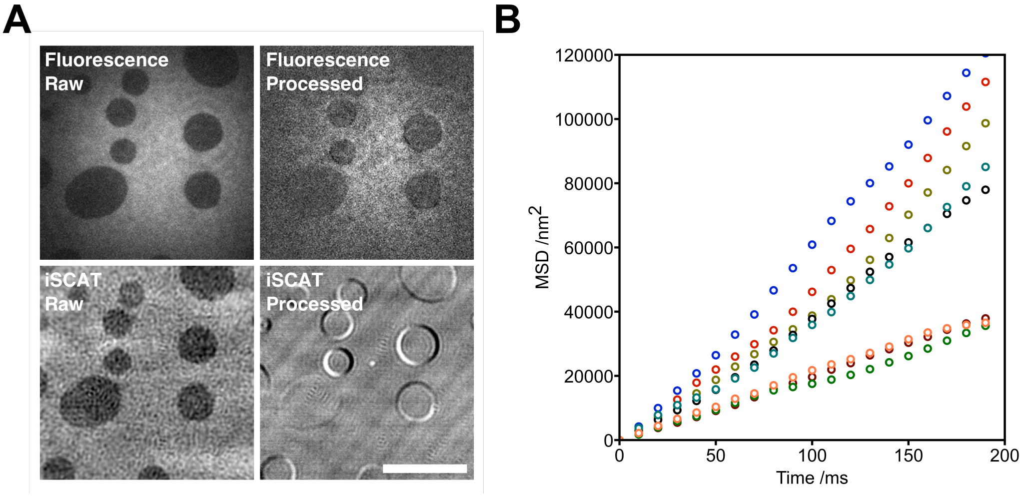

Figure 4.2: (A) Comparison of raw and processed TIRF and iSCAT images. Images of domains in a 1:1 DOPC:bSM bilayer with 1 mol% ATTO 488 - DPPE. Images were taken at 100 Hz (iSCAT) and 20 Hz (fluorescence). Scale bar 10 µm. (B) MSD versus time for micro domains showing Brownian diffusion.

4.3 Label free imaging of induced L_o nanodomains in ternary lipid mixtures

DIBs composed of a 1:1:1 mixture of DPhPC, bSM and Chol were formed according to the protocol described in section 2.3. DIBs were visualized using the imaging setup described in subsection 2.5.2. The microscope objective of the imaging setup described in subsection 2.5.2 was fitted with an objective heater controlled using a variable current output controller. Furthermore, precautions were taken to insulate the device from the metal stage to ensure minimal heat dissipation. The temperature of the objective was monitored in real time using a thermocouple. The temperature of the objective was ramped from room temperature (≈ 23°C) to (≈ 45°C) above the transition temperature of the ternary lipid mixture (≈ 35°C) until lipid mixing was complete and a single phase was observed throughout the whole bilayer. The device was then allowed to cool and nanoscopic lipid domains were seen to emerge as the bilayer's temperature passed below the transition temperature of the ternary lipid mixture.

The emerging lipid nanodomains were tracked and the contrast was measured with time (figure 4.3).

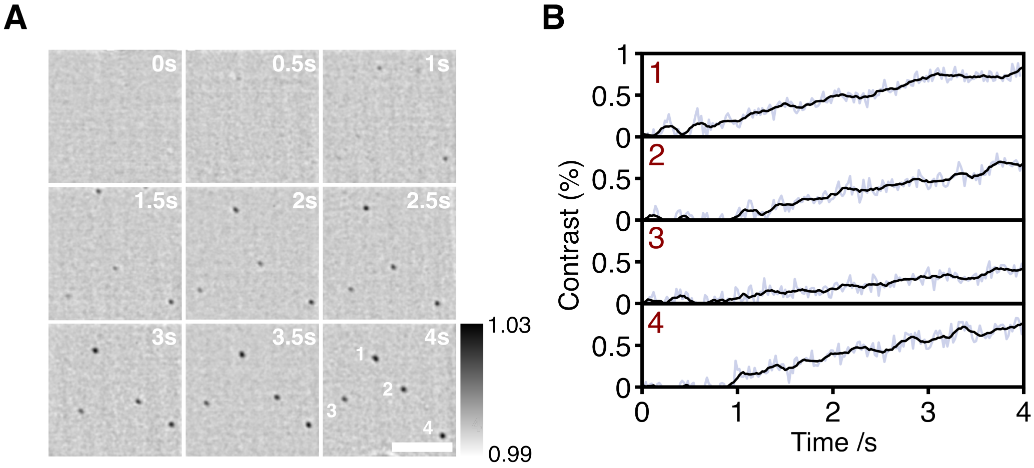

Figure 4.3: (A) Time-lapse sequence of iSCAT images of L_o nanodomains appearing from a uniform L_d phase upon cooling of a droplet below the phase transition temperature. The droplet was heated to 45°C for 10 minutes. Nanodomains appeared 2 - 5 minutes after heating was removed. (D) Trajectories corresponding to average pixel contrast within a 900 × 900 nm window centered on each nanodomain labelled in (B). Values before the appearance of the domain are representative of the background fluctuations at the position where the domain first becomes visible. Scale bars 5 µm.

The size of induced L_o nanodomains is below the diffraction limit but can be deduced from their respective diffusion coefficients. However, the diffusion of L_o domains is subject to hydrodynamic perturbations and is expected to be inconsistent with the mathematical models describing the diffusion of cylindrical inclusions in two-dimensional membranes (section 1.4). The diffusion of S_o nanodomains has been modelled (section 1.4). In the next section, S_o nanodomains are imaged and tracked. A relationship is obtained between the size, contrast and diffusion of S_o nanodomains.

4.4 Label free imaging of induced S_o nanodomains in ternary lipid mixtures

DIBs composed of a 1:1 mixture of DPhPC and bSM were formed according to the protocol described in section 2.3. DIBs were visualized using the imaging setup described in subsection 2.5.2. To effectively reduce mechanical drifts of the sample, stage or immersion oil whilst imaging, objective heating was replaced with laser heating. The intensity of the excitation laser was increased 30 fold to induce local heating of a 1 µm^2 area of the sample. The time taken for a micron-sized domain to become a diffraction-limited-sized domain is $\approx$ 10 minutes and the time taken for a diffraction-limited-sized domain to completely disappear is $\approx$ 1 minute.

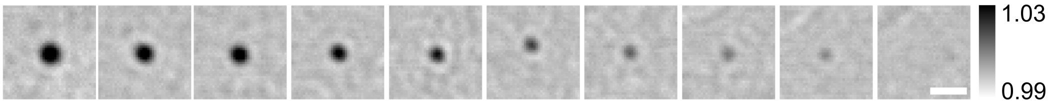

Figure 4.4: 15 s, time-lapse sequence of iSCAT images showing shrinking S_o nanodomains in a DIB (1:1 DPhPC:bSM, plus 1 mol% Atto488-DPPE. Scale bar 0.5 µm.

A large number of S_o nanodomains were imaged and tracked to obtain the relationship between the radius and peak contrast. Nanodomains were tracked and were subsequently fitted with gaussian profiles as described in subsection 2.6.1. The Half Width Half Maximum (HWHM) and peak contrast value of each imaged gaussian-fitted nanodomain was computed and plotted as shown below.

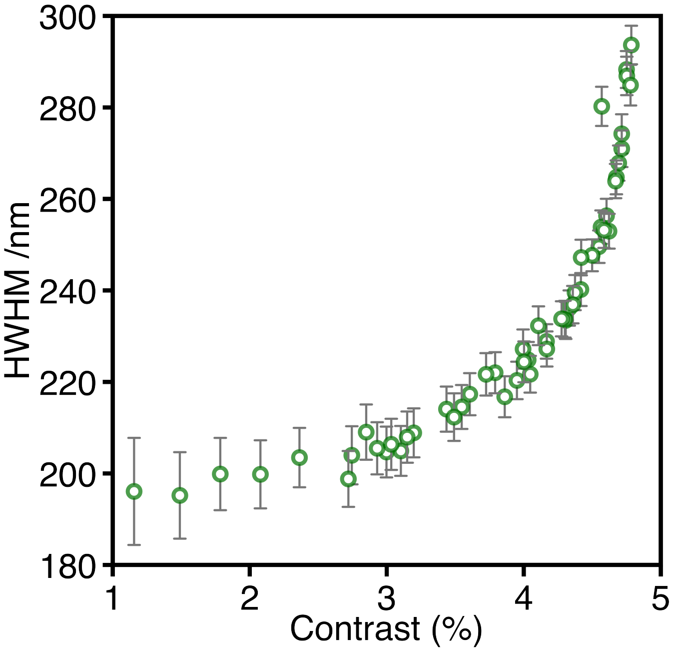

Figure 4.5: HWHM versus contrast for S_o nanodomains. HWHM tends to the resolution limit of our microscope as the contrast decreases. Our limiting detectable contrast is 0.5% at 0.5 kHz. Error bars show the average error in the HWHM, based on the covariance of the Gaussian fitting parameters.

Figure 4.5 shows the dependance of the HWHM on the peak contrast value. Below a contrast value of 3% all the domains are smaller than the diffraction limit of light; this is evident from the limiting HWHM at low contrast. The diffusion coefficients of small micron-sized S_o domains were computed and plotted against their corresponding measured radii values (figure 4.6). The scatter plot was fitted to four models for two-dimensional vales (section 1.4). The diffusion of micron-sized domains was reasonably described by all four diffusion models. However, it is evident that, below the diffraction limit, different models do substainally diverge. To discriminate between the different models, the radii of domains just smaller than the diffraction limit (but with contrast greater than 2%) were determined by deconvolution of this PSF (338.6 nm). Fitting the combined data from domains smaller and larger than the diffraction limit, the Guigas-Weiss (χ^2 = 2.957) model was found to best describe the data (figure 4.6).

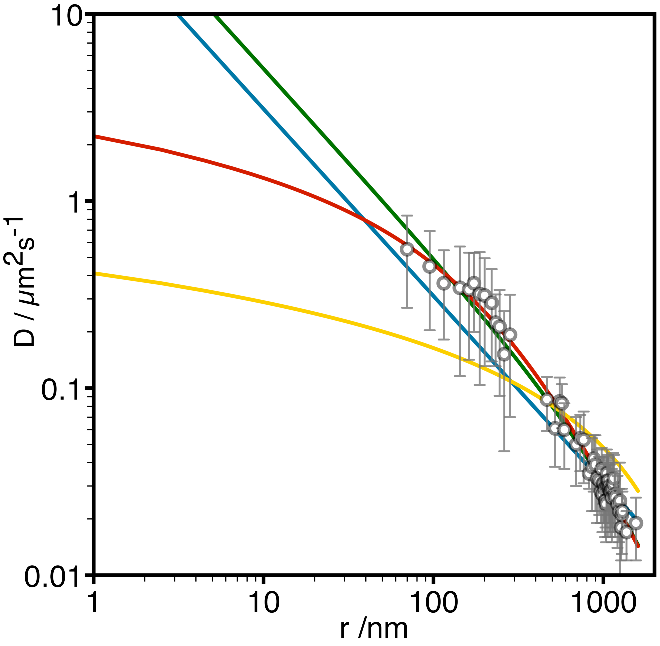

Figure 4.6: Tracking of small S$_o$ microdomains. Data was recorded at 500 Hz, using 662 nm illumination at a power density of 0.7 kW/cm^2. The radii of domains smaller than the diffraction limit (338.6 nm) was obtained by deconvolution of the PSF. Diffusion coefficients versus domain radius was fit to the large limit of the Saffman-Delbruck (yellow), Guigas-Weiss (green), Petrov-Schwille (blue) and Evans-Sackmann models (red). The Guigas-Weiss model best describes the data (GW: χ^2 = 2.957, η_c= 0.00505 Ns/m^2, c = 1.377 x 10-6; ES: χ^2 = 3.002, η_m = 0.20596 Ns/m, b_s = 13561.8 Ns/m^3; PS: χ^2 = 6.110, η_c = 0.0083 Ns/m^2, η_m = 2.5 x 10-12 Ns/m; SD: χ^2 = 9.02, η_c = 0.00306 Ns/m^2, η_m = 1.51 Ns/m). This scaling enables the estimation of So and Lo nanodomain radii.

By extrapolating the Guigas-Weiss fit, the size of domains below the diffraction limit can be deduced (figure 4.7). Comparing the diffusion coefficients with those we measure for the smallest detectable domain predicts a radius of $\approx$ 50 nm.

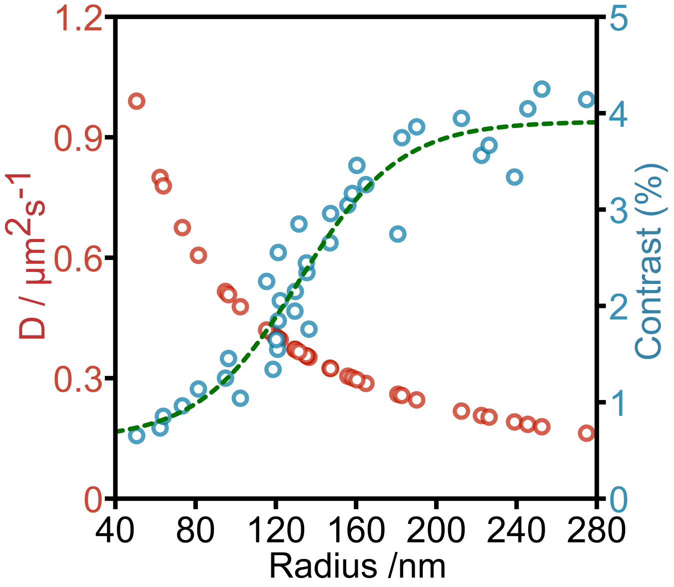

Figure 4.7: Diffusion coefficient (red) versus radius calculated by calibration to microdomain diffusion for the same bilayer composition. Contrast (blue) versus radius calculated from the measured diffusion coefficient. Contrast increases with increasing radius and can be approximated by a sigmoid (dashed line) until we approach the resolution limit.

Following our determination of the scaling of domain diffusion with radius, the scaling of radius with contrast was examined. A sigmoid function was chosen to fit the data (Appendix C.1). The function is mathematically expressed as:

$$c(r) = c_0 + \frac{c_{max}}{1 + e^{\frac{r_0 - r}{m}}} \tag{4.1}$$

Where $c_0 = 0.61081$ is the detection limit, $c_{max} = 3.3037$ is the contrast at the diffraction limit, $r_0 = 131.72$ is the inflection point and $m = 25.146$ is the rate of increase of the sigmoid function. c_0 is dictated by the smallest observable contrast, which in turn is dictated by shot noise, while c_{max} is dictated by the refractive indices of the different phases and their surroundings and the PSF of the microscope. The sigmoid function, describing the dependance of the contrast on the radii of S_o nanodomains, can also be used to deduce the radius of any nanoscopic domain, whether S_o or L_o, provided that the peak contrast value at or above the diffraction limit is known.

4.5 Label free imaging of transient L_o nanodomains in quaternary lipid mixtures

Although S_o/L_d phase coexistence has enabled a determination of the scaling between the contrast and radii of nanodomains, it has limited biological relevance. L_o/L_d phase coexistence is implicated in the formation and destruction of nanoscopic functional lipid rafts. In 2013, Heberle and coworkers used FRET, SANS and Monte Carlo Simulations to detect of L_o nanoscopic lipid domains [76] in sub 100 nm liposomes. Using a quaternary mixture of DSPC, DOPC, POPC and Chol they showed that modulating $\rho \equiv [\text{DOPC}]/([\text{DOPC}]+[\text{DSPC}])$ can modulate the size of L_o nanoscopic lipid domains present in the system. Their measurements indicate an increase in the average diameter of a domain from ≈ 13 nm to 32 nm when the molar ratio ρ was changed from 0 to 0.3. The mismatch in the thickness of a bilayer, brought by the presence of saturated and saturated lipids, is capable of modulating the size of nanoscopic lipid domains. Here, quaternary lipid mixtures were exploited. Although Heberle and coworkers used DSPC, DOPC, POPC and Chol, DSPC is a long chain lipid that is immiscible in hexadecane and therefore hard to incorporate in DIBs. To resolve that problem, the quaternary mixture DSPC, DOPC, POPC and Chol was replaced with DOPC, POPC, bSM and Chol. The latter composition is compatible with the architecture of DIBs. Whilst the ratio of (DOPC+POPC) to bSM and Chol was kept constant, ρ was varied. DIBs composed of a ρ:(1 - ρ):1:1 mixture of DOPC, POPC, bSM and Chol were formed according to the protocol described in section 2.3. DIBs were imaged using the setup described in subsection 2.5.1.

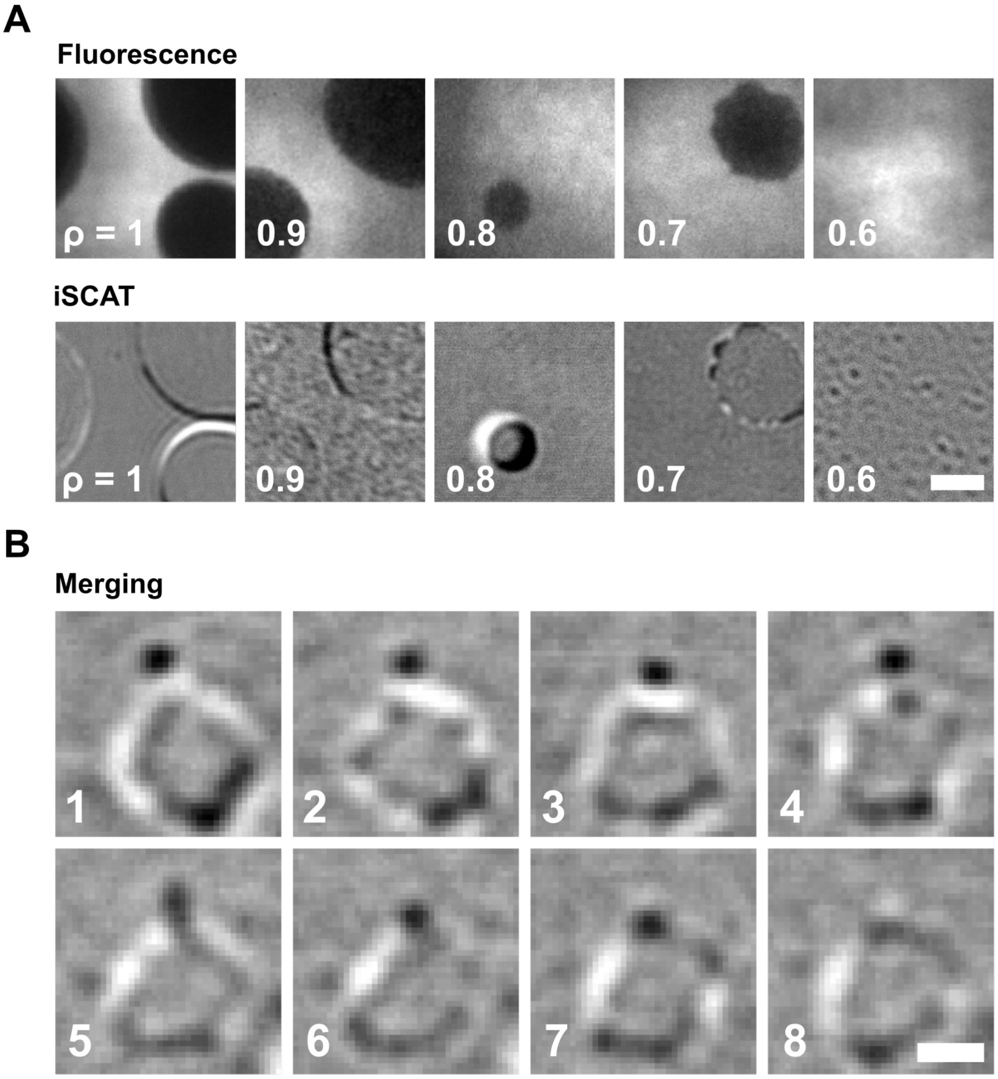

Figure 4.8: (A) TIRF and iSCAT images for quaternary mixtures of DOPC, POPC, bSM and Chol ρ:(1 - ρ):1:1 (+ 1 mol % DiI-C18), with the fraction, ρ, varying from 1 to 0.6. iSCAT images were binned to 100 Hz. TIRF images were binned to 10 Hz. Scale bar 2.5 µm. (B). Image sequences of nanodomain / microdomain merging. Scale bar 1 µm.

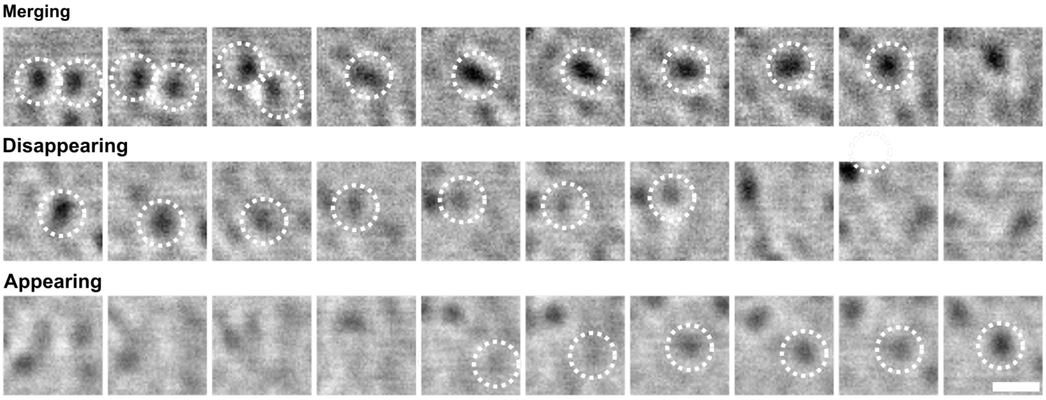

Figure 4.9: Observing transient nanodomains. Image sequence of nanodomains merging, disappearing, and appearing for $\rho = 0.6$. Scale bar 1.5 µm.

As the molar ratio ρ is decreased from 1 to 0.7, domain boundaries' fluctuations become pronounced (figure 4.8a). At $\rho = 0.6$, no phase coexistence was observed in TIRF, but, highly dynamic diffraction-limited spots, that are spontaneously formed and destructed within a short time scale, were observed in iSCAT (figure 4.8b and 4.10). These diffraction-limited spots were not observable for any other lipid composition and are therefore, indeed, transient nanoscopic lipid domains.

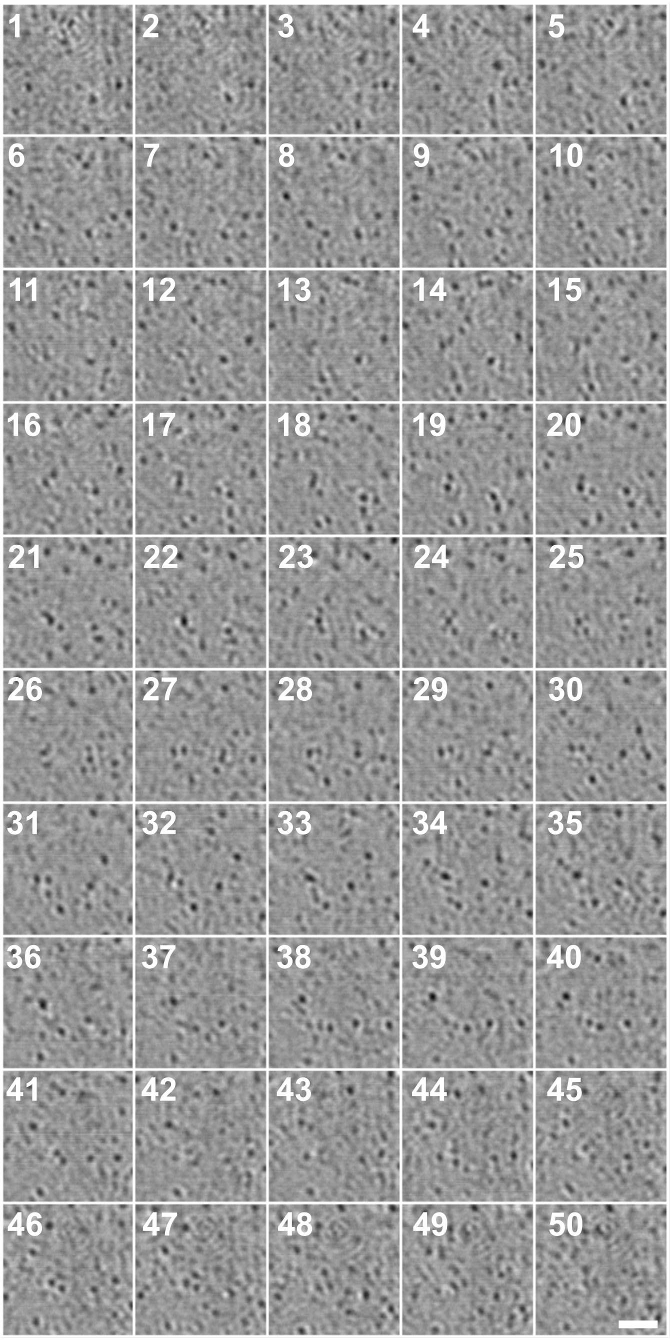

Figure 4.10: Extended image sequence of nanodomains in dynamic equilibrium at $\rho = 0.6$. Scale bar 2.5 µm.

4.6 Characterisation of the transient dynamics of L_o nanodomains

To characterise their dynamics, the observed transient L_o nanodomains were tracked as described in subsection 2.6.1 and analyzed using a home written MATLAB script (Appendix B.2). The HWHM of the Gaussian-fitted transient nanodomains did not vary with their peak contrast, consistent with diffraction limited nanodomains.

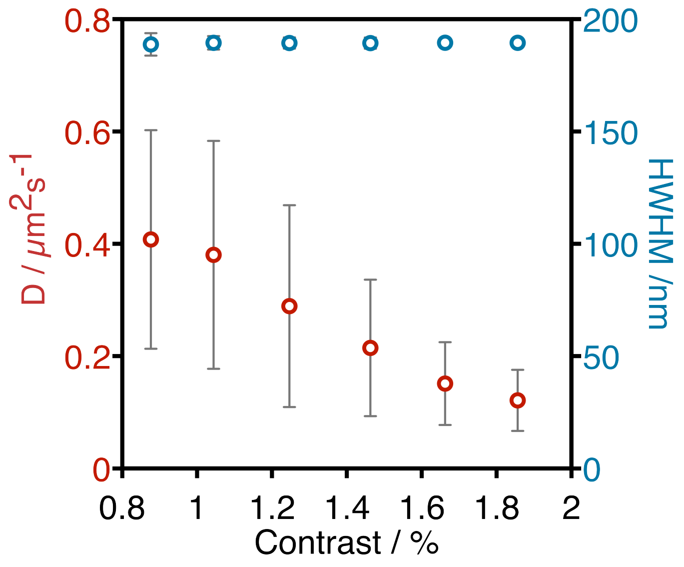

Figure 4.11: Measured diffusion versus contrast and HWHM for $\rho = 0.6$ (749 domains).

Nanodomains were transient with a mean lifetime of 220 ms and a standard deviation of 60 ms. The upper limit for the lifetime of those transient nanodomains did not exceed 350 ms, however, the lower limit was governed by the detection limit of the imaging setup. The dependance of the contrast on the radius of S_0 nanodomains, represented by the sigmoid form, can be applied to infer the radii of the transient nanoscopic L_o domains. The sigmoid function in figure 4.7 is multiplied by the ratio of the maximum detected contrast for L_o to S_o microdomains (2.2% to 4%) to estimate average size of the imaged transient nanoscopic L_o domains. The range of radii of the observed nanodomains is broad, consistent with their dynamic nature, and has a mean of 130 nm. In addition, all radii values are below the reported HWHM ($\approx$ 190 nm) in agreement with previous conclusion that they are diffraction-limited in size.

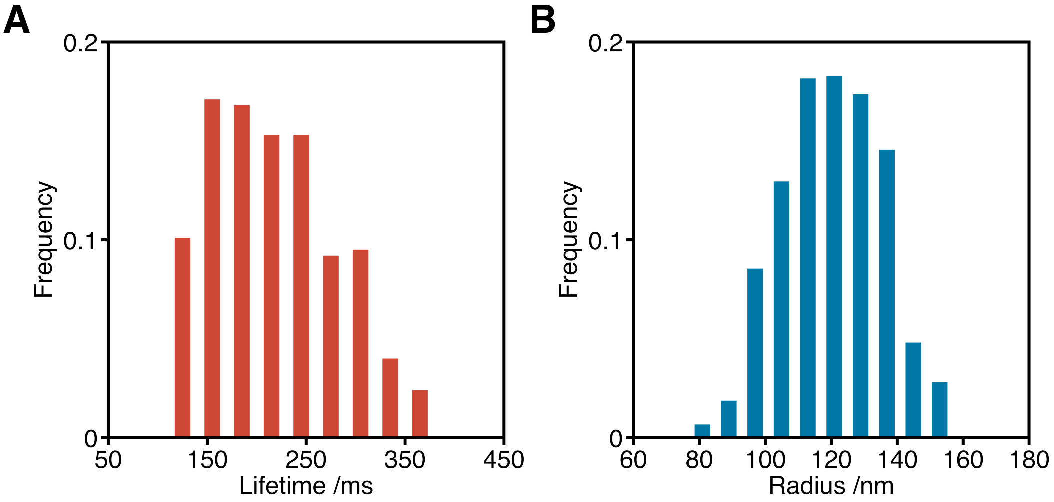

Figure 4.12: Distribution of lifetimes (A) and calculated radii (B) transient of nanodomains for $\rho = 0.6$ (749 domains).

4.7 Discussion

The precise mechanistic role of lipid rafts remains elusive. In some scenarios, membrane proteins are expected to contribute to the coalescence of transient nanoscopic lipid domains to form discernable micron-sized domains which are sufficiently stable over long periods of time to control downstream protein functions. The precise manner in which cellular membranes modulate the size, and consequently the lifetime, of its rafts, if they exist, is yet unexplored. But, the nanodomain lifetimes measured, and detailed herein, are on a similar order to the kinetics reported for many membrane-signaling processes [30, 113, 187]. This suggests that the dynamic creation and destruction of lipid nanodomains might indeed be a key modulator of protein signaling. One example is the dimerization of GPI-anchored receptors taking place on the timescale of a several hundred ms, where dimerization might be altered by raft-lipid interactions

[177]. These results represent the first step in exploiting iSCAT to provide a quantitative understanding of the potential role of nanoscopic lipid phase separation in membrane signaling.

4.8 Summary

This chapter details my work in exploiting the differences in light scattering from lipid bilayer phases to achieve dynamic imaging of nanoscopic lipid domains without any fluorescent labels. We resolve the diffusion of domains larger than 50 nm in radius and observe nanodomain formation, destruction and dynamic coalescence with a domain lifetime of 220 +/- 60 ms. Domain dynamics on this timescale suggests an important role in modulating membrane protein function.

5

Conclusion and outlook

In this dissertation, I have described work towards imaging and characterizing lipid phase separation in DIBs. The accessibility of DIBs to optical microscopy, has helped providing novel insights on the functional architecture of heterogenous lipid membranes. Specifically, the introduction of iSCAT as a label-free, all-optical, tool for probing DIBs has confirmed the existence of transient nanoscopic domains in heterogenous lipid membranes. The detection of functional, transient and nanoscopic lipid rafts in the plasma membrane of living cells remains a holy grail in molecular biology research. The challenges posed by the mentioned goal are both numerous and varied [136]. The development of lipid probes which can faithfully partition into the L_o phase and the use of STED-FCS has rendered fluorescence microscopy capable of detecting domains as small as 60 nm; yet it fails to detect such transient nanoscopic lipid rafts in biological membranes. Here, iSCAT was used to resolve transient lipid nanodomains *in vitro*, the question remains if this method could be applied to living cells. iSCAT lacks the molecular specificity to differentiate between different biological entities in a crowded environment. Preliminary experiments performed on surface adhered HeLa and ptk2 cells were inconclusive (figure 5.1). At some instances, static[1], nanoscopic, membrane-localized objects were seen, and at others, the scattering signal from the plasma membrane was dis-

---

[1] The membrane-localized static objects could be lipid Caveolae; nanoscopic membrane undulations which are implicated in numerous membrane signalling and trafficking processes [30, 78, 171].

torted by the interference of inter-cellular scattering signals.

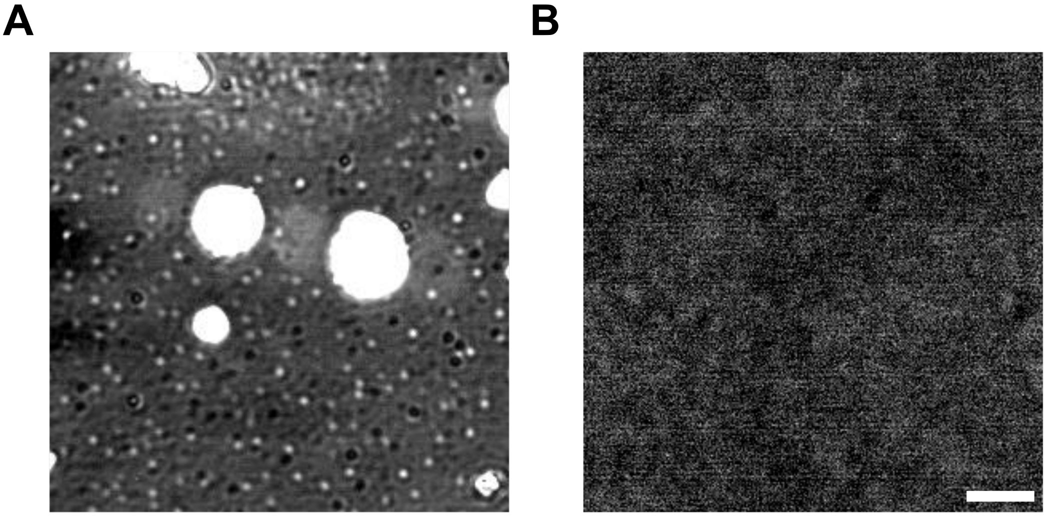

Figure 5.1: Label-free imaging of surface adhered (A) HeLa and (B) ptk2 cells using iSCAT.

The aim is to combine the sensitivity of iSCAT with the specificity of single molecule fluorescence and try to detect the transient enhancement of raft-implicated proteins in transient nanoscopic lipid domains *in vitro* first, then *in vivo*. This goal is inevitably challenging and should span a long term, meanwhile, the dynamics of the observed transient lipid nanodomains should be better characterized. Control over the size of L_o nanodomains was demonstrated by modulating the ratio of lipids in quaternary mixtures. To permit mathematical modelling of this behaviour, the mean radii and lifetimes for transient nanodomains should be precisely quantified for a large range of lipid molar ratios. This can be achieved by sampling of specific quaternary lipid mixtures with different mixing ratios or using the titration method described in chapter 3. The titration method will not only permit control over the composition of the individual bilayers, but will offer the possibility of mimicking cellular lipid recycling *in vitro* and examining its effect on lipid phase separation and protein organization.

With respect to protein dynamics, here, it was shown that the insertion and pore formation of EqII are strongly correlated with the presence of tensed phase boundaries. If lipids rafts could exist in living cells they would posses low line tensions similar to those mimicked *in vitro* using quaternary lipid mixtures. Combining the techniques used to examine the phase-dependant pore formation of EqII with the dynamic, label-free, imaging of transient nanodomains should permit an examination of the different models of how peripheral proteins interact with transient nanoscopic lipid rafts.

Finally, iSCAT is not limited in its application to single, fast-diffusing, biological molecules, but can indeed, be used to study a large number of other systems whose dimensions are between 100 nm and 1 µm. For these applications, powerful lasers and fast cameras are not required. In fact, incoherent light sources, as opposed to coherent laser sources (e.g. Light Emitting Diodes (LEDs)), were found to be capable of producing a detectable contrast from 40 nm gold nanoparticles. This finding needs to be better formalized to open up new opportunities for the development of low-cost iSCAT microscopy.

Bibliography

[1] D Ackerman and G Feigenson. Multiscale Modeling of Four-Component Lipid Mixtures: Domain Composition, Size, Alignment, and Properties of the Phase Interface. *J. Phys. Chem.*, 2015.

[2] B Al-Sakere, F André, C Bernat, E Connault, P Opolon, R Davalos, B Rubinsky, and L Mir. Tumor Ablation with Irreversible Electroporation. *PLoS One*, 2(11):e1135, 2007.

[3] P Almeida. Thermodynamics of lipid interactions in complex bilayers. *Biochim. Biophys. Acta*, 1788(1):72–85, 2009.

[4] M Alonso and J Millán. The role of lipid rafts in signalling and membrane trafficking in T lymphocytes. *J. Cell Sci.*, 114(22):3957–3965, 2001.

[5] G Anderluh and P Macek. Cytolytic peptide and protein toxins from sea anemones (Anthozoa: Actiniaria). *Toxicon*, 40(2):111–124, 2002.

[6] J Ando, M Kinoshita, J Cui, H Yamakoshi, K Dodo, K Fujita, M Murata, and M Sodeoka. Sphingomyelin distribution in lipid rafts of artificial monolayer membranes visualized by Raman microscopy. *Proc. Natl. Acad. Sci.*, 112(15):4558–4563, 2015.

[7] J Andrecka, J Ortega Arroyo, Y Takagi, G de Wit, A Fineberg, L MacKinnon, G Young, J Sellers, and P Kukura. Structural dynamics of myosin 5 during processive motion revealed by interferometric scattering microscopy. *Elife*, 4, 2015.

[8] J Andrecka, K Spillane, J Ortega-Arroyo, and P Kukura. Direct Observation and Control of Supported Lipid Bilayer Formation with Interferometric Scattering Microscopy. *ACS Nano*, 7(12):10662–10670, 2013.

[9] M Angelova and D Dimitrov. Liposome electroformation. *Faraday Discuss.*, 81(0):303–311, 1986.

[10] L Arriaga, S Datta, S Kim, E Amstad, T Kodger, F Monroy, and D Weitz. Ultrathin Shell Double Emulsion Templated Giant Unilamellar Lipid Vesicles with Controlled Microdomain Formation. *Small*, 10(5):950–956, 2014.

[11] S Arumugam, E Petrov, and P Schwille. Cytoskeletal Pinning Controls Phase Separation in Multicomponent Lipid Membranes. *Biophys. J.*, 108(5):1104–1113, 2015.

[12] P Atkins and D Paula. *Physical Chemistry.* Oxford University Press, Oxford, 8th edition, 2006.

[13] D Axelrod. Cell-substrate contacts illuminated by total internal reflection fluorescence. *J. Cell Biol.*, 89(1):141–5, 1981.

[14] B Bakrač, I Gutiérrez-Aguirre, Z Podlesek, A Sonnen, R Gilbert, P Maček, J Lakey, and G Anderluh. Molecular Determinants of Sphingomyelin Specificity of a Eukaryotic Pore-forming Toxin. *J. Biol. Chem.*, 283(27):18665–18677, 2008.

[15] K Balasubramanian and A Schroit. Aminophospholipid Asymmetry: A Matter of Life and Death. *Annu. Rev. Physiol.*, 65(1):701–734, 2003.

[16] T Baumgart, A Hammond, P Sengupta, S Hess, D Holowka, B Baird, and W Webb. Large-scale fluid/fluid phase separation of proteins and lipids in giant plasma membrane vesicles. *Proc. Natl. Acad. Sci.*, 104(9):3165–3170, 2007.

[17] T Baumgart, S Hess, and W Webb. Imaging coexisting fluid domains in biomembrane models coupling curvature and line tension. *Nature*, 425(6960):821–824, 2003.

[18] T Baumgart, G Hunt, E Farkas, W Webb, and G Feigenson. Fluorescence probe partitioning between L(o)/L(d) phases in lipid membranes. *Biochim. Biophys. Acta*, 1768(9):2182–2194, 2007.

[19] E Baykal-Caglar, E Hassan-Zadeh, B Saremi, and J Huang. Preparation of giant unilamellar vesicles from damp lipid film for better lipid compositional uniformity. *Biochim. Biophys. Acta*, 1818(11):2598–2604, 2012.

[20] H Bayley. Membrane-protein structure: Piercing insights. *Nature*, 459(7247):651–652, 2009.

[21] H Bayley, B Cronin, A Heron, M Holden, W Hwang, R Syeda, J Thompson, and M Wallace. Droplet interface bilayers. *Mol. Biosyst.*, 4(12):1191–1208, 2008.

[22] H Bayley, L Jayasinghe, and M Wallace. Prepore for a breakthrough. *Nat Struct Mol Biol*, 12(5):385–386, 2005.

[23] D Benvegnu and H McConnell. Line tension between liquid domains in lipid monolayers. *J. Phys. Chem.*, 96(16):6820–6824, 1992.

[24] N Bezlyepkina, R Gracià, P Shchelokovskyy, R Lipowsky, and R Dimova. Phase Diagram and Tie-Line Determination for the Ternary Mixture DOPC/eSM/Cholesterol. *Biophys. J.*, 104(7):1456–1464, 2013.

[25] K Blodgett. Films Built by Depositing Successive Monomolecular Layers on a Solid Surface. *J. Am. Chem. Soc.*, 57(6):1007–1022, 1935.

[26] J Boggs. Lipid intermolecular hydrogen bonding: influence on structural organization and membrane function. *Biochim. Biophys. Acta - Rev. Biomembr.*, 906(3):353–404, 1987.

[27] J Boon and B Smith. Chemical control of phospholipid distribution across bilayer membranes. *Med. Res. Rev.*, 22(3):251–281, 2002.

[28] M Bramkamp and D Lopez. Exploring the Existence of Lipid Rafts in Bacteria. *Microbiol. Mol. Biol. Rev.*, 79(1):81–100, 2015.

[29] J Briggs, T Wilk, and S Fuller. Do lipid rafts mediate virus assembly and pseudotyping? *J. Gen. Virol.*, 84(4):757–768, 2003.

[30] D. Brown and E London. Functions of Lipid Rafts in Biological Membranes. *Annu. Rev. Cell Dev. Biol.*, 14(1):111–136, 1998.

[31] S Campbell, S Crowe, and J Mak. Lipid rafts and HIV-1: from viral entry to assembly of progeny virions. *J. Clin. Virol.*, 22(3):217–227, 2001.

[32] D Cerneus, E Ueffing, G Posthuma, G Strous, and A Van der Ende. Detergent insolubility of alkaline phosphatase during biosynthetic transport and endocytosis. Role of cholesterol. *J. Biol. Chem.*, 268(5):3150–3155, 1993.

[33] N Chazal and D Gerlier. Virus Entry, Assembly, Budding, and Membrane Rafts. *Microbiol. Mol. Biol. Rev.*, 67(2):226–237, 2003.

[34] P Cicuta, SL Keller, and S Veatch. Diffusion of Liquid Domains in Lipid Bilayer Membranes. *J. Phys. Chem.*, 111(13):3328–3331, 2007.

[35] M Collins and S Keller. Tuning lipid mixtures to induce or suppress domain formation across leaflets of unsupported asymmetric bilayers. *Proc. Natl. Acad. Sci.*, 105(1):124–128, 2008.

[36] S Connell, G Heath, P Olmsted, and A Kisil. Critical point fluctuations in supported lipid membranes. *Faraday Discuss.*, 161(0):91–111, 2013.

[37] K Crnigoj Kristan, G Viero, M Dalla Serra, P Macek, and G Anderluh. Molecular mechanism of pore formation by actinoporins. *Toxicon*, 54(8):1125–1134, 2009.

[38] W Curatolo. The physical properties of glycolipids. *Biochim. Biophys. Acta - Rev. Biomembr.*, 906(2):111–136, 1987.

[39] A Curtis. The Mechanism of Adhesion of Cells to Glass: A Study by Interference Reflection Microscopy. *J. Cell Biol.*, 20(2):199–215, 1964.

[40] J Danielli and H Davson. A contribution to the theory of permeability of thin films. *J. Cell. Comp. Physiol.*, 5(4):495–508, 1935.

[41] E Danielsen. Involvement of Detergent-Insoluble Complexes in the Intracellular Transport of Intestinal Brush Border Enzymes. *Biochemistry*, 34(5):1596–1605, 1995.

[42] C Dietrich, L Bagatolli, Z Volovyk, N Thompson, M Levi, K Jacobson, and E Gratton. Lipid Rafts Reconstituted in Model Membranes. *Biophys. J.*, 80(3):1417–1428, March 2001.

[43] Y Domanov, S Aimon, G Toombes, M Renner, F Quemeneur, A Triller, M Turner, and P Bassereau. Mobility in geometrically confined membranes. *Proc. Natl. Acad. Sci.*, 108(31):12605–12610, 2011.

[44] K Dressler, S Mathias, and R Kolesnick. Tumor necrosis factor-alpha activates the sphingomyelin signal transduction pathway in a cell-free system. *Science (80-.).*, 255(5052):1715–1718, 1992.

[45] Y Dufrêne and G Lee. Advances in the characterization of supported lipid films with the atomic force microscope. *Biochim. Biophys. Acta - Biomembr.*, 1509(1):14–41, 2000.

[46] M Edidin. The State of Lipid Rafts: From Model Membranes to Cells. *Annu. Rev. Biophys. Biomol. Struct.*, 32(1):257–283, 2003.

[47] M Edidin, S Kuo, and M Sheetz. Lateral movements of membrane glycoproteins restricted by dynamic cytoplasmic barriers. *Science (80-.).*, 254(5036):1379–1382, 1991.

[48] C Eggeling, C Ringemann, R Medda, G Schwarzmann, K Sandhoff, S Polyakova, V Belov, B Hein, C Middendorff, A Schönle, and S Hell. Direct observation of the nanoscale dynamics of membrane lipids in a living cell. *Nature*, 457(7233):1159–1162, 2009.

[49] S El-Andaloussi, Y Lee, S Lakhal-Littleton, J Li, Y Seow, C Gardiner, L Alvarez-Erviti, I Sargent, and M Wood. Exosome-mediated delivery of siRNA in vitro and in vivo. *Nat. Protoc.*, 7(12):2112–2126, 2012.

[50] D Engelman. X-ray diffraction studies of phase transitions in the membrane of Mycoplasma laidlawii. *J. Mol. Biol.*, 47(1):115–117, 1970.

[51] T Estep, D Mountcastle, Y Barenholz, R Biltonen, and T Thompson. Thermal behavior of synthetic sphingomyelin-cholesterol dispersions. *Biochemistry*, 18(10):2112–2117, 1979.

[52] M Ethier, D Wolf, and D Melchior. Calorimetric investigation of the phase partitioning of the fluorescent carbocyanine probes in phosphatidylcholine bilayers. *Biochemistry*, 22(5):1178–1182, 1983.

[53] E Evans and E Sackmann. Translational and rotational drag coefficients for a disk moving in a liquid membrane associated with a rigid substrate. *J. Fluid Mech.*, 194:553–561, 1988.

[54] J Feder. Spreading of giant vesicles on moderately adhesive substrates by fingering: a reflection interference contrast microscopy study. *Phys. Rev. E*, 51(4), 1995.

[55] G Feigenson. Phase behavior of lipid mixtures. *Nat. Chem. Biol.*, 2(11):560–563, 2006.

[56] A Fra, E Williamson, K Simons, and R Parton. Detergent-insoluble glycolipid microdomains in lymphocytes in the absence of caveolae. *J. Biol. Chem.*, 269(49):30745–30748, 1994.

[57] L Frye and M Edidin. The Rapid Intermixing of Cell Surface Antigens After Formation of Mouse-Human Heterokaryons. *J. Cell Sci.*, 7(2):319–335, 1970.

[58] T Fujiwara, K Ritchie, H Murakoshi, K Jacobson, and A Kusumi. Phospholipids undergo hop diffusion in compartmentalized cell membrane. *J. Cell Biol.*, 157(6):1071–1082, 2002.

[59] L Garcia-Ortega, J Alegre-Cebollada, S Garcia-Linares, M Bruix, A Martinez-del Pozo, and J Gavilanes. The behavior of sea anemone actinoporins at the waterâĂŞmembrane interface. *Biochim. Biophys. Acta - Biomembr.*, 1808(9):2275–2288, 2011.

[60] M Garcia-Parajo, A Cambi, J Torreno-Pina, N Thompson, and K Jacobson. Nanoclustering as a dominant feature of plasma membrane organization. *J. Cell Sci.*, 127(23):4995–5005, 2014.

[61] A García-Sáez, S Buschhorn, H Keller, G Anderluh, K Simons, and P Schwille. Oligomerization and Pore Formation by Equinatoxin II Inhibit Endocytosis and Lead to Plasma Membrane Reorganization. *J. Biol. Chem.*, 286(43):37768–37777, 2011.

[62] A García-Sáez, S Chiantia, and P Schwille. Effect of Line Tension on the Lateral Organization of Lipid Membranes. *J. Biol. Chem.*, 282(46):33537–33544, 2007.

[63] A García-Sáez and P Schwille. Stability of lipid domains. *FEBS Lett.*, 584(9):1653–1658, 2010.

[64] S Garg, J Rühe, K Lüdtke, R Jordan, and C Naumann. Domain Registration in Raft-Mimicking Lipid Mixtures Studied Using Polymer-Tethered Lipid Bilayers. *Biophys. J.*, 92(4):1263–1270, 2007.

[65] S Goh, J Amazon, and G Feigenson. Toward a Better Raft Model: Modulated Phases in the Four-Component Bilayer, DSPC/DOPC/POPC/-CHOL. *Biophys. J.*, 104(4):853–862, 2013.

[66] D Goswami, K Gowrishankar, S Bilgrami, S Ghosh, R Raghupathy, R Chadda, R Vishwakarma, M Rao, and S Mayor. Nanoclusters of GPI-Anchored Proteins Are Formed by Cortical Actin-Driven Activity. *Cell*, 135(6):1085–1097, 2008.

[67] L Gross, O Castell, and M Wallace. Dynamic and Reversible Control of 2D Membrane Protein Concentration in a Droplet Interface Bilayer. *Nano Lett.*, 11(8):3324–3328, 2011.

[68] L Gross, A Heron, S Baca, and M Wallace. Determining Membrane Capacitance by Dynamic Control of Droplet Interface Bilayer Area. *Langmuir*, 27(23):14335–14342, 2011.

[69] G Guigas and M Weiss. Size-dependent diffusion of membrane inclusions. *Biophys. J.*, 91(7):2393–8, 2006.

[70] A Hammond, F Heberle, T Baumgart, D Holowka, B Baird, and G Feigenson. Crosslinking a lipid raft component triggers liquid ordered-liquid disordered phase separation in model plasma membranes. *Proc. Natl. Acad. Sci. U. S. A.*, 102(18):6320–6325, 2005.

[71] G Hammond, S Dove, A Nicol, J Pinxteren, D Zicha, and G Schiavo. Elimination of plasma membrane phosphatidylinositol (4,5)-bisphosphate is required for exocytosis from mast cells. *J. Cell Sci.*, 119(10):2084–2094, 2006.

[72] K Hanada, M Nishijima, Y Akamatsu, and R Pagano. Both Sphingolipids and Cholesterol Participate in the Detergent Insolubility of Alkaline Phosphatase, a Glycosylphosphatidylinositol-anchored Protein, in Mammalian Membranes. *J. Biol. Chem.*, 270(11):6254–6260, 1995.

[73] J Hancock. Lipid rafts: contentious only from simplistic standpoints. *Nat Rev Mol Cell Biol*, 7(6):456–462, 2006.

[74] M Hanzal-Bayer and J Hancock. Lipid rafts and membrane traffic. *FEBS Lett.*, 581(11):2098–2104, 2007.

[75] L Harriss, B Cronin, J Thompson, and M Wallace. Imaging Multiple Conductance States in an Alamethicin Pore. *J. Am. Chem. Soc.*, 133(37):14507–14509, 2011.

[76] F Heberle, R Petruzielo, J Pan, P Drazba, N Kučerka, R Standaert, G Feigenson, and J Katsaras. Bilayer Thickness Mismatch Controls Domain Size in Model Membranes. *J. Am. Chem. Soc.*, 135(18):6853–6859, 2013.

[77] H Heerklotz. Triton promotes domain formation in lipid raft mixtures. *Biophys. J.*, 83(5):2693–2701, 2002.

[78] J Helms and C Zurzolo. Lipids as Targeting Signals: Lipid Rafts and Intracellular Trafficking. *Traffic*, 5(4):247–254, 2004.

[79] A Heron, J Thompson, B Cronin, H Bayley, and M Wallace. Simultaneous Measurement of Ionic Current and Fluorescence from Single Protein Pores. *J. Am. Chem. Soc.*, 131(5):1652–1653, 2009.

[80] AJ Heron, J Thompson, A Mason, and M Wallace. Direct Detection of Membrane Channels from Gels Using Water-in-Oil Droplet Bilayers. *J. Am. Chem. Soc.*, 129(51):16042–16047, 2007.

[81] A Heuck, R Tweten, and A Johnson. β-Barrel Pore-Forming Toxins: Intriguing Dimorphic Proteins. *Biochemistry*, 40(31):9065–9073, 2001.

[82] A Honigmann, V Mueller, S Hell, and C Eggeling. STED microscopy detects and quantifies liquid phase separation in lipid membranes using a new far-red emitting fluorescent phosphoglycerolipid analogue. *Faraday Discuss.*, 161(0):77–89, 2013.

[83] A Honigmann, V Mueller, H Ta, A Schoenle, E Sezgin, S Hell, and C Eggeling. Scanning STED-FCS reveals spatiotemporal heterogeneity of lipid interaction in the plasma membrane of living cells. *Nat Commun*, 5, 2014.

[84] A Honigmann, S Sadeghi, J Keller, S Hell, C Eggeling, and R Vink. A lipid bound actin meshwork organizes liquid phase separation in model membranes. *Elife*, 3:e01671, 2014.

[85] K Horger, D Estes, R Capone, and M Mayer. Films of Agarose Enable Rapid Formation of Giant Liposomes in Solutions of Physiologic Ionic Strength. *J. Am. Chem. Soc.*, 131(5):1810–1819, 2009.

[86] J Huang and G Feigenson. A microscopic interaction model of maximum solubility of cholesterol in lipid bilayers. *Biophys. J.*, 76(4):2142–2157, 1999.

[87] B Hughes, B Pailthorpe, and L White. The translational and rotational drag on a cylinder moving in a membrane. *J. Fluid Mech.*, 110:349–372, 1981.

[88] I Iacovache, F van der Goot, and L Pernot. Pore formation: An ancient yet complex form of attack. *Biochim. Biophys. Acta - Biomembr.*, 1778(7âĂŞ8):1611–1623, 2008.

[89] K Jacobson, O Mouritsen, and R Anderson. Lipid rafts: at a crossroad between cell biology and physics. *Nat Cell Biol*, 9(1):7–14, 2007.

[90] L Janosi, Z Li, J Hancock, and A Gorfe. Organization, dynamics, and segregation of Ras nanoclusters in membrane domains. *Proc. Natl. Acad. Sci. U. S. A.*, 109(21):8097–8102, 2012.

[91] K Jaqaman, D Loerke, M Mettlen, H Kuwata, S Grinstein, S Schmid, and G Danuser. Robust single-particle tracking in live-cell time-lapse sequences. *Nat Meth*, 5(8):695–702, 2008.

[92] R Joachim and S Erich. Imaging optical thicknesses and separation distances of phospholipid vesicles at solid surfaces. *J. Phys. II Fr.*, 3(5):727–748, 1993.

[93] P Kabouridis, J Janzen, A Magee, and S Ley. Cholesterol depletion disrupts lipid rafts and modulates the activity of multiple signaling pathways in T lymphocytes. *Eur. J. Immunol.*, 30(3):954–963, 2000.

[94] Y Kaizuka and J Groves. Structure and Dynamics of Supported Intermembrane Junctions. *Biophys. J.*, 86(2):905–912, 2004.

[95] K Karamdad, R Law, J Seddon, N Brooks, and O Ces. Preparation and mechanical characterisation of giant unilamellar vesicles by a microfluidic method. *Lab Chip*, 15(2):557–562, 2015.

[96] M Karnvosky, A Kleinfeld, R Hoover, and R Klausner. The concept of lipid domains in membranes. *J. Cell Biol.*, 94(1):1–6, 1982.

[97] J Klingler and H McConnell. Brownian motion and fluid mechanics of lipid monolayer domains. *J. Phys. Chem.*, 97(22):6096–6100, 1993.

[98] R Kolesnick, A Haimovitz-Friedman, and Z Fuks. The sphingomyelin signal transduction pathway mediates apoptosis for tumor necrosis factor, Fas, and ionizing radiation. *Biochem. Cell Biol.*, 72(11-12):471–474, 1994.

[99] T Konyakhina, J Wu, J Mastroianni, F Heberle, and G Feigenson. Phase diagram of a 4-component lipid mixture: DSPC/DOPC/POPC/chol. *Biochim. Biophys. Acta*, 1828(9):2204–2214, 2013.

[100] J Korlach, P Schwille, W Webb, and G Feigenson. Characterization of lipid bilayer phases by confocal microscopy and fluorescence correlation spectroscopy. *Proc. Natl. Acad. Sci.*, 96(15):8461–8466, 1999.

[101] D Kucik, S Kuo, E Elson, and M Sheetz. Preferential attachment of membrane glycoproteins to the cytoskeleton at the leading edge of lamella. *J. Cell Biol.*, 114(5):1029–1036, 1991.

[102] P Kukura, H Ewers, C Müller, A Renn, A Helenius, and V Sandoghdar. High-speed nanoscopic tracking of the position and orientation of a single virus. *Nat. Methods*, 6(12):923–927, 2009.

[103] A Kusumi, C Nakada, K Ritchie, K Murase, K Suzuki, H Murakoshi, R Kasai, J Kondo, and T Fujiwara. Paradigm Shift of the Plasma Membrane Concept from the Two-Dimensional Continuum Fluid to the Partitioned Fluid: High-Speed Single-Molecule Tracking of Membrane Molecules. *Annu. Rev. Biophys. Biomol. Struct.*, 34(1):351–378, 2005.

[104] A Kusumi and Y Sako. Cell surface organization by the membrane skeleton. *Curr. Opin. Cell Biol.*, 8(4):566–574, 1996.

[105] B Lagerholm, G Weinreb, K Jacobson, and N Thompson. Detecting microdomains in intract cell membranes. *Annu. Rev. Phys. Chem.*, 56(1):309–336, 2004.

[106] I Langmuir. The Constitution and fundamental properties of Solids and Liquids. *J. Am. Chem. Soc.*, 38(11):2221–2295, 1916.

[107] A Larbi, N Douziech, A Khalil, Gi Dupuis, S Gherairi, K Guérard, and T Fülöp. Effects of methyl-β-cyclodextrin on T lymphocytes lipid rafts with aging. *Exp. Gerontol.*, 39(4):551–558, 2004.

[108] M Ledesma, K Simons, and C Dotti. Neuronal polarity: essential role of protein lipid complexes in axonal sorting. *Proc. Natl. Acad. Sci. U. S. A.*, 95(7):3966–3971, 1998.

[109] S Leptihn, O Castell, B Cronin, E Lee, L Gross, D Marshall, J Thompson, M Holden, and M Wallace. Constructing droplet interface bilayers from the contact of aqueous droplets in oil. *Nat. Protoc.*, 8(6):1048–1057, 2013.

[110] I Levental, F Byfield, P Chowdhury, F Gai, T Baumgart, and P Janmey. Cholesterol-dependent phase separation in cell-derived giant plasma-membrane vesicles. *Biochem. J.*, 424(2):163–167, 2009.

[111] K Lindfors, T Kalkbrenner, P Stoller, and V Sandoghdar. Detection and Spectroscopy of Gold Nanoparticles Using Supercontinuum White Light Confocal Microscopy. *Phys. Rev. Lett.*, 93(3):37401, 2004.

[112] D Lingwood, J Ries, P Schwille, and K Simons. Plasma membranes are poised for activation of raft phase coalescence at physiological temperature. *Proc. Natl. Acad. Sci.*, 105(29):10005–10010, 2008.

[113] D Lingwood and K Simons. Lipid Rafts As a Membrane-Organizing Principle. *Science (80-.).*, 327(5961):46–50, 2010.

[114] A Liu and D Fletcher. Actin Polymerization Serves as a Membrane Domain Switch in Model Lipid Bilayers. *Biophys. J.*, 91(11):4064–4070, 2006.

[115] B Machta, S Papanikolaou, J Sethna, and S Veatch. Minimal Model of Plasma Membrane Heterogeneity Requires Coupling Cortical Actin to Criticality. *Biophys. J.*, 100(7):1668–1677, 2011.

[116] S Matosevic and B Paegel. Stepwise Synthesis of Giant Unilamellar Vesicles on a Microfluidic Assembly Line. *J. Am. Chem. Soc.*, 133(9):2798–2800, 2011.

[117] H McConnell and A Radhakrishnan. Condensed complexes of cholesterol and phospholipids. *Biochim. Biophys. Acta*, 1610(2):159–173, 2003.

[118] D Melchior, H Morowitz, J Sturtevant, and T Tsong. Characterization of the plasma membrane of Mycoplasma laidlawii. VII. Phase transitions of membrane lipids. *Biochim. Biophys. Acta - Biomembr.*, 219(1):114–122, 1970.

[119] A Merrill, M Sullards, E Wang, K Voss, and R Riley. Sphingolipid metabolism: roles in signal transduction and disruption by fumonisins. *Environ. Health Perspect.*, 109(Suppl 2):283–289, 2001.

[120] D Milovanovic, A Honigmann, S Koike, F Göttfert, G Pähler, M Junius, S Müllar, U Diederichsen, A Janshoff, H Grubmüller, H Risselada, C Eggeling, S Hell, G van den Bogaart, and R Jahn. Hydrophobic mismatch sorts SNARE proteins into distinct membrane domains. *Nat Commun*, 6, 2015.

[121] M Mingeot-Leclercq, M Deleu, R Brasseur, and Y Dufrene. Atomic force microscopy of supported lipid bilayers. *Nat. Protoc.*, 3(10):1654–1659, 2008.

[122] K Moissoglu, V Kiessling, C Wan, B Hoffman, A Norambuena, L Tamm, and M Schwartz. Regulation of Rac1 translocation and activation by membrane domains and their boundaries. *J. Cell Sci.*, 127(11):2565–2576, 2014.

[123] N Momin, S Lee, A Gadok, D Busch, G Bachand, C Hayden, J Stachowiak, and D Sasaki. Designing lipids for selective partitioning into liquid ordered membrane domains. *Soft Matter*, 11(16):3241–3250, 2015.

[124] M Montal and P Mueller. Formation of bimolecular membranes from lipid monolayers and a study of their electrical properties. *Proc. Natl. Acad. Sci.*, 69(12):3561–6, 1972.

[125] P Mueller, D Rudin, and W Wescott. Reconstitution of Cell Membrane Structure in vitro and its Transformation into an Excitable System. *Nature*, 194(4832):979–980, 1962.

[126] S Mukherjee and F Maxfield. Role of Membrane Organization and Membrane Domains in Endocytic Lipid Trafficking. *Traffic*, 1(3):203–211, 2000.

[127] S Munro. Lipid Rafts: Elusive or Illusive? *Cell*, 115(4):377–388, 2003.

[128] A Ono and E Freed. Plasma membrane rafts play a critical role in HIV-1 assembly and release. *Proc. Natl. Acad. Sci. U. S. A.*, 98(24):13925–13930, 2001.

[129] J op den Kamp. Lipid Asymmetry in Membranes. *Annu. Rev. Biochem.*, 48(1):47–71, 1979.

[130] J Ortega Arroyo, J Andrecka, K Spillane, N Billington, Y Takagi, J Sellers, and P Kukura. Label-free, all-optical detection, imaging, and tracking of a single protein. *Nano Lett.*, 14(4):2065–2070, 2014.

[131] J Ortega-Arroyo and P Kukura. Interferometric scattering microscopy (iSCAT): new frontiers in ultrafast and ultrasensitive optical microscopy. *Phys. Chem. Chem. Phys.*, 14(45):15625–15636, 2012.

[132] M Parker and S Feil. Pore-forming protein toxins: from structure to function. *Prog. Biophys. Mol. Biol.*, 88(1):91–142, 2005.

[133] E Petrov, R Petrosyan, and P Schwille. Translational and rotational diffusion of micrometer-sized solid domains in lipid membranes. *Soft Matter*, 8(29):7552–7555, 2012.

[134] E Petrov and P Schwille. Translational Diffusion in Lipid Membranes beyond the Saffman-Delbrück Approximation. *Biophys. J.*, 94(5):L41–L43, 2008.

[135] L Pike. Rafts defined: a report on the Keystone symposium on lipid rafts and cell function. *J. Lipid Res.*, 47(7):1597–1598, 2006.

[136] L Pike. The challenge of lipid rafts. *J. Lipid Res.*, 50(Suppl):S323–S328, 2009.

[137] M Piliarik and V Sandoghdar. Direct optical sensing of single unlabelled proteins and super-resolution imaging of their binding sites. *Nat. Commun.*, 5, 2014.

[138] N Povey and N Parker. Temperature dependence of bulk viscosity in water using acoustic spectroscopy. *J. Phys. Conf. Ser.*, 269(1):12011, 2011.

[139] V Puri, R Watanabe, M Dominguez, X Sun, C Wheatley, D Marks, and R Pagano. Cholesterol modulates membrane traffic along the endocytic pathway in sphingolipid-storage diseases. *Nat Cell Biol*, 1(6):386–388, 1999.

[140] G Putzel, M Uline, I Szleifer, and M Schick. Interleaflet Coupling and Domain Registry in Phase-Separated Lipid Bilayers. *Biophys. J.*, 100(4):996–1004, 2011.

[141] J Raedler, H Strey, and E Sackmann. Phenomenology and Kinetics of Lipid Bilayer Spreading on Hydrophilic Surfaces. *Langmuir*, 11(11):4539–4548, 1995.

[142] R Raghupathy, A Anilkumar, A Polley, P Singh, M Yadav, C Johnson, S Suryawanshi, V Saikam, S Sawant, A Panda, Z Guo, R Vishwakarma, M Rao, and S Mayor. Transbilayer Lipid Interactions Mediate Nanoclustering of Lipid-Anchored Proteins. *Cell*, 161(3):581–594, 2015.

[143] S Rawat, M Viard, S Gallo, A Rein, R Blumenthal, and A Puri. Modulation of entry of enveloped viruses by cholesterol and sphingolipids. *Mol. Membr. Biol.*, 20(3):243–254, 2003.

[144] J Reeves and R Dowben. Formation and properties of thin-walled phospholipid vesicles. *J. Cell. Physiol.*, 73(1):49–60, 1969.

[145] R Reigada. Electroporation of heterogeneous lipid membranes. *Biochim. Biophys. Acta - Biomembr.*, 1838(3):814–821, 2014.

[146] J Richens, J Lane, M Mather, and P OShea. The interactions of squalene, alkanes and other mineral oils with model membranes; effects on membrane heterogeneity and function. *J. Colloid Interface Sci.*, 457:225–231, 2015.

[147] D Richmond, E Schmid, S Martens, J Stachowiak, N Liska, and D Fletcher. Forming giant vesicles with controlled membrane composition, asymmetry, and contents. *Proc. Natl. Acad. Sci.*, 108(23):9431–9436, 2011.

[148] N Rojko, B Cronin, J Danial, M Baker, G Anderluh, and M Wallace. Imaging the Lipid-Phase-Dependent Pore Formation of Equinatoxin II in Droplet Interface Bilayers. *Biophys. J.*, 106(8):1630–1637, 2015.

[149] U Ros and A García-Sáez. More Than a Pore: The Interplay of Pore-Forming Proteins and Lipid Membranes. *J. Membr. Biol.*, 248(3):545–561, 2015.

[150] P Saffman and M Delbruck. Brownian motion in biological membranes. *Proc. Natl. Acad. Sci.*, 72(8):3111–3113, 1975.

[151] S Saka, A Honigmann, C Eggeling, S Hell, T Lang, and S Rizzoli. Multi-protein assemblies underlie the mesoscale organization of the plasma membrane. *Nat Commun*, 5:4509–4522, 2014.

[152] Y Sako and A Kusumi. Compartmentalized structure of the plasma membrane for receptor movements as revealed by a nanometer-level motion analysis. *J. Cell Biol.*, 125(6):1251–1264, 1994.

[153] Y Sako and A Kusumi. Barriers for lateral diffusion of transferrin receptor in the plasma membrane as characterized by receptor dragging by laser tweezers: fence versus tether. *J. Cell Biol.*, 129(6):1559–1574, 1995.

[154] Z Salamon, H Macleod, and G Tollin. Surface plasmon resonance spectroscopy as a tool for investigating the biochemical and biophysical properties of membrane protein systems. I: Theoretical principles. *Biochim. Biophys. Acta - Rev. Biomembr.*, 1331(2):117–129, 1997.

[155] A Samsonov, I Mihalyov, and F Cohen. Characterization of cholesterol-sphingomyelin domains and their dynamics in bilayer membranes. *Biophys. J.*, 81(3):1486–1500, 2001.

[156] M Sargiacomo, M Sudol, Z Tang, and M Lisanti. Signal transducing molecules and glycosyl-phosphatidylinositol-linked proteins form a caveolin-rich insoluble complex in MDCK cells. *J. Cell Biol.*, 122(4):789–807, 1993.

[157] P Scheiffele, A Rietveld, T Wilk, and K Simons. Influenza Viruses Select Ordered Lipid Domains during Budding from the Plasma Membrane. *J. Biol. Chem.*, 274(4):2038–2044, 1999.

[158] C Scheve, P Gonzales, N Momin, and J Stachowiak. Steric Pressure between Membrane-Bound Proteins Opposes Lipid Phase Separation. *J. Am. Chem. Soc.*, 135(4):1185–1188, 2013.

[159] C Schmidt, A Horwitz, D Lauffenburger, and M Sheetz. Integrin-cytoskeletal interactions in migrating fibroblasts are dynamic, asymmetric, and regulated. *J. Cell Biol.*, 123(4):977–991, 1993.

[160] P Schön, A García-Sáez, P Malovrh, K Bacia, G Anderluh, and P Schwille. Equinatoxin II Permeabilizing Activity Depends on the Presence of Sphingomyelin and Lipid Phase Coexistence. *Biophys. J.*, 95(2):691–698, 2008.

[161] Y Shai. Mechanism of the binding, insertion and destabilization of phospholipid bilayer membranes by α-helical antimicrobial and cell non-selective membrane-lytic peptides. *Biochim. Biophys. Acta - Biomembr.*, 1462(1):55–70, 1999.

[162] C Shao, E Kendall, and D DeVoe. Electro-optical BLM chips enabling dynamic imaging of ordered lipid domains. *Lab Chip*, 12(17):3142–3149, 2012.

[163] K Simons and E Ikonen. Functional rafts in cell membranes. *Nature*, 387(6633):569–572, 1997.

[164] K Simons and J Sampaio. Membrane Organization and Lipid Rafts. *Cold Spring Harb. Perspect. Biol.*, 3(10), 2011.

[165] K Simons and D Toomre. Lipid rafts and signal transduction. *Nat Rev Mol Cell Biol*, 1(1):31–39, 2000.

[166] K Simons and W Vaz. Model Systems, Lipid Rafts, and Cell Membranes. *Annu. Rev. Biophys. Biomol. Struct.*, 33(1):269–295, 2004.

[167] S Singer and G Nicolson. The Fluid Mosaic Model of the Structure of Cell Membranes. *Science (80-.).*, 175(4023):720–731, 1972.

[168] J Skibbens, M Roth, and K Matlin. Differential extractability of influenza virus hemagglutinin during intracellular transport in polarized epithelial cells and nonpolar fibroblasts. *J. Cell Biol.*, 108(3):821–832, 1989.

[169] L Solanko, A Honigmann, H Midtiby, F Lund, J Brewer, V Dekaris, R Bittman, C Eggeling, and D Wüstner. Membrane Orientation and Lateral Diffusion of BODIPY-Cholesterol as a Function of Probe Structure. *Biophys. J.*, 105(9):2082–2092, 2015.

[170] J Stachowiak, D Richmond, T Li, A Liu, S Parekh, and D Fletcher. Unilamellar vesicle formation and encapsulation by microfluidic jetting. *Proc. Natl. Acad. Sci.*, 105(12):4697–4702, 2008.

[171] T Stauffer and T Meyer. Compartmentalized IgE ReceptorâĂŞmediated Signal Transduction in Living Cells. *J. Cell Biol.*, 139(6):1447–1454, 1997.

[172] J Steim, M Tourtellotte, J Reinert, R McElhaney, and R Rader. Calorimetric Evidence for the Liquid-Crystalline State of Lipids in a Biomembrane. *Proc. Natl. Acad. Sci.*, 63(1):104–109, 1969.

[173] A Stier and E Sackmann. Spin labels as enzyme substrates Heterogeneous lipid distribution in liver microsomal membranes. *Biochim. Biophys. Acta*, 311(3):400–408, 1973.

[174] Y Subburaj, U Ros, E Hermann, R Tong, and A García-Sáez. Toxicity of an α-Pore-forming Toxin Depends on the Assembly Mechanism on the Target Membrane as Revealed by Single Molecule Imaging. *J. Biol. Chem.*, 290(8):4856–4865, 2015.

[175] I Sugar and E Neumann. Stochastic model for electric field-induced membrane pores electroporation. *Biophys. Chem.*, 19(3):211–225, 1984.

[176] K Suzuki. Lipid rafts generate digital-like signal transduction in cell plasma membranes. *Biotechnol. J.*, 7(6):753–761, 2012.

[177] K Suzuki, R Kasai, K Hirosawa, Y Nemoto, M Ishibashi, Y Miwa, T Fujiwara, and A Kusumi. Transient GPI-anchored protein homodimers are units for raft organization and function. *Nat Chem Biol*, 8(9):774–783, 2012.

[178] M Takeda, G Leser, C Russell, and R Lamb. Influenza virus hemagglutinin concentrates in lipid raft microdomains for efficient viral fusion. *Proc. Natl. Acad. Sci.*, 100(25):14610–14617, 2003.

[179] L Tamm and H McConnell. Supported phospholipid bilayers. *Biophys. J.*, 47(1):105–113, 1985.

[180] M Tanaka, J Hermann, I Haase, M Fischer, and S Boxer. Frictional Drag and Electrical Manipulation of Recombinant Proteins in Polymer-Supported Membranes. *Langmuir*, 23(10):5638–5644, 2007.

[181] M Tarek. Membrane Electroporation: A Molecular Dynamics Simulation. *Biophys. J.*, 88(6):4045–4053, 2005.

[182] J Thompson, B Cronin, H Bayley, and M Wallace. Rapid Assembly of a Multimeric Membrane Protein Pore. *Biophys. J.*, 101(11):2679–2683, 2011.

[183] J Thompson, A Heron, Y Santoso, and M Wallace. Enhanced Stability and Fluidity in Droplet on Hydrogel Bilayers for Measuring Membrane Protein Diffusion. *Nano Lett.*, 7(12):3875–3878, 2007.

[184] T Thompson and T Tillack. Organization of Glycosphingolipids in Bilayers and Plasma Membranes of Mammalian Cells. *Annu. Rev. Biophys. Biophys. Chem.*, 14(1):361–386, 1985.

[185] D Tieleman. The molecular basis of electroporation. *BMC Biochem.*, 5:10, 2004.

[186] M Tourtellotte, D Branton, and A Keith. Membrane Structure: Spin Labeling and Freeze Etching of Mycoplasma laidlawii. *Proc. Natl. Acad. Sci. U. S. A.*, 66(3):909–916, 1970.

[187] B Truong-Quang and P Lenne. Membrane microdomains: from seeing to understanding. *Front. Plant Sci.*, 5, 2014.

[188] M Turner, P Sens, and N Socci. Nonequilibrium Raftlike Membrane Domains under Continuous Recycling. *Phys. Rev. Lett.*, 95(16):168301, 2005.

[189] M Valapala and J Vishwanatha. Lipid Raft Endocytosis and Exosomal Transport Facilitate Extracellular Trafficking of Annexin A2. *J. Biol. Chem.*, 286(35):30911–30925, 2011.

[190] G van Meer and A de Kroon. Lipid map of the mammalian cell. *J. Cell Sci.*, 124(1):5–8, 2011.

[191] G van Meer and Q Lisman. Sphingolipid Transport: Rafts and Translocators. *J. Biol. Chem.*, 277(29):25855–25858, 2002.

[192] G van Meer, D Voelker, and G Feigenson. Membrane lipids: where they are and how they behave. *Nat. Rev. Mol. Cell Biol.*, 9(2):112–124, 2008.

[193] R Varma and S Mayor. GPI-anchored proteins are organized in submicron domains at the cell surface. *Nature*, 394(6695):798–801, 1998.

[194] S Veatch, P Cicuta, P Sengupta, A Honerkamp-Smith, D Holowka, and B Baird. Critical Fluctuations in Plasma Membrane Vesicles. *ACS Chem. Biol.*, 3(5):287–293, 2008.

[195] S Veatch, K Gawrisch, and S Keller. Closed-Loop Miscibility Gap and Quantitative Tie-Lines in Ternary Membranes Containing Diphytanoyl PC. *Biophys. J.*, 90(12):4428–4436, 2006.

[196] S Veatch and S Keller. Separation of Liquid Phases in Giant Vesicles of Ternary Mixtures of Phospholipids and Cholesterol. *Biophys. J.*, 85(5):3074–3083, 2003.

[197] S Veatch and S Keller. Seeing spots: Complex phase behavior in simple membranes. *Biochim. Biophys. Acta*, 1746(3):172–185, 2005.

[198] S Veatch, O Soubias, S Keller, and K Gawrisch. Critical fluctuations in domain-forming lipid mixtures. *Proc. Natl. Acad. Sci.*, 104(45):17650–17655, 2007.

[199] O Wesolowska, K Michalak, J Maniewska, and A Hendrich. Giant unilamellar vesicles - a perfect tool to visualize phase separation and lipid rafts in model systems. *Acta Biochim. Pol.*, 56(1):33–39, 2009.

[200] A Wiese and U Seydel. Interaction of peptides and proteins with bacterial surface glycolipids: a comparison of glycosphingolipids and lipopolysaccharides. *J. Ind. Microbiol. Biotechnol.*, 23(4):414–424, 1999.

[201] F Wunderlich, A Ronai, V Speth, J Seelig, and A Blume. Thermotropic lipid clustering in tetrahymena membranes. *Biochemistry*, 14(17):3730–3735, 1975.

[202] S Yang, V Kiessling, J Simmons, J White, and L Tamm. HIV gp41-mediated membrane fusion occurs at edges of cholesterol-rich lipid domains. *Nat Chem Biol*, 11(6):424–431, 2015.

[203] J Zhang, A Pekosz, and R Lamb. Influenza Virus Assembly and Lipid Raft Microdomains: a Role for the Cytoplasmic Tails of the Spike Glycoproteins. *J. Virol.*, 74(10):4634–4644, 2000.

[204] Y Zhu and S Granick. Limits of the Hydrodynamic No-Slip Boundary Condition. *Phys. Rev. Lett.*, 88(10):106102, 2002.

[205] R Zidovetzki and I Levitan. Use of cyclodextrins to manipulate plasma membrane cholesterol content: evidence, misconceptions and control strategies. *Biochim. Biophys. Acta*, 1768(6):1311–1324, 2007.

Appendix A

Publications

A.1 Journal Articles

* equal contribution

A. **J. S. H. Danial**, C. Mallick, B. Cronin and M. I. Wallace. On demand modulation of lipid composition in an individual bilayer. Under preparation.

B. G. de Wit*, **J. S. H. Danial***, P. Kukura and M. I. Wallace. Dynamic label-free imaging of lipid nanodomains. PNAS. Under review.

C. N. Rojko, B. Cronin, **J. S. H. Danial**, M. A. Baker, G. Anderluh, M. I. Wallace. Imaging the lipid-phase-dependent pore formation of equinatoxin II in droplet interface bilayers. Biophys J. 2014, 106(8):1630-7

A.2 Book Chapters

A. E. Weatherill, **J. S. H. Danial** and M. I. Wallace. Channels, Pumps and Transporters. Wiley. In press.

Appendix B

Codes

B.1 Stack Reduction Code

```
Average=300
SourceDir = getDirectory("Choose a Directory");
FolderList = getFileList(SourceDir);
length=FolderList.length
for (i=1; i<=length; i+=Average)
{
run("Image Sequence...", "open=[SourceDir] number=Average ...
    starting=i increment=1 scale=100 file=tif");
run("Grouped Z Project...","Group=Average");
selectWindow(File.getName(SourceDir) );
close();
}
run("Concatenate...", "all_open title=[Concatenated Stacks]");
run("Z Project...","start=1 stop=i")
imageCalculator("Divide create 32-bit stack", "Concatenated ...
    Stacks","MED_Concatenated Stacks");
```

B.2 Tracks Processing Code

```
clear all;
close all;
FILE_NAME = uigetfile('*.csv','Please choose your video ...
    files','MultiSelect','on');
FILES_COUNT = numel(cellstr(FILE_NAME));
PIXEL_SIZE = 0.0424;
FRAME_TIME = 0.01;
SCALING_FACTOR = 10;
SLICE_WIDTH = 10;
TRACK_ID = [];
MAX_TRACK_ID = 0;
POSITION_X = [];
```

```
POSITION_Y = [];
MSD_T_PARTICLE_NUMBER = 97;
INTENSITY_T_PARTICLE_NUMBER = 15;
MEAN_INTENSITY = [];
FRAME_NUMBER = [];
ESTIMATED_DIAMETER = [];
DATA = [];
DIFFUSION_C = [];
VECTOR_MSD_FINAL = [];
MSD_T_VECTOR_MSD = [];
TRACK_COUNTER = 1;
FULL_TRACK_COUNTER = 1;
for FILE_NUMBER = 1 : FILES_COUNT
    DATA = [];
    INDIVIDUAL_TRACK = [];
    TRACK_ID = [];
    POSITION_X = [];
    POSITION_Y = [];
    MEAN_INTENSITY = [];
    FRAME_NUMBER = [];
    ESTIMATED_DIAMETER = [];
    FOUND_TRACK_FLAG = 0;
    DATA = csvread(strcat(FILE_NAME{FILE_NUMBER}));
    TRACK_ID = DATA(:,4);
    MAX_TRACK_ID = max(TRACK_ID);
    POSITION_X = DATA(:,6);
    POSITION_Y = DATA(:,7);
    FRAME_NUMBER = DATA(:,10)+1;
    MEAN_INTENSITY = DATA(:,15);
    ESTIMATED_DIAMETER = DATA(:,20);
    for TRACK_NUMBER = 0 : MAX_TRACK_ID
        INDIVIDUAL_TRACK = [];
        COPY_INDIVIDUAL_TRACK = [];
        for SPOT_NUMBER = 1 : length(TRACK_ID)
            if TRACK_NUMBER == TRACK_ID(SPOT_NUMBER)
                INDIVIDUAL_TRACK(FRAME_NUMBER(SPOT_NUMBER),1) ...
                   = FRAME_NUMBER(SPOT_NUMBER);
                INDIVIDUAL_TRACK(FRAME_NUMBER(SPOT_NUMBER),2) ...
                   = POSITION_X(SPOT_NUMBER);
                INDIVIDUAL_TRACK(FRAME_NUMBER(SPOT_NUMBER),3) ...
                   = POSITION_Y(SPOT_NUMBER);
                INDIVIDUAL_TRACK(FRAME_NUMBER(SPOT_NUMBER),4) ...
                   = MEAN_INTENSITY(SPOT_NUMBER);
                INDIVIDUAL_TRACK(FRAME_NUMBER(SPOT_NUMBER),5) ...
                   = ESTIMATED_DIAMETER(SPOT_NUMBER);
            end
        end
        if isempty(INDIVIDUAL_TRACK) == 0
            if size(INDIVIDUAL_TRACK,1) < 40
                VECTOR_TAU(FULL_TRACK_COUNTER) = ...
                   nnz(INDIVIDUAL_TRACK)/5;
            end
            FULL_TRACK_COUNTER = FULL_TRACK_COUNTER + 1;
            COPY_INDIVIDUAL_TRACK = INDIVIDUAL_TRACK;
```

```
            for SLICE_INDEX = 1 : SLICE_WIDTH : ...
               size(INDIVIDUAL_TRACK,1) - SLICE_WIDTH
                INDIVIDUAL_TRACK = [];
                if FULL_TRACK_COUNTER == MSD_T_PARTICLE_NUMBER
                    INDIVIDUAL_TRACK = COPY_INDIVIDUAL_TRACK;
                else
                    INDIVIDUAL_TRACK(1 : SLICE_WIDTH , : ) = ...
                       COPY_INDIVIDUAL_TRACK(SLICE_INDEX : ...
                       SLICE_INDEX + SLICE_WIDTH - 1 , :);
                end
                for i = 1 : size(INDIVIDUAL_TRACK,1)
                    if FULL_TRACK_COUNTER ~= MSD_T_PARTICLE_NUMBER
                        VECTOR_FRAME(i,TRACK_COUNTER) = ...
                           INDIVIDUAL_TRACK(i,1);
                        VECTOR_X_POS(i,TRACK_COUNTER) = ...
                           INDIVIDUAL_TRACK(i,2);
                        VECTOR_Y_POS(i,TRACK_COUNTER) = ...
                           INDIVIDUAL_TRACK(i,3);
                        VECTOR_INTENSITY(i,TRACK_COUNTER) = ...
                           INDIVIDUAL_TRACK(i,4);
                        VECTOR_DIAMETER(i,TRACK_COUNTER) = ...
                           INDIVIDUAL_TRACK(i,5);
                    end
                end
                FULL_FLAG = 0;
                for GAP = 1 : ...
                   INDIVIDUAL_TRACK(size(INDIVIDUAL_TRACK(:,1),1),1) ...
                   - INDIVIDUAL_TRACK(1,1)
                    N = 0;
                    MSD = 0;
                    for INDEX_1 = 1 : ...
                       size(INDIVIDUAL_TRACK(:,1),1) - 1
                        for INDEX_2 = INDEX_1 + 1 : ...
                           size(INDIVIDUAL_TRACK(:,1),1)
                            if INDIVIDUAL_TRACK(INDEX_2,1) - ...
                               INDIVIDUAL_TRACK(INDEX_1,1) == ...
                               GAP & ...
                               INDIVIDUAL_TRACK(INDEX_2,2) > ...
                               0.5 & ...
                               INDIVIDUAL_TRACK(INDEX_1,2) > ...
                               0.5 & ...
                               INDIVIDUAL_TRACK(INDEX_2,3) > ...
                               0.5 & ...
                               INDIVIDUAL_TRACK(INDEX_1,3) > 0.5
                                MSD = MSD + ...
                                   (INDIVIDUAL_TRACK(INDEX_2,2) ...
                                   - ...
                                   INDIVIDUAL_TRACK(INDEX_1,2)).^2 ...
                                   + ...
                                   (INDIVIDUAL_TRACK(INDEX_2,3) ...
                                   - ...
                                   INDIVIDUAL_TRACK(INDEX_1,3)).^2;
                                N = N + 1;
                                break;
```

```
                            end
                        end
                    end
                    if N > 0 & INDIVIDUAL_TRACK(:,2) > 0 & ...
                       FULL_TRACK_COUNTER ~= MSD_T_PARTICLE_NUMBER
                        VECTOR_MSD(GAP,TRACK_COUNTER) = MSD / N;
                        VECTOR_N(GAP,TRACK_COUNTER) = N;
                        FULL_FLAG = 1;
                    elseif N == 0 & INDIVIDUAL_TRACK(:,2) > 0 ...
                       & FULL_TRACK_COUNTER ~= ...
                       MSD_T_PARTICLE_NUMBER
                        VECTOR_MSD(GAP,TRACK_COUNTER) = 0;
                        VECTOR_N(GAP,TRACK_COUNTER) = N;
                        FULL_FLAG = 1;
                    elseif N > 0 & FULL_TRACK_COUNTER == ...
                       MSD_T_PARTICLE_NUMBER
                        MSD_T_VECTOR_MSD(GAP) = MSD / N;
                    elseif N == 0 & FULL_TRACK_COUNTER == ...
                       MSD_T_PARTICLE_NUMBER
                        MSD_T_VECTOR_MSD(GAP) = 0;
                    end
                end
                if FULL_TRACK_COUNTER ~= MSD_T_PARTICLE_NUMBER ...
                   & FULL_FLAG == 1;
                    TRACK_COUNTER = TRACK_COUNTER + 1;
                end
            end
        end
    end
end
%% Calculation of MSDs
MSD_LENGTH = 2;
RED_TRACK_NUMBER = 1;
COUNT = 1;
I_C_T_VECTOR_MSD = [];
MSD_C_T_VECTOR_MSD = [];
for TRACK_NUMBER = 1 : size(VECTOR_MSD,2)
    VECTOR_N_INT = 0;
    for INT = 1 : MSD_LENGTH
        if INT == 1
            VECTOR_MSD_INT(INT) = ...
               (VECTOR_MSD(INT,TRACK_NUMBER) - 0) * ...
               (VECTOR_N(INT,TRACK_NUMBER));
        else
            VECTOR_MSD_INT(INT) = ...
               (VECTOR_MSD(INT,TRACK_NUMBER) - VECTOR_MSD(INT ...
               - 1,TRACK_NUMBER)) * (VECTOR_N(INT,TRACK_NUMBER));
        end
        VECTOR_N_INT = VECTOR_N_INT + VECTOR_N(INT,TRACK_NUMBER);
    end
    if abs(VECTOR_MSD_INT(1) - VECTOR_MSD_INT(2)) < 30
        VECTOR_MSD_FINAL(RED_TRACK_NUMBER) = ...
           sum(VECTOR_MSD_INT) .* ((PIXEL_SIZE ^ 2) / ...
           (VECTOR_N_INT));
```

```
        VECTOR_INTENSITY_COPY(:,RED_TRACK_NUMBER) = ...
           VECTOR_INTENSITY(:,TRACK_NUMBER);
        VECTOR_DIAMETER_COPY(:,RED_TRACK_NUMBER) = ...
           VECTOR_DIAMETER(:,TRACK_NUMBER);
        RED_TRACK_NUMBER = RED_TRACK_NUMBER + 1;
    end
end
VECTOR_INTENSITY = [];
VECTOR_INTENSITY = VECTOR_INTENSITY_COPY;
VECTOR_DIAMETER = [];
VECTOR_DIAMETER = VECTOR_DIAMETER_COPY;
%% calculation of diffusion co-efficients
VECTOR_DIFFUSION_FINAL = VECTOR_MSD_FINAL ./ (4 * FRAME_TIME);
%% calculation of Intensity values
for TRACK_NUMBER = 1  : size(VECTOR_INTENSITY,2)
    INT_PRE_SUM = 0;
    COUNT = 0;
    for INDEX_R = 1 : size(VECTOR_INTENSITY,1)
        if VECTOR_INTENSITY(INDEX_R,TRACK_NUMBER) ~= 0
            INT_PRE_SUM = INT_PRE_SUM + ...
               VECTOR_INTENSITY(INDEX_R,TRACK_NUMBER);
            COUNT = COUNT + 1;
        end
    end
    VECTOR_INTENSITY_FINAL(TRACK_NUMBER) = INT_PRE_SUM / ...
       (SCALING_FACTOR * COUNT);
end
%% calculation of Measured Diameter
for TRACK_NUMBER = 1  : size(VECTOR_DIAMETER,2)
    DIAM_PRE_SUM = 0;
    COUNT = 0;
    for INDEX_R = 1 : size(VECTOR_DIAMETER,1)
        if VECTOR_DIAMETER(INDEX_R,TRACK_NUMBER) > 8 && ...
           VECTOR_DIAMETER(INDEX_R,TRACK_NUMBER) < 10
            DIAM_PRE_SUM = DIAM_PRE_SUM + ...
               VECTOR_DIAMETER(INDEX_R,TRACK_NUMBER);
            COUNT = COUNT + 1;
        end
    end
    VECTOR_DIAMETER_FINAL(TRACK_NUMBER) = (DIAM_PRE_SUM * ...
       PIXEL_SIZE) / COUNT;
end
%% Ranging
RANGE = find(VECTOR_INTENSITY_FINAL > 0 & ...
   VECTOR_INTENSITY_FINAL < 2 & VECTOR_DIFFUSION_FINAL < 1 & ...
   VECTOR_DIFFUSION_FINAL > 0 & VECTOR_DIAMETER_FINAL > 0);
VECTOR_INTENSITY_FINAL = VECTOR_INTENSITY_FINAL(RANGE);
VECTOR_DIFFUSION_FINAL = VECTOR_DIFFUSION_FINAL(RANGE);
VECTOR_DIAMETER_FINAL = VECTOR_DIAMETER_FINAL(RANGE) .* 1000;
VECTOR_TAU_FINAL = VECTOR_TAU(find(VECTOR_TAU > 0)) .* FRAME_TIME;
%% Grouping
GROUP_RANGE_OPT(1) = 1;
GROUP_RANGE_OPT(2) = 1;
TEMP_VEC(:,1) = VECTOR_INTENSITY_FINAL;
```

```
if GROUP_RANGE_OPT(1) == 1
    GROUPING_INTERVAL = 5;
    MAX_VALUE = 1.8;
    MIN_VALUE = 0.7;
    TEMP_VEC(:,2) = VECTOR_DIFFUSION_FINAL;
    INDEX = 1;
    MEAN_Y_GROUP_VEC = [];
    MEAN_X_GROUP_VEC = [];
    Y_GROUP_VEC_SUB = [];
    MEAN_ERROR_GROUP_VEC = [];
    DIFFERENCE_INTERVAL = ((MAX_VALUE - MIN_VALUE) / ...
       GROUPING_INTERVAL);
    for RANGE_START = MIN_VALUE : DIFFERENCE_INTERVAL : MAX_VALUE
        X_GROUP_VEC = [];
        Y_GROUP_VEC = [];
        count = 1;
        for i = 1 : length(TEMP_VEC(:,1))
            if TEMP_VEC(i,1) >= RANGE_START && TEMP_VEC(i,1) < ...
               (RANGE_START + DIFFERENCE_INTERVAL)
                X_GROUP_VEC = [X_GROUP_VEC TEMP_VEC(i,1)];
                Y_GROUP_VEC = [Y_GROUP_VEC TEMP_VEC(i,2)];
                Y_GROUP_VEC_SUB(INDEX,count) = TEMP_VEC(i,2);
                count = count + 1;
            end
        end
        if ~isempty(X_GROUP_VEC)
            DIFF_I_MEAN_X_GROUP_VEC(INDEX) = mean(X_GROUP_VEC);
            DIFF_I_MEAN_Y_GROUP_VEC(INDEX) = mean(Y_GROUP_VEC);
            DIFF_I_MEAN_ERROR_GROUP_VEC(INDEX) = ...
               std(Y_GROUP_VEC,1);
            INDEX = INDEX + 1;
        end
    end
end
if GROUP_RANGE_OPT(2) == 1
    GROUPING_INTERVAL = 5;
    MAX_VALUE = 1.8;
    MIN_VALUE = 0.8;
    TEMP_VEC(:,2) = VECTOR_DIAMETER_FINAL;
    INDEX = 1;
    MEAN_Y_GROUP_VEC = [];
    MEAN_X_GROUP_VEC = [];
    MEAN_ERROR_GROUP_VEC = [];
    DIFFERENCE_INTERVAL = ((MAX_VALUE - MIN_VALUE) / ...
       GROUPING_INTERVAL);
    for RANGE_START = MIN_VALUE : DIFFERENCE_INTERVAL : MAX_VALUE
        X_GROUP_VEC = [];
        Y_GROUP_VEC = [];
        count = 1;
        for i = 1 : length(TEMP_VEC(:,1))
            if TEMP_VEC(i,1) >= RANGE_START && TEMP_VEC(i,1) < ...
               (RANGE_START + DIFFERENCE_INTERVAL)
                X_GROUP_VEC = [X_GROUP_VEC TEMP_VEC(i,1)];
                Y_GROUP_VEC = [Y_GROUP_VEC TEMP_VEC(i,2)];
```

```
                count = count + 1;
            end
        end
        if ~isempty(X_GROUP_VEC)
            DIAM_I_MEAN_X_GROUP_VEC(INDEX) = mean(X_GROUP_VEC);
            DIAM_I_MEAN_Y_GROUP_VEC(INDEX) = mean(Y_GROUP_VEC);
            DIAM_I_MEAN_ERROR_GROUP_VEC(INDEX) = ...
               std(Y_GROUP_VEC,1);
            INDEX = INDEX + 1;
        end
    end
end
%% Data exclusion
EXC_RANGE = find(DIFF_I_MEAN_X_GROUP_VEC > 0.7);
DIFF_I_MEAN_X_GROUP_VEC = DIFF_I_MEAN_X_GROUP_VEC(EXC_RANGE);
DIFF_I_MEAN_Y_GROUP_VEC = DIFF_I_MEAN_Y_GROUP_VEC(EXC_RANGE);
DIFF_I_MEAN_ERROR_GROUP_VEC = ...
   DIFF_I_MEAN_ERROR_GROUP_VEC(EXC_RANGE);
%% calculation of Estimated Diameter
FIT_OPTION(1) = 1;
FIT_OPTION(2) = 1;
X_MIN = 0.8;
X_MAX = 2;
STEP = 0.001;
X_RANGE_FINAL = X_MIN : STEP : X_MAX;
X_RANGE_RED = X_RANGE_FINAL ./ 100;
K_B = 1.3806503e-23;
TEMP_K = 25 + 273;
H = 3.3e-9;
if FIT_OPTION(1) == 1
    INITIAL_GUESS = [2e-9,0.001,5e12];
    FIT_PARAMETERS = optimset('Display', 'iter');
    GUIGAS_VAR = lsqnonlin(@(GUIGAS_VAR) ...
       DIFF_I_MEAN_Y_GROUP_VEC - 1e12 .* ...
       GUIGAS_FITTING_FUNCTION(GUIGAS_VAR, ...
       (DIFF_I_MEAN_X_GROUP_VEC ./ 100)), INITIAL_GUESS, [], ...
       [], FIT_PARAMETERS);
    GUIGAS_DIFFUSION_EQUATION_FINAL = ((K_B .* TEMP_K) ./ (8 ...
       .* pi .* GUIGAS_VAR(2))) .* tan(GUIGAS_VAR(1) .* ...
       sqrt(GUIGAS_VAR(3) ./ X_RANGE_RED)) ./ sqrt(X_RANGE_RED ...
       ./ GUIGAS_VAR(3)) .* 1e12;
    ISCAT_DIAMETER_EQUATION_FINAL = sqrt(X_RANGE_RED ./ ...
       GUIGAS_VAR(3)) .* 1e9 .*2;
    ISCAT_DIAMETER_VEC_FINAL = sqrt((VECTOR_INTENSITY_FINAL ./ ...
       100) ./ GUIGAS_VAR(3)) .* 1e9 .*2;
    GUIGAS_VAR(1)
    GUIGAS_VAR(2)
    GUIGAS_VAR(3)
end
if FIT_OPTION(2) == 1
    INITIAL_GUESS = [0.3,0.01,5e12];
    FIT_PARAMETERS = optimset('Display', 'iter');
    SAFFMAN_DELBRUCK_VAR = lsqnonlin(@(SAFFMAN_DELBRUCK_VAR) ...
       DIFF_I_MEAN_Y_GROUP_VEC - 1e12 .* ...
```

```
       SAFFMAN_DELBRUCK_FITTING_FUNCTION(SAFFMAN_DELBRUCK_VAR, ...
       (DIFF_I_MEAN_X_GROUP_VEC ./ 100)), INITIAL_GUESS, [], ...
       [], FIT_PARAMETERS);
    SAFFMAN_DELBRUCK_DIFFUSION_EQUATION_FINAL = ((K_B .* ...
       TEMP_K) ./ (4 .* pi .* H .* SAFFMAN_DELBRUCK_VAR(1))) ...
       .* (log((H .* SAFFMAN_DELBRUCK_VAR(1)) ./ ...
       (sqrt(X_RANGE_RED ./ SAFFMAN_DELBRUCK_VAR(3)) .* ...
       SAFFMAN_DELBRUCK_VAR(2))) - 0.5772 + 0.5) .* 1e12;
    ISCAT_DIAMETER_EQUATION_FINAL = sqrt(X_RANGE_RED ./ ...
       SAFFMAN_DELBRUCK_VAR(3)) .* 1e9 .*2;
    ISCAT_DIAMETER_VEC_FINAL = sqrt((VECTOR_INTENSITY_FINAL ./ ...
       100) ./ SAFFMAN_DELBRUCK_VAR(3)) .* 1e9 .*2;
    SAFFMAN_DELBRUCK_VAR(1)
    SAFFMAN_DELBRUCK_VAR(2)
    SAFFMAN_DELBRUCK_VAR(3)
    CRITICAL_RADIUS = (H .* SAFFMAN_DELBRUCK_VAR(1)) ./ (2 .* ...
       SAFFMAN_DELBRUCK_VAR(2)) * 1e9;
end
ISCAT_RADIUS_VEC_FINAL = ...
    (VECTOR_INTENSITY_FINAL./(50.*0.00002598)).^(1/1.40377);
end
```

Appendix C

Reference material

C.1 Domain radius versus contrast

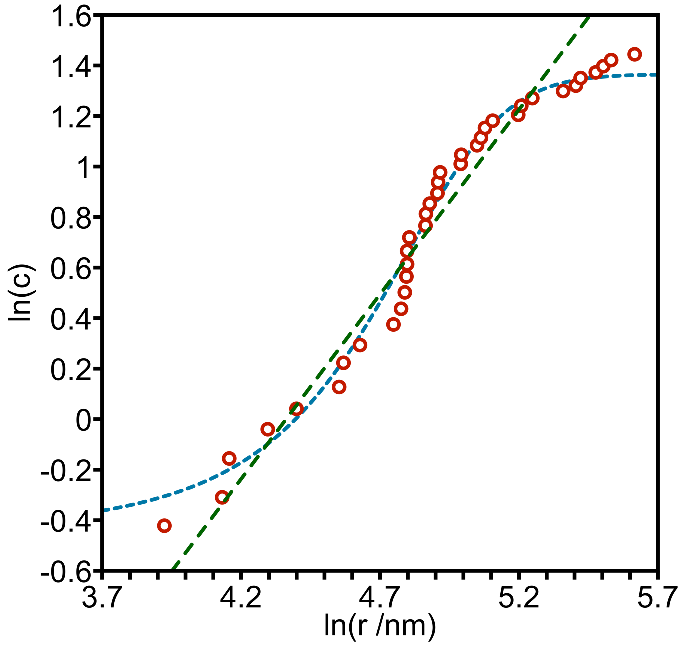

Figure C.1: Logarithmic plot of the variation of the contrast (c) of S_o domains with the radius (r). Dashed lines are power (green, ln(c) = 1.462 ln[r] -6.377), and sigmoid (blue, c = 0.61081 + 3.3037/1+exp[(131.72-r)/25.146]) fits to the data.